Polymer multilayers at liquid interfaces : assembly, interfacial rheology and microfluidic probing.

C. Tregouet

To cite this version:

C. Tregouet. Polymer multilayers at liquid interfaces : assembly, interfacial rheology and microfluidic probing.. Chemical Physics [physics.chem-ph]. Université Pierre et Marie Curie - Paris VI, 2016. English. NNT : 2016PA066299 . tel-01467085

HAL Id: tel-01467085
https://theses.hal.science/tel-01467085

Submitted on 14 Feb 2017

THÈSE DE DOCTORAT
DE L'UNIVERSITÉ PIERRE ET MARIE CURIE

Spécialité

Physico-chimie des matériaux

(ED 397)

Préparée aux LABORATOIRES :
SCIENCES ET INGÉNIERIE DE LA MATIÈRE MOLLE (UMR 7615)
GULLIVER (UMR 7083)

Pour obtenir le grade de

DOCTEUR de l'UNIVERSITÉ PIERRE ET MARIE CURIE

Polymer multilayers at liquid interfaces: assembly, interfacial rheology and microfluidic probing.

Présentée par

Corentin Trégouët

le 14 Octobre 2016

devant le jury composé de :

M.	**BARET**	**Jean-Christophe**	**Rapporteur**
M.	**CLEGG**	**Paul**	**Rapporteur**
M.	**JOANNY**	**Jean-François**	**Examinateur**
M.	**VERMANT**	**Jan**	**Examinateur**
Mme	**MONTEUX**	**Cécile**	**Directrice de thèse**
Mme	**REYSSAT**	**Mathilde**	**Co-directrice de thèse**

Remerciements

Au terme de ces trois années, je voudrais prendre le temps de remercier les personnes qui ont été à mes côtés pendant cette thèse.

Je voudrais tout d'abord remercier Cécile et Mathilde. Votre patience, votre bienveillance et votre confiance ont été plus que précieux durant ces années. Votre patience quand il fallu me former à la microfludique et à la rhéologie, votre bienveillance quand je perdais confiance en moi, votre confiance quand nous nous sommes lancés sur des terrains que nous connaissions moins tels que les éléments finis. Au delà du travail de thèse, vous m'avez guidé vers la suite de ma thèse en m'accompagnant dans mes longues réflexions mais aussi dans mes démarches. Enfin, travailler avec vous a été un plaisir aussi grâce à tous ces moments moins scientifiques partagés autour d'un café, d'un repas au RA, autour d'une partie de Molky aux buttes Chaumonts ou de balançoire à Antony, ou autour de landaus avant les réunions de la team Capsule. Tous ces moments où la science laissait place à la course à pied, aux récits des aventures de vacances, aux échanges de photos de bébés, furent des moments riches que je n'oublierais pas.

Mais ces années n'auraient pas eu le même dénouement ni la même saveur sans la team Capsule. Nadège et Patrick, vous n'aurez pas réussi, malgré tous vos efforts à me faire faire une synthèse, mais malgré tout vous m'avez réconcilié avec la chimie : c'est à vous qu'il faudrait dire "Avec vous la chimie devient simple !". Thomas, merci pour ton aide pour la théorie, mais surtout pour ta simplicité et ton optimisme. Sandrine, ton aide et ta patience lors de mon stage de M2 m'ont mis sur les rails dès le départ, merci pour ton temps et ta gentillesse. Enfin, Julien, merci pour ces années de collaboration et plus particulièrement pour ton soutien (galettes Saint Michel et autres) pendant les moments stressants qu'étaient la rédaction et la préparation de la soutenance.

Plus généralement, je souhaiterais remercier les membres des différents labos au sein desquels j'ai travaillé: le SIMM et Gulliver et plus particulièrement ceux qui font en sorte que les labos et les équipes puissent travailler dans de bonnes conditions, notamment Elie et Christian, Guylaine, et Olivier. Je remercie également toute l'équipe du groupe Soft Materials et notamment Jan Vermant qui m'a chaleureusement accueilli dans ces locaux le temps de quelques séries de manip.

Ces années ont été marquées par les amitiés qui sont nées autour des paillasses, dans les couloirs du labo, aux salles café, aux goûters Kinder, aux réunions ANR de 16h04, aux apéconf' et goûter-conf' et autour des babyfoot du foyer, aux petits déjeuners du mercredi matin, aux bières du lundi, aux concerts de l'amicale, à l'atelier, etc. Merci à vous tous, vous qui avez participé à ces moments là, et notamment mes co-bureaux Marc puis Louis, Ester, Guillaume et Mickaël, et ceux qui sont arrivés et repartis en même temps que moi Marc, Laura, Pascaline, Marine, Louis, Loïc, Paul, Davide, Pierre et Thitima.

J'associe à ces remerciements les 128 et particulièrement ceux que j'avais le plaisir de retrouver pour la traditionnelle Grande Joie : votre accueil m'a beaucoup touché.

J'en profite aussi pour remercier tous mes amis qui se sont déplacés pour venir me soutenir le jour de ma soutenance et fêter mon doctorat. Vos attentions pour me remonter le moral pendant la rédaction et votre présence à ma soutenance m'ont beaucoup touché : les anciens du lycée De Lattre, les grimpeurs, les compamignones, les 2k9, et mes anciens et plus récents colocs.

Je voudrais aussi remercier les enseignants qui ont marqué mon parcours académique, et qui ont contribué à me faire choisir aujourd'hui la recherche et l'enseignement : Stéphane Mary, Jean-Marc Vince, et David Quéré.

Enfin, je remercie mes parents pour leur soutien, mais aussi pour m'avoir transmis cette curiosité scientifique qui m'a guidé tout au long de ces travaux. Bien sur je n'oublie pas les frères et sœurs, beau-frère et neveu, ainsi que toute l'équipe des Montrougiens pour leur soutien sans faille.

Contents of this thesis

Résumé en Français

Le relargage contrôlé est un enjeu industriel qui peut permettre d'augmenter significativement l'efficacité de diverses substances chimiques (parfums, arômes, médicaments, etc). L'encapsulation des substances par une membrane élastique permet de mettre en œuvre ce relargage contrôlé. Diverses méthodes ont été explorées pour obtenir des membranes bien contrôlées. Une méthode prometteuse pour fabriquer des micro-capsules consiste à déposer couche après couche (*Layer-by-Layer*, ou *LbL*) des polymères à la surface de goutte d'huiles ou de bulles d'air, comme illustré sur la Figure 1, en s'assurant que les différentes couches soient liées les unes aux autres par des interactions physiques. Par rapports aux autres méthodes présentes dans la littératures (poly-condensation interfaciale, ou LbL sur colloïdes par exemple), cette méthode est à la fois relativement simple à mettre en œuvre et bien contrôlée. En effet, la membrane est construite directement autour de la substance à protéger, et l'absence de réaction chimique in-situ permet d'éviter la formation de produits indésirables.

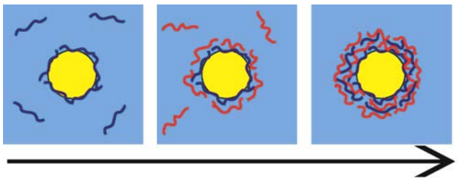

Figure 1: Adsorption de polymères en couche par couche (LbL) sur une interface liquide (surface d'une goutte d'huile dans l'eau) pour fabriquer une microcapsule.

Cette thèse a pour objet ces assemblages en multicouches de polymères aux interfaces liquides. Une analyse de l'état de l'art nous a amené à nous poser les questions suivantes : quels sont les mécanismes dirigeant la dynamique d'adsorption des chaines de polymères à l'interface ? Peut-on dissocier les contributions des différentes interactions mises en jeu dans l'assemblage multicouche sur les propriétés rhéologiques de la membrane ? Dans quelle mesure peut-on étudier ces propriétés de rhéologie interfaciales sur des microcapsules en microfluidique ?

A partir d'expériences menées sur des interfaces modèles entre deux fluides non miscibles et sur des microcapsules et par la modélisation de ces expériences, nous avons étudié l'effet des interactions à l'échelle des chaînes de polymère sur les propriétés rhéologiques de l'interface. Dans un premier temps, je présenterai le système physico-chimique qui constitue nos multicouches. Dans un deuxième temps, j'exposerai les résultats obtenus grâce à des expériences menées sur des interfaces modèles. Ces résultats nous permettront de mieux comprendre l'adsorption des polymères sur l'interface, et le rôle des interactions moléculaires sur les propriétés de rhéologie interaciale de nos multicouches. Enfin, je présenterai comment nous avons utilisé la microfluidique pour fabriquer nos microcapsules et pour mesurer in-situ leurs propriétés mécaniques en mettant à profit les atouts de la microfluidique que sont le bon contrôle des fluides et le grand nombre d'échantillons.

Système étudié

Phases en présence

Les membranes étudiées dans cette thèse sont assemblées sur des interfaces eau/air pour les géométries modèles ou des interfaces eau/huile pour la production microfluidique. Dans le second cas, l'huile utilisée est une huile minérale, vendue par Sigma-Aldrich de viscosité 30 fois supérieur à la viscosité de l'eau, et de densité inférieure à 1.

Polymères

Les polymères utilisés ont été choisis pour être solubles dans l'eau, amphiphiles, et pour établir des interactions attractives entre les différentes couches. Le caractère amphiphiles des polymères permet d'assurer leur adsorption spontanée à une interface. De plus, alors que la plupart des études de la littératures utilisent des polymères chargés interagissant de manière électrostatique, nous avons ici utilisé des polymères neutres interagissant grâce à des liaisons hydrogènes et des interactions hydrophobes. De plus l'ancrage de la première couche avec l'interface peut également être ajusté.

Liaisons hydrogènes : ces liaisons s'établissent entre deux couches successives si l'une présente des atomes d'hydrogène mobiles (tels ceux d'une fonction acide) et l'autre des doublets non liants (tels ceux d'une fonction cétone). Nous avons choisi d'utiliser la polyvinylpyrrolidonne (PVP) comme accepteur de protons, et l'acide polyacrylique (PAA) ainsi que l'acide polymethacrylique (PMAA) comme donneur de protons, comme illustré sur la Figure 2.

Interactions hydrophobes : ces interactions naissent du caractère légèrement hydrophobe des chaînes de polymères. Plus le squelette des chaînes est hydrophobe, plus cette interaction est prononcée. Ainsi, ces interactions ont pu être mesurées entre la PVP et le PMAA, mais pas entre la PVP et le PAA.

Ancrage à l'interface : l'ancrage de la première couche avec l'interface peut être amélioré par l'intermédiaire de greffons hydrophobes (chaînes alkyles) répartis statistiquement le long des chaînes de PAA. Nous notons α le degré de greffage en pourcentage ($\alpha < 5\%$), et n la longueur des greffons ($n = 8$ ou 12), et de tels polymères sont appelé PAA-α-$\mathrm{C_n}$.

Pour garantir la présence du proton de la fonction acide et donc l'établissement des liaisons hydrogènes, toutes les solutions seront utilisées à pH 3.

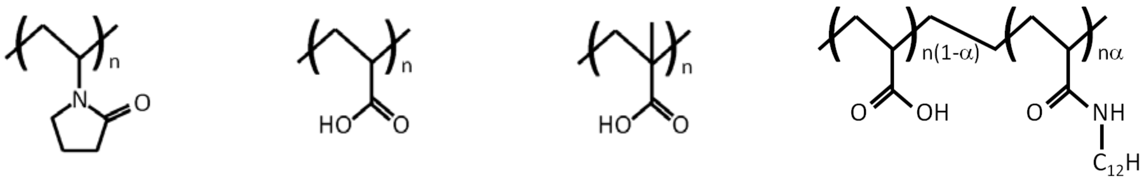

(a) PVP. (b) PAA. (c) PMAA. (d) PAA-α-C_{12}.

Figure 2: Polymères utilisés dans cette thèse: polyvinylpyrrolidonne (PVP), acide polyacrylique (PAA), acide polymethacrylique (PMAA), PAA greffé (PAA-α-C_{12}). Nous avons également utilisé des PAA-α-C_8, non représentés ici.

Monocouches et multicouches en géométries modèles

Dans un premier temps, nous avons utilisé la géométrie modèle qu'est la bulle montante (inverse de la goutte pendante) pour analyser la dynamique d'adsorption des chaînes de polymères constituant la première couche et pour mesurer la réponse de monocouches et multicouches sous compression/dilatation. Enfin, en collaboration avec le groupe de Jan Vermant, nous avons effectué des mesures rhéologiques sur des bicouches dans deux autres géométries (un rhéomètre interfacial de cisaillement et une cuve de compression radiale) pour valider les mesures effectuées en goutte pendante.

Dynamique d'adsorption

Nous avons mesuré la tension interfaciale γ de bulles d'air dans des solutions de polymères au cours du temps. La bulle d'air est fixée à la pointe d'une aiguille reliée à une seringue selon le montage classique de la goutte pendante. Nous nous sommes particulièrement intéressés à l'influence du greffage sur la dynamique d'adsorption. En effet, le tension interfaciale est d'autant plus petite que concentration surfacique Γ est grande. Nous observons sur la Figure 3a qui représente la tension de surface au cours du temps que le greffage mène à des tensions interfaciales plus petites que ce qui est mesuré avec du PAA, et donc que les greffons implique des excès de surface plus grands. Par ailleurs, nous avons observé que la tension interfaciale au temps long décrit une dynamique logarithmique, comme présenté sur la Figure 3b, où l'axe du temps est en échelle logarithmique.

Une cinétique logarithmique est généralement due à une barrière énergétique qui augmente avec le temps. Dans la littérature, des modèles ont été proposés pour d'autres systèmes, proposant deux origines à cette barrière énergétique. Johner et Joanny[1] suggèrent qu'il faut apporter de l'énergie pour déformer la chaîne de polymère, pour lui permettre ainsi d'atteindre l'interface malgré la gène stérique de la brosse formée par les chaînes préalablement adsorbées. Ce mécanisme a été proposé pour des co-polymères diblocs. Par ailleurs, Ward et Tordaï[2] ont proposé un modèle pour des tensioactifs dans lequel l'énergie nécessaire à l'adsorption correspond à l'aire de la portion d'interface à libérer pour ajouter une nouvelle molécule.

---

[1] Johner, A. and Joanny, J. F. Block copolymer adsorption in a selective solvent: a kinetic study. Macromolecules 23, 5299–5311 (1990).

[2] Ward, A. F. H. and Tordai, L. Time-dependence of boundary tensions of solutions: IV. Kinetics of adsorption at liquid-liquid interfaces. Recl. des Trav. Chim. des Pays-Bas 71, 572–584 (1952).

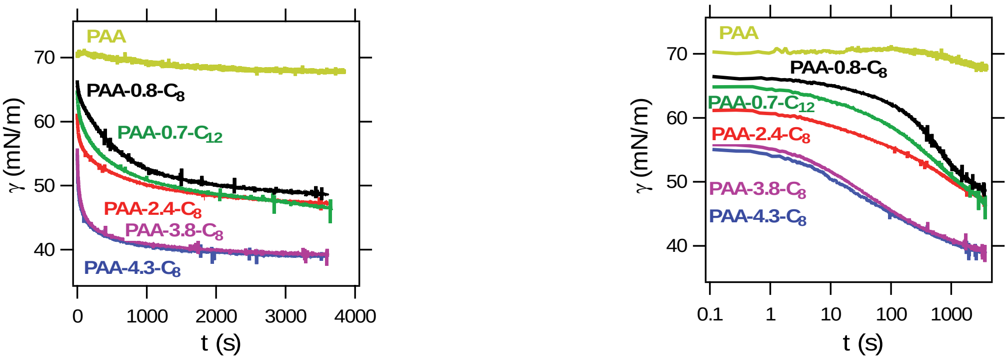

(a) Echelle linéaire.

(b) Echelle logarithmique en abscisse.

Figure 3: Evolution de la tension interfaciale en fonction du temps lors de l'adsorption des chaînes de polymères à l'interface eau/air.

Nous avons montré que ces deux contributions doivent être prises en compte pour décrire la cinétique d'adsorption de nos chaînes de polymère. Nous attribuons cela à la nature des chaînes considérées : la répartition statistique des greffons le long de la chaîne de polymère implique des chaînes plus regroupées (moins étirées) lors leur adsorption que dans le cas de polymère diblocs. Les courbes théoriques dérivées de ce modèle sont ajustées aux courbes expérimentales grâce au paramètre $\mathcal{A}$ qui représente la surface nécessaire à l'adsorption d'une nouvelle chaîne de polymère. Un second paramètre est la taille d'un monomère : b.

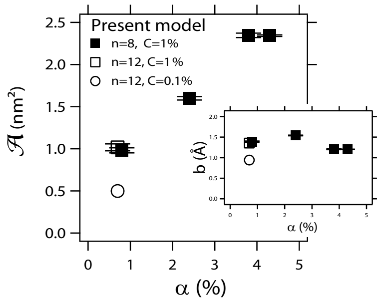

Figure 4: Aire critique $\mathcal{A}$ pour l'adsorption d'une nouvelle chaîne en fonction du taux de greffage α pour différentes longueurs de greffons (n) et différentes concentrations de polymère en solution (C). En encart, valeur du paramètre b représentant la taille du monomère en fonction du taux de greffage α.

Nous observons sur la Figure 4 que l'aire critique $\mathcal{A}$ est de l'ordre de quelques nm^2 et que cette aire augmente avec le taux de greffage α. Par ailleurs nous obervons que la taille du monomère est constante et d'environ 1.5 Å. Nous interprétons la croissance de $\mathcal{A}$ en fonction de α comme la signature d'une adsorption simultanée des greffons : plus il y a de greffons sur la chaîne, plus il faut de place pour adsorber une nouvelle chaîne.

Compression/dilatation de monocouches

La stabilité des capsules dépend fortement de leurs propriétés rhéologiques, et plus particulièrement de leurs réponses en compression/dilatation. En diminuant ou en augmentant le volume des bulles il est possible respectivement de comprimer ou de dilater l'interface. Nous avons mesuré les variations de tension interfaciale induites par les variations de surface, et les avons comparées à ce que l'on mesurerait si la quantité de polymère à l'interface restait constante.

Ainsi, dans le cas des compressions, nous avons pu suivre la désorption des chaînes au cours de la compression. Pour prendre en compte les conditions initiales de l'interface, nous présentons nos données en fonction de la pression de surface théorique s'il n'y avait pas de désorption plutôt qu'en fonction du taux de déformation. Cette pression théorique est une fonction croissante du taux de déformation : elle augmente pendant la compression, et diminue pendant la dilatation. Dans le cas de chaînes de PAA-0.7-C_{12} en compression, comme illustré sur la Figure 5, nous observons qu'à faible déformation la tension interfaciale est identique à la prédiction faite en supposant aucune désorption, mais qu'à grande déformation la tension interfaciale est constante, ce qui s'explique par une désorption rapide. De plus nous observons que la désorption est plus importante lorsque la compression est lente.

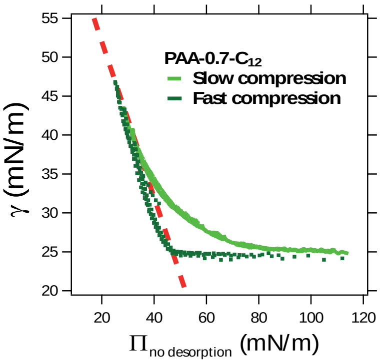

Figure 5: Evolution de la tension de surface en fonction de la pression théorique s'il n'y avait pas de désorption. La ligne rouge pointillée représente le cas théorique sans désorption.

La comparaison entre les différents polymères à notre disposition nous a permis de mettre en évidence deux effets:

- la désorption est plus importante quand les greffons sont plus courts,
- la désorption est plus importante quand la densité de greffage est plus élevée.

Nous interprétons ce deuxième effet comme suit : un taux de greffage plus élevé implique que les longueurs de chaînes sont plus courtes entre les greffons, et donc que la chaîne est contenue dans une épaisseur moindre. Ainsi, les chaînes les plus greffées sont les chaînes les plus contraintes, et correspondent donc à celles qui désorbent plus vite lors de la compression.

Lors de la dilatation des monocouches nous avons mesuré une faible adsorption des chaînes lors de la dilatation dans le cas des chaînes les plus greffées.

Compression de multicouches

L'analyse de la compression des bicouches de PVP avec du PAA, du PMAA ou du PAA-α-C_n sur des interfaces eau/air nous a permis de mettre en avant le rôle des interactions hydrophobes et de l'ancrage à l'interface dans la réponses de ces bicouches à la compression. Nous avons montré que la combinaison de ces deux leviers nous permet de fabriquer des multicouches viscoélastiques, comme illustré sur la Figure 6. L'élasticité de la membrane rend impossible la mesure classique de tension de surface. Nous utilisons par conséquent un capteur de pression pour connaître la tension interfaciale à l'apex de la bulle. Alors que le module interfacial de compression des monocouches est de l'ordre de 20 mN/m, nous avons mesuré pour la tricouche PAA-0.7-C_{12}-PVP-PMAA un module interfacial de compression de l'ordre de 1000 mN/m.

(a) PAA-0.7-C_{12}-PVP-PAA.

(b) PAA-0.7-C_{12}-PVP-PMAA.

Figure 6: Profil des gouttes lors de la compression de l'interface dans le cas de tricouches (lecture de gauche à droite puis de haut en bas). L'analyse du profil permet de mettre en avant le caractère viscoélastique de l'interface dans le cas du PAA-0.7-C_{12}-PVP-PMAA qui combine un fort ancrage des polymères à l'interface, des liaisons hydrogènes et des interactions hydrophobes.

Géométries complémentaires

Pour déterminer l'importance relative de la compression et du cisaillement lors de la compression de l'interface d'une bulle, nous avons effectué des expériences de pure compression (sans changement de forme, grâce à une cuve radiale) et de pure cisaillement (sans changement de surface, grâce à un rhéomètre interfacial de cisaillement), en collaboration avec M. Pepicelli, B. Schroyen et M. Nagel du groupe de J. Vermant.

Nous nous sommes concentrés dans cette étude sur les bicouches de PVP-PMAA à l'interface eau/air. Nous avons mesuré un module élastique de cisaillement élevé ($G' \sim 200$ mN/m), et un module visqueux de cisaillement plus faible ($G'' \sim 50$ mN/m), comme illustré sur la Figure 7.

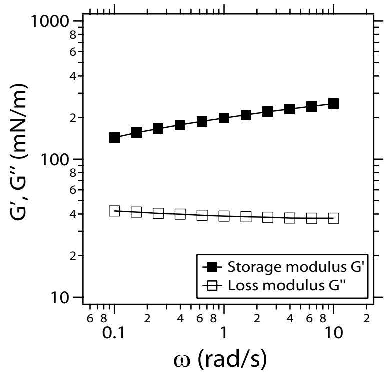

Figure 7: Modules de cisaillement de bicouche PMAA/PVP à l'interface eau/air en fonction de la fréquence mesurés grâce à un rhéomètre interfacial de cisaillement.

Cependant, lors de la compression, le module mesuré est plus faible et très proche du module mesuré en goutte pendante ($K \sim 100$ mN/m). Nous en concluons qu'en goutte pendante grâce à la haute symétrie de l'apex de la bulle, les mesures effectuées à cet endroit précis correspondent à de la pure compression. En effet, la composante de cisaillement est importante dans une zone localisée à la base de la bulle, loin de la zone de mesure.

Production et caractérisation de microcapsules par microfluidique

Ces résultats sur des interfaces modèles nous ouvrent la route pour fabriquer des microcapsules aux propriétés contrôlées. De plus, ces mesures sont une première étape vers des mesures rhéologiques in-situ sur les microcapsules. Grâce à la microfluidique, nous sommes capables de fabriquer des microcapsules de manière bien contrôlée et de mesurer leurs propriétés rhéologiques in-situ.

Production microfluidique de microcapsules en couche par couche

La microfluidique nous offre un grand contrôle sur les flux à l'intérieur des canaux microfluidiques, et la lithographie douce nous laisse une grande liberté dans le design des puces microfluidique. La fabrication des microcapsules s'effectue dans une puce en PDMS (poly(dimethyl siloxane)) et se décompose en trois étapes : la production des gouttes d'huile qui constitueront le cœur de nos capsules, l'adsorption des polymères à l'interface, et le rinçage des capsules pour ajouter de nouvelles couches.

Production des gouttes : les capsules sont produites à partir de gouttes d'huile minérale formées grâce à un dispositif de focalisation hydrodynamique. Ce dispositif, simple à mettre en œuvre, offre une très bonne monodispersité. Ainsi nous produisons des gouttes d'huiles de $50\,\mu$m de diamètre.

Adsorption du polymère : les gouttes sont produites directement dans une solution de polymère. Un long canal laisse le temps au polymère de s'adsorber à l'interface. La géométrie de la puce a été optimisée pour que ce long canal n'offre pas trop de résistance hydrodynamique relativement aux autres parties de la puce.

Rinçage des capsules : la première étape consiste à extraire les capsules de la solution de polymère et à les transférer dans une solution de rinçage (solution sans polymère à pH 3). Pour cela, la solution de polymère avec les capsules et la solution de rinçage sont mis en contact et poussées à travers un canal étroit, comme illustré sur la Figure 8. Grâce au contrôleur de pression, les débits des deux solutions sont ajustées pour que les capsules soient au contact des parois tout en ayant leur centre de masse dans la solution de rinçage. Ainsi, lorsque les solutions sont séparées, les capsules suivent la solution de rinçage. Le même protocole est reproduit pour transférer les capsules dans une seconde solution de polymère pour adsorber une seconde couche.

Ainsi, il est possible de fabriquer des capsules avec plusieurs couches de polymère. Dans cette étude nous nous sommes limités à deux couches. Les capsules sont ensuite envoyées dans une seconde puce microfluidique au fur et à mesure de leur production pour mesurer les propriétés rhéologiques de leur membrane.

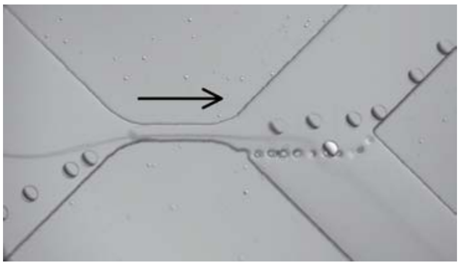

Figure 8: Trajectoire d'une capsule depuis la solution de polymère vers la solution de rinçage. La largeur du canal central est de 70 μm.

Caractérisation de la rhéologie interfaciale des capsules

Dans une seconde puce microfluidique plus rigide, les capsules sont déformées par des contraintes visqueuses. L'analyse de cette déformation, associée au calcul des contraintes appliquées sur la capsule permet d'estimer certains paramètres rhéologiques de la membrane.

Deformation des capsules : les capsules sont poussées dans un canal où elles sont légèrement confinées en largeur, selon le design développé par le groupe de J.-C. Baret[3]. Lorsque le canal s'élargit brusquement, le fluide envahit toute la largeur de la chambre comme illustré sur la Figure 9 par des traceurs, induisant des contraintes visqueuses qui tendent à étirer latéralement les capsules. Les capsules, initialement comprimées latéralement tendent donc à s'étirer puis à récupérer leur forme sphérique grâce à la tension interfaciale. La rapidité du phénomène nous empêche de capturer plus qu'une dizaine de points par capsule. Cependant, le grand nombre de capsules produites et l'homogénéité des conditions expérimentales pour les différentes capsules nous permettent de reconstituer l'évolution de la déformation avec un grand nombre de points.

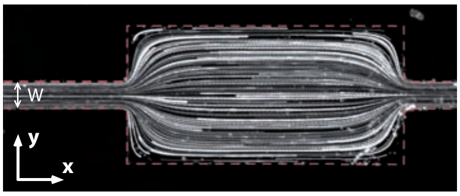

Figure 9: Lignes de courant du fluide dans la chambre de déformation. La divergence des lignes de courant à l'entrée de la chambre crée des contraintes visqueuses qui déforment la capsule lors de son passage. La largeur du canal d'entrée est $W = 80\,\mu$m. Les lignes de courants sont matérialisées grâce à des traceurs fluorescent de 5 μm de diamètre.

Evaluation de la contrainte à l'interface : la détermination de la contrainte appliquée sur l'interface de la capsule est nécessaire à l'évaluation des propriétés rhéologiques de la capsule. Cependant, la présence même de la capsule rend le calcul de l'écoulement et donc celui des contraintes très complexe. Pour cette raison, nous avons effectué des simulations numériques en éléments finis pour déterminer ces contraintes en tout point de l'interface, pour chaque position de la capsule, et pour chaque expérience.

---

[3] Brosseau, Q., Vrignon, J. and Baret, J.-C. Microfluidic Dynamic Interfacial Tensiometry (μDIT). Soft Matter 10, 3066–76 (2014).

Analyse de la relaxation de la capsule : la connaissance des contraintes appliquées sur l'interface nous permet d'évaluer la déformation théorique de la capsule en fonction de sa position au moyen d'un modèle. La littérature propose deux modèles correspondant à deux cas extrêmes. Le premier[4] décrit le cas où la membrane présente une tension interfaciale homogène, isotrope, et indépendante de la déformation, alors que le second[5] décrit le cas où la membrane présente uniquement une tension élastique. Le premier modèle décrit bien les monocouches de PMAA comme illustré sur la Figure 10 et nous permet d'en extraire un temps de relaxation caractéristique correspondant à une tension interfaciale de 40 mN/m relativement proche de ce qui a été mesuré en goutte pendante.

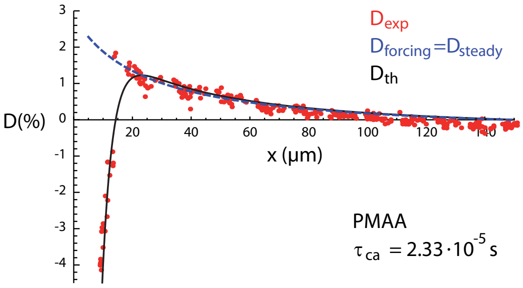

Figure 10: Déformation d'une capsule (D_{steady}) en fonction de sa position dans la chambre (x). La membrane consiste en une monocouche de PMAA. La ligne bleue représente le forçage due aux forces visqueuses du fluide extérieur (D_{forcing}), et la ligne noire la prédiction théorique de la déformation (D_{th}). Le calcul de D_{th} est fait pour une tension interfaciale de 40 mN/m, amenant à un temps de relaxation $\tau_{\text{ca}} = 2.33 \cdot 10^{-5}$ s.

Cependant, les expériences en géométrie modèle nous ont montré que les hypothèses de ce premier modèle ne sont en général pas vérifiées, sans toutefois que nos membranes puissent être considérées comme des membranes purement élastiques. De plus, ces deux modèles ne nous permettent pas de décrire les déformations mesurées dans nos puces microfluidiques. Ainsi nous avons proposé un modèle prenant en compte la composante isotrope de la tension interfaciale, et la viscoélasticité de la membrane. Ce modèle nous a permis d'interpréter les comportements observés pour les monocouches de PAA-0.7-C_{12}, et les bicouches PMAA/PVP et PAA-0.7-C_{12}/PVP, et d'en extraire des temps caractéristiques de relaxation cohérents avec les expériences macroscopiques modèles.

Conclusion

Dans un premier temps nous avons utilisé la géométrie modèle qu'est la bulle montante (inverse de la goutte pendante) pour étudier indépendamment les différents phénomènes impliqués dans l'assemblage des multicouches et dans leur déformation. Nous avons revisité différents modèles classique pour décrire l'adsorption de nos polymères à l'interface, puis nous avons mesuré les modules interfaciaux de différents systèmes de polymères. Pour cela, à l'aide de mesures complémentaires, nous avons établi un cadre pour les mesures de modules élastiques en goutte pendante.

---

[4] Taylor, G. I. The Formation of Emulsions in Definable Fields of Flow. Proc. R. Soc. A Math. Phys. Eng. Sci. 146, 501–523 (1934).

[5] Barthes-Biesel, D. and Rallison, J. M. The time-dependent deformation of a capsule freely suspended in a linear shear flow. J. Fluid Mech. 113, 251 (1981).

Dans un second temps, nous avons utilisé la microfluidique pour fabriquer différents types de micro-capsules et pour mesurer leurs propriétés mécaniques. Celles-ci résultent des différents phénomènes étudiés dans la première partie de cette thèse. Nous avons établi un modèle et effectué des simulations numériques qui nous permettent d'extraire les principales propriétés interfaciales de nos capsules à partir de la mesure de leur déformation dans les canaux microfluidiques.

Introduction

The precise control of the delivery of chemicals at the micro- or even nano-scale is a major concern when using various kinds of compound such as detergents, pesticides and drugs. In order to improve control over the delivery, industries seek a way to encapsulate the chemicals. Nature provides plenty of examples of micro- and nano-containers: viruses to transport DNA or RNA fragments inside the host cells; sperm cells to transport chromosomes to the ovule; or red blood cells to transport hemoglobin and thus oxygen to every cell of the body. These examples in nature have one common feature: an inner core is isolated from the environment by one or more layers of proteins or lipids. Moreover, they are specifically adapted to their use and environment. A route toward artificial micro-containers is to mimic this common structure by enclosing the chemical compound into a polymeric membrane: such objects are called micro-capsules.

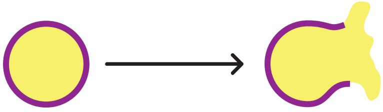

This thesis is focused on a method to produce artificial micro-capsules by assembling several layers of polymer at the interface of an oil droplet or an air bubble, as shown in the figure below. The polymers are dissolved in the water and they are chosen to adsorb spontaneously at the interface of the drop/bubble. As for the natural examples, the capsules have to be adapted to the specific conditions corresponding to their use. It is therefore crucial to know how to tune the capsules properties. For instance, the membrane stiffness must be carefully adjusted: it should be stiff enough to protect the chemical during transport and soft enough or breakable to enable the release under stimulus.

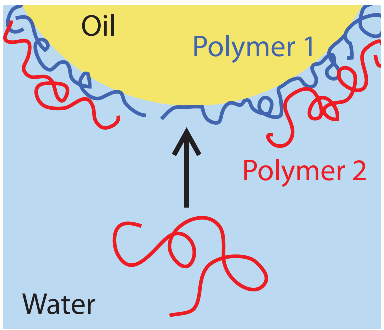

In this thesis, we focus more specifically on the building process of such membrane, on the measurement and the control of its mechanical properties, and finally on the assembly and probing of large populations of micro-capsules.

Assembly

The adsorption of the polymer layers being spontaneous, a fine understanding of the adsorption dynamics is crucial to control the quantity of polymer at the interface. More precisely, our goal is to determine what mechanism rules the adsorption kinetics, and how we can tune it. Our levers of control are the chemical structure of our polymer chains, and the balance between the hydrophilic and the hydrophobic groups of the chain. As a first step, in order to study these general adsorption mechanisms, we will work with a model interface: a pendant drop. This large and fixed interface offers more convenient handling and probing than micro-capsules dispersed in solution.

Interfacial rheology

We will show that the mechanical (or rheological) properties of these model membranes can exhibit a large variety of behaviours, from the softest multilayers, similar to soapy interfaces, to the stiffest ones, which can wrinkle under compression. By varying the nature of the polymers, we tune the interactions of the polymers with each other and with the interface, and we can indeed explore all these rheological behaviours.

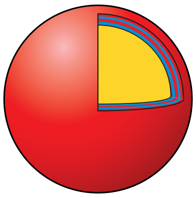

Microfluidic probing

The production of large populations of spherical micro-capsules of a few tens of micrometers requires fine control at the micro-scale of all the fabrication steps: droplets formation, polymer adsorption, and all the intermediate steps. This is achieved by the design of microfluidic chips: a network of micro-channels which convey the liquids and the capsules to manage all the elementary operations.

Microfluidics also offers the right tools to individually handle the capsules to measure the rheological properties of their membranes. Using the viscosity of the water and the high shear rates allowed by microfluidics, we will stretch the capsules and observe how they deform in response. We will show that the different behaviours measured with model membranes are observed on real capsules.

I will first introduce the fundamental concepts of interfacial rheology, hydrodynamics and polymer physics linked to this work in Chapter 1. I will present in Chapter 2 how we measure and model the assembly and the interfacial rheology of model interfaces. I will first study the adsorption kinetics of monolayers and their behaviour under compression/dilatation. I will then explore the influence of the anchoring and interaction between polymers in the case of multilayers. In Chapter 3, I will expose how we produce micro-capsules in a microfluidic chip, and how we perform direct in-situ measurement of the rheological properties of these membranes. We will see how the capsule behaviour in such geometry is related to the membrane composition.

Chapter 1

Fundamental concepts and bibliography

Contents of this chapter

1.0 Introduction

In this chapter, I will introduce the concepts and the formalism that we need for this thesis. I will first present an overview of the different encapsulation methods that we can find in the literature.

Then I will introduce the concepts of interfacial tension and interfacial rheology which are central in this thesis. In the third part of this chapter, I will present the theoretical basis of the polymer physics. All these concepts will be used in Chapters 2 and 3, and necessary to rationalize our experimental observations.

1.1 Encapsulation

From food ingredients to drugs, a lot of chemicals need to be temporarily isolated from their environment before their delivery, or their action. The challenge is either to prevent any contact either with an aggressive environment, or or to prevent the environment to be contaminated by the chemical. In the former case, it could result in a degradation of the chemical and a decrease of its efficiency. In the later case, it could cause dangerous side effects on an ecosystem, or on the body for instance.

Moreover, some applications require to extend the duration of the delivery of a specific chemical. For instance, the perfume contained in the detergent must be released on a period of time as long as possible after the washing.

In some specific cases, one may wish to deliver the chemicals on a specific location to maximize the efficiency of the compounds. The application gathering most attention may be the targeted drug delivery. The principle is to inject a drug in the body which spontaneously concentrates in a specific area, where its action is needed.

A possible solution to overcome these three challenges is to encapsulate the chemical into small droplets protected by a membrane. The control of the membrane properties leads to a good control of the delivery of the enclosed chemical.

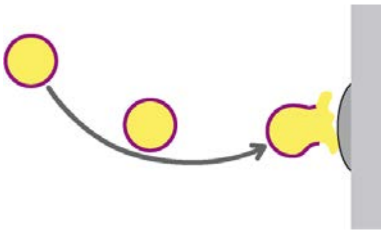

Figure 1.1: Isolation, transport and targeted delivery of a chemical.

1.1.1 What are the key properties that make a capsule efficient?

An efficient capsule meets three main requirements to be called so. It must show:

- good transport abilities,
- an efficient protection of the chemical from its environment,
- a controlled delivery of the chemical.

Moreover, numerous side effects can be avoided by the limitation of membrane-material accumulation after the release. To this aim, the membrane should be as thin as possible.

Transport of the capsules. In a complex media, the transport is easier for the smallest capsules. A smaller size provides to the capsules the ability to enter smaller pores and to slow down sedimentation. The use of capsules in the blood stream requires the size to be below $5\,\mu$m to prevent any thrombosis. This limitation is challenging and requires an extremely fine control of the monodispersity which is hard to achieve without microfluidic. Preventing the capsule from adhering to any surface they could encounter is also an overriding challenge. Raichur *et al.* [1] showed that the surface coverage of the capsule defines their adhesive properties, which can consequently be tuned.

Thus an efficient capsule must be small and must not adhere to the surfaces of the media.

Protection of the chemical. The protection of the chemical mostly consists in preventing any leakage of chemicals, from the environment into the capsule, or from the capsule toward the environment. Ideally, a perfectly impermeable membrane should prevent any flux through it, and thus any contact between the chemical and the environment.

Mun *et al.* [2] and Zeeb *et al.* [3] have shown that an elastic membrane is more efficient than a purely viscous one to prevent mass transfer through it. A leakage through the membrane would indeed lead to a volume change, which creates a compression or a dilatation of the membrane. Hence, if the membrane is rigid enough, the energy needed to deform it can be high enough to stop the flow through the membrane. As a consequence, the rheological properties of the membrane can limit the volume changes and thus any large flux through it.

Consequently, the efficiency of the protection strongly depends upon the mechanical properties of the membrane. These mechanical properties must therefore be finely controlled.

Targeted delivery of the chemical. There are two mains possibilities to face targeted delivery, represented in Figure 1.2: either a specific affinity of the capsule with the target area concentrates them in this area (Figure 1.2a), or a local stimulus triggers the release on the target (Figure 1.2b).

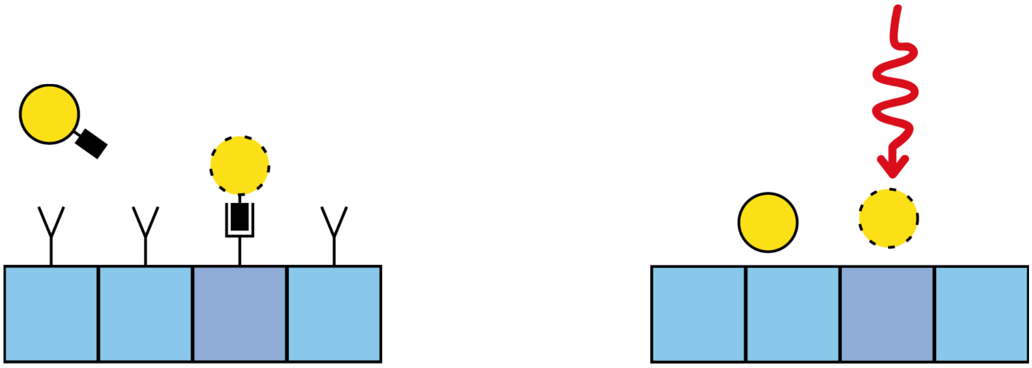

(a) Specific adhesion between the target and the capsule by using complementary chemical functions, represented by the triangles and the squares.

(b) Localized triggering of the delivery with a focused stimulus, represented by the red arrow.

Figure 1.2: Targeted delivery. The capsules (yellow) must deliver their content on the target only (dark blue square).

A spontaneous accumulation on the target can be met if the capsules show specific adhesion with the target. This is possible in biological systems, using for instance antibodies or other specific proteins, as presented in Figure 1.2a. Wang *et al.* [4] and Raichur *et al.* [1] have shown that a specific adhesion can be used to concentrate the capsules in a specific location, using the so-called key-lock type interactions, and especially the strong and specific biotin/streptavidin complex.

A local triggering of the delivery is possible if the capsule is stimuli responsive, as reported by Delcea *et al.* [5], and if the stimulus can be local, as illustrated in Figure 1.2b. This stimulus can be visible or infrared light [6], ultrasound beams [7, 8], or magnetic beam [9, 10].

In any case, the toughness of the membrane must be tuned to allow the delivery. Accordingly, the mechanical properties of the membrane are also preeminent to control the delivery of the compounds.

1.1.2 Main encapsulation methods

Several methods of capsule synthesis have been developed in the past few years [11], each of them presenting pros and cons. The future use of the capsule determines the priority requirement and thus, the synthesis method. We present here the main encapsulation methods present in the literature.

Interfacial polycondensation. The first method used to create elastic capsules is the interfacial polycondensation. It has been intensively studied in the last decades, especially by Rosenthal and Chang [12] and Rehage *et al.* [13, 14], and is commercially available, for instance in detergents.

This method consists in a chemical reaction of polymerization taking place at the interface between an oil droplet and the surrounding continuous water phase. Monomers are dissolved in the oil and they react with the water molecules to polymerize. The two reactants are in the two different phases, so they only meet at the interface. In this way, the reaction is localized, and a polymer network is exclusively created at the interface. This network can be then easily crosslinked to obtain a strong elastic membrane. When the network is chemically crosslinked, it is usually irreversible. Consequently, the ageing of the capsule is slow, and the elastic moduli can reach a few thousands of mN/m, as measured by Rehage *et al.* [14].

However, the toxicity of the monomers which remains in the oil is a barrier for many applications requiring a contact with living tissues. This is a very limiting disadvantage of the method.

Layer-by-layer (LbL) on solid substrates. To get rid of chemical reagents and initiators, Donath *et al.* and Caruso *et al.* [15, 16] developed a method to build spherical membrane around colloidal templates , as illustrated in Figure 1.3b. This process was adapted from the work of Decher *et al.* based on the physical interactions between the chains [17, 18]. The method of Decher consists in stacking layers of polymers on solid substrates, using physical attraction between the layers and the substrate. As illustrated in Figure 1.3a, the substrate is initially positively charged, in order to adsorb polyanions, which are of opposite charge. After rinsing the substrate to get rid of all the chains that are not adsorbed, a layer of positively charged polymers (polycations) is adsorbed on the first one. In this way, by alternating polycations and polyanions, the authors can add as many layers as needed.

In the case of LbL on colloids, by dissolving the colloidal core, the authors obtain an empty capsule which can be filled with the specified chemical. Layer-by-layer adsorption leads to well structured and well controlled membranes, but the process is complicated because of the necessary dissolution of the core.

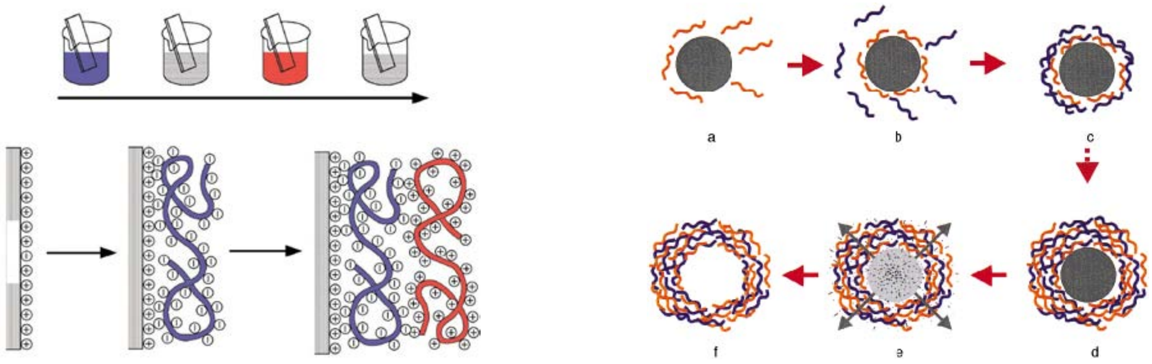

(a) Principle of the layer-by-layer adsorption of polymers on solid substrates: alternated dipping of the substrate in polyanions solution (blue), pure water (grey), polycations solution (red) (Figure from Decher *et al.* [18]).

(b) Step of fabrication of capsules using the LbL adsorption of colloidal particle. (Figure from Donath *et al.* [15])

Figure 1.3: Layer-by-layer adsorption of polyelectrolytes on solid substrates in two geometries: (a) on a planar macroscopic substrate; (b) on colloidal substrates.

LbL on liquid interfaces. To avoid the dissolution of the core (last steps in Figure 1.3b) and the refilling, it is possible to stack the layers directly on liquid droplets as presented in Figure 1.4. Klinlesorn *et al.* developed this method with polyelectrolytes for food applications [19]. The process has also been studied [20] with polymers interacting with hydrogen bonds.

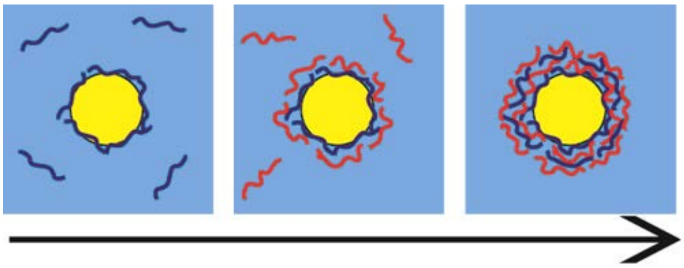

Figure 1.4: Main steps of fabrication of a multilayer membrane by LbL on liquid interface: droplets are created in a solution of amphiphilic polymers (blue) which therefore adsorb on the interface. The solution is rinsed to dispose of the chains which are not adsorbed, and a second polymer solution is added. The new polymer chains (red) adsorb because of their interaction with the first polymer. This interaction can be electrostatic [19] or due to hydrogen bonds [21]. Alternating rinsing and adsoption of polymers allows the assembling of as many layers as needed.

Although this method allows a more direct encapsulation, the manipulation of droplets raises new issues. Classical methods to produce emulsions consist in applying high shear rates to a biphasic system, which indeed usually lead to high polydispersity. Moreover, emulsions are known to be unstable: coalescence and coarsening can rapidly destroy the emulsion. Nevertheless, monodispersity and polymers at the interface bring more stability to the emulsions. Accordingly, LbL on liquid interfaces is the starting point of the synthesis of the capsules studied in this work.

Microfluidics. Microfluidics consists in well defined micron-sized channels conveying fluids and droplets, bubbles, cells, etc. The small size of the channels allows a good control of the flows. Microfluidics can be a powerful tool to produce capsules, allowing a fine control of all the steps of production, from the droplet formation, to the capsule manipulation. Hence, using microfluidics, finely structured droplets or objects can be produced [22].

Chu *et al.* and Abate *et al.* performed to create controlled multiple emulsions [23, 24] with a defined number of inner droplets in every larger droplet, as presented in Figure 1.5a. Although it is not properly capsules, it is a solution to isolate a chemical (in the inner droplets) from the environment. To build these multiple emulsions, the authors have faced four issues: the control of the size of the inner and outer droplets, the coalescence of the inner droplets, the coalescence of the outer droplets and the expulsion of the inner droplets outside the outer ones. These challenges have been overcome by a subtle choice of the surfactants, and by a fine control on the fluid dynamics that only microfluidics can offer.

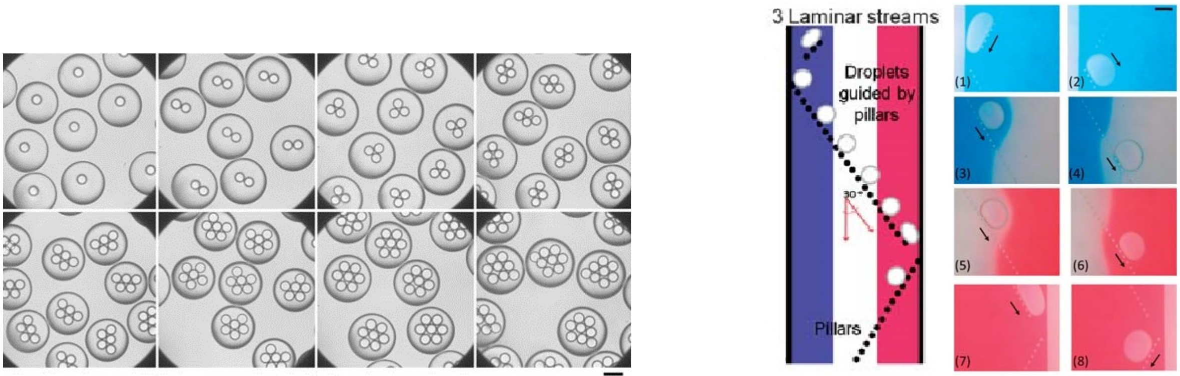

(a) Multiple emulsions of finely controlled structure, Chu *et al.* [23]. Scale bar is 200 μm.

(b) Coflow used by Kantak *et al.* to build LbL capsules [25] by alternating polyelectrolytes (blue and red) and washing solution (white). Scale bar is 200 μm

Figure 1.5: Examples of microfluidic production of micron-sized objects.

The high level of control brought by microfluidics can be applied for LbL capsules. Even so, building multilayers on droplets is far from straightforward, and various systems have been investigated [25, 26]. Kantak *et al.* designed a microfluidic chip to produce multilayers of polyelectrolytes on liquid droplets [25], which is presented in Figure 1.5b. Owing to the low Reynolds number, the authors set a coflow with three entries: polyelectrolyte 1 (blue), wash solution (white), polyelectrolyte 2 (red). This coflow is stable because of the predominant viscous effects, and the droplets are led through these three flows to adsorb the different layers.

Although microfluidics offers the possibility to finely control the size, the monodispersity and the structure of capsules, the implementation of such systems is not trivial.

Most of the encapsulation methods presented here consist in covering a micrometer-sized droplet with an elastic membrane. The mechanical properties of such droplets and capsules are mostly governed by the interface. We need therefore to present the fundamental concepts of interfacial rheology and its formalism, from classical interfacial tension to visco-elastic membranes. All these notions will indeed be needed later in this thesis.

To summarize this section:

Encapsulation is an ideal solution to control the diffusion, the protection, and the delivery of specific chemicals. The capsules efficiency strongly depends on the rheological properties of the membrane.

Several methods to produce capsules have been investigated in the last decades. Among them, the layer-by-layer adsorption of polymers on liquid interfaces allows a good control of the membrane composition. Furthermore, microfluidics should allow an easy manipulation of the droplets to build model capsules of known composition.

These model capsules are the necessary starting point for a fine study of the link between the composition and the rheological properties of the capsules.

1.2 Interfacial tension and interfacial rheology

In this section, I will introduce the physical concept of interfacial tension between two pure immiscible fluid phases. I will show that at the length scale of the capsules, interfacial tension is indeed dominating the volume forces, as gravity for instance. I will present the behaviour of a pure interface, the response of an interface covered by small molecules of surfactants, and finally the general frame of interfacial rheology. In a second step, I will present how we can measure the interfacial properties of droplets by deforming them in microfluidic experiments.

All the concepts and studies presented here consider an ideal interface, which requires two assumptions.

- An ideal interface is smooth (no roughness): we neglect surface fluctuations due to thermal noise. In reality, these fluctuations are fast and of the order of the Angström [27]. At the scale of the polymer network, they are neglected.
- An ideal interface has no thickness: the interface is a two-dimensional mathematical object with its own properties. In reality, the intensive properties (e.g. density) are continuous, and evolve from the two bulk values on a length of a few nanometers [28]. The interfacial quantities (surface concentration, surface energy, etc) usually results from the integration of the difference between the real continuous profile and the ideal step model, as illustrated in Figure 1.6.

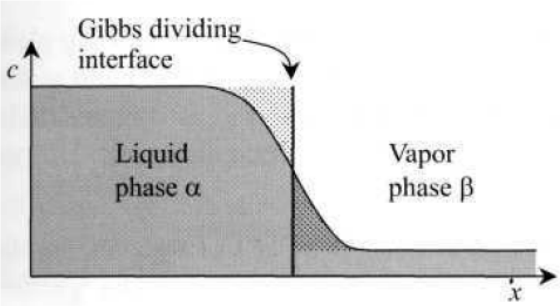

Figure 1.6: Intensive quantities (here concentration c) are continuous through all the thickness of the interface. According to Gibbs formalism, the interface is fixed at a given position with no thickness: intensive quantities follows a step transition between the bulk values. The algebraic dotted area represent the surface concentration, which is zero in this case. Figure adapted from [29].

1.2.1 Definition of interfacial tension

Let us consider a droplet of oil in a bath of water. Most of the time, oil does not mix with water: the two phases are qualified as immiscible phases. At an interface by definition, there is a contact between different molecules, as shown in Figure 1.7a. This contact between molecules of two immiscible phases implies that an interface costs energy. This surface energy E_S is proportional to the area A of the interface, and we call γ the proportionality factor, which is called *interfacial tension*:

$$E_\mathrm{S} = \gamma_\mathrm{ow} \cdot A \quad . \tag{1.1}$$

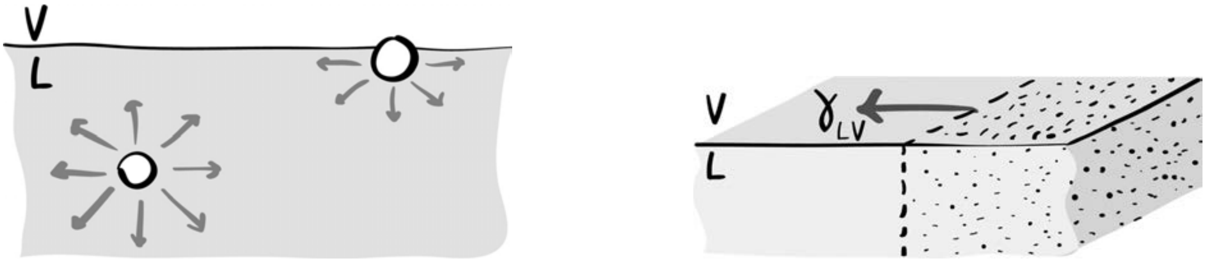

(a) Surface energy between two phases (here: liquid (L) and vapor (V)) is due to some missing interactions for the molecules at the interface.

(b) Interfacial tension can be interpreted as a force per unit length of one subsystem on the other (the dotted region). The force is orthogonal to the contact line, and parallel to the interface.

Figure 1.7: Molecular interpretation of interfacial tension (Figure from Marchand *et al.* [30]).

Because of interfacial tension, a two-phase system spontaneously tends toward the situation which minimizes the total interfacial area. Consequently, without external force, drops at rest are always spherical. This can be observed in microgravity, as it was represented by Hergé in Figure 1.8.

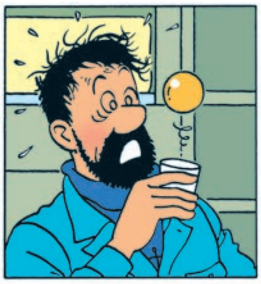

Figure 1.8: In microgravity, the shape of the liquid phase (here, the whiskey) is set to minimize its area with air, which leads to a sphere. (©Hergé/Moulinsart 2016)

Interfacial tension depends on the two phases in contact, and on the temperature. It is an energy per unit area, but its common unit is *Newton per meter* N/m. Indeed, an interfacial tension is also a force per unit length. If we consider a subsystem containing a portion of the interface, as illustrated in Figure 1.7b, we can define the line which delimits the portion of the interface included in the subsystem. Along this line, on a small segment of length $\mathrm{d}l$, the subsystem is submitted to a traction force $\mathrm{d}f$ parallel to the interface and orthogonal to the line, whose value is $\mathrm{d}f = \gamma \cdot \mathrm{d}l$. A more detailed description of this force in the frame of a continuous interface (as presented in Figure 1.6) is presented by Pozrikidis [31].

Interfacial tension being a force per unit length, it affects the pressure on both sides of the interface. For every point M of a surface, we can define two radii of curvatures along two orthogonal directions of the surface, and define the two radii of curvature R_Φ and R_ξ in M, as illustrated in Figure 1.9. The Young-Laplace law states:

$$\Delta P = P_{\mathrm{in}} - P_{\mathrm{out}} = \gamma \cdot \left(\frac{1}{R_\Phi} + \frac{1}{R_\xi} \right) \quad , \tag{1.2}$$

where P_{in} and P_{out} are the pressure in both regions separated by the interfaces, R_Φ and R_ξ are the two radii of curvature defined in Figure 1.9.

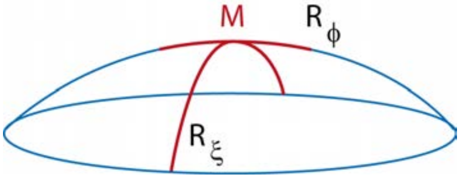

Figure 1.9: The pressure difference between both sides of the interface is defined by interfacial tension and the two radii of curvature of the surface.

In a gravity field, the weight is $F_\mathrm{g} = \rho V g$, where ρ is the density, V the volume, and g is acceleration of gravity. If we call L the typical length scale of the system, we can write that the surface force associated to it is: $F_\mathrm{S} \sim \gamma L$. Hence, writing that $V \sim L^3$, the ratio of these forces is:

$$\frac{F_\mathrm{g}}{F_\mathrm{S}} \sim \frac{\rho g}{\gamma} \cdot L^2 \quad . \tag{1.3}$$

This dimensionless quantity characterizes the relative predominance of one effect on the other. It is called the *Bond number* $\mathcal{B}o = \frac{\Delta\rho\, g\, L^2}{\gamma}$ in the general case, where $\Delta\rho$ is the density difference of the phases in contact. A high Bond number indicates predominance of gravity over interfacial tension effects and vice-versa. We see from equation (1.3) that the relative importance of gravity and interfacial tension strongly depends on the size of the objects. We introduce the capillary length L_c for which the two effects have similar amplitude ($\mathcal{B}o = 1$):

$$L_\mathrm{c} = \sqrt{\frac{\gamma}{\rho g}} \quad . \tag{1.4}$$

When the typical size of the system L is greater than L_c, gravity overcomes interfacial tension. In the specific case of pendant droplets, gravity deforms them which consequently look more elongated than spherical. Otherwise, when $L < L_\mathrm{c}$, droplets are almost spherical, and in most cases we can neglect gravity effects. When buoyancy takes place, ρ is replaced by $\Delta\rho$ in equation (1.4). In the case of droplets of water in air, $\gamma = 72\,\mathrm{mN/m}$, and $L_\mathrm{c} \sim 3\,\mathrm{mm}$. For water and oil systems, L_c is of the same order of magnitude. Consequently, in microfluidics, we will always neglect the gravity (and buoyancy) effects.

1.2.2 Methods to measure interfacial tension

I present here two methods commonly used to measure interfacial tension: the Wilhelmy plate, and the pendant-drop experiment.

1.2.2.a Wilhelmy plate

In this apparatus, a thin plate is placed to touch the interface between the liquid and the gas, as presented in Figure 1.10a. The interface applies a force all along the contact line with the plate. If $\mathcal{P}$ is the perimeter of the plate, the force F measured on the plate is:

$$F = \mathcal{P} \cdot \gamma \cdot \cos\theta \quad , \tag{1.5}$$

(a) The Wilhelmy plate touches the interface to create a meniscus. The meniscus applies a force on the plate proportional to interfacial tension.

(b) The shape of the pendant drop results from a balance between the Laplace pressure (Equation (1.2)) and the hydrostatic pressure.

Figure 1.10: Two methods to measure an interfacial tension: the Wilhelmy plate and the pendant-drop experiment.

where θ is the contact angle of the liquid on the solid. Usually, the plate is used in complete wetting conditions ($\cos\theta = 1$). The measurement of the force F is thus a direct measurement of the interfacial tension.

1.2.2.b Pendant drop

This method is presented for a drop of liquid in a gas, but it can also be used for a bubble of air in a liquid, or a drop of a liquid in another immiscible liquid. When the Bond number is close to $\mathcal{B}o = 1$, the shape of the droplet results in a balance between hydrostatic pressure which pulls on the droplet to elongate it, and interfacial tension, which tends to keep the droplet spherical. By balancing hydrostatic pressure with Laplace pressure (Equation (1.2)), we can numerically calculate the theoretical shape of the droplet, depending on its interfacial tension with the surrounding gas. The measured profile of the droplet can be fitted with the calculated profiles, with the interfacial tension γ as fitting parameter.

This method is less direct than the Wilhelmy-plate method, but it requires small amounts of liquid. Moreover the interface can be easily deformed by varying the volume of the droplet. This method will be described in more detail in Section 2.1

1.2.3 Interfacial tension with surfactants

As soon as one phase is not pure, more complex behaviours can be observed if one of the compounds of the two phases adsorb at the interface.

Most of the time in two-phase systems, one phase is polar (e.g., water), and one is non-polar (e.g., an oil or a gas). This difference in polarity causes the two phases to be non miscible. Consequently, a small molecule as presented in Figure 1.11a presenting a polar region (e.g., a charge) (in blue in Figure 1.11a) and a organic non-polar one (e.g., a long alkyl chain) (in orange in Figure 1.11a) often has a good affinity with both phases: it is *amphiphilic*. It is energetically favorable for it to adsorb at the interface between the two phases. This adsorption energy is typically of the order of $k_B T$, where k_B is the Boltzmann constant, ant T the temperature. Such a molecule is called a surfactant, and tends to stay at the interface, with the polar region (the *head*) in the water phase and the non-polar one (the *tail*) in the oil phase, as illustrated in Figure 1.11b.

The presence of such molecules at an interface decreases interfacial tension. We call Γ the surface excess, i.e. the number of surfactant molecules per unit area in molecules/m^2:

$$\Gamma = \frac{N_\mathrm{S}}{A} \quad , \tag{1.6}$$

where N_S is the number of molecules at the interface, and A the interfacial area.

The interfacial tension between the two pure phases commonly called γ_0, will be distinguished from the interfacial tension with surfactants: γ. Because of the presence of such molecules, we observe that $\gamma < \gamma_0$, and the shift of interfacial tension due to surfactants is called *surface pressure*, Π:

$$\Pi = \gamma_0 - \gamma \quad . \tag{1.7}$$

(a) A classic surfactant molecule is composed of a polar *head* (blue) and a non-polar *tail* (orange).

(b) At an interface, a surfactant molecule is oriented to present its polar head toward the polar phase (e.g. water), and its non-polar tail toward the non-polar one (e.g. oil).

Figure 1.11: Surfactant molecule and its arrangement at an interface.

As we will see, the behaviour of an interface in the presence of surfactants depends on the solubility of the molecules in the two phases. We can distinguish two cases:

- an *insoluble surfactant* shows slow exchanges between bulk and interface, and molecules can be considered as trapped at the interface in the time scale of the experiment,
- a *soluble surfactant* is soluble in at least one phase with fast exchanges between bulk and interface.

1.2.3.a Insoluble surfactants

Insoluble surfactants are trapped at the interface in the time scale of the experiment because of their poor solubility in the bulk phases (e.g. 1-dodecanol at an air/water interface), as illustrated in Figure 1.12a. Experimentally, they are most commonly spread on interfaces using a volatile solvent: the solvent containing the surfactants is spread at the air/water interface and the molecules spread on the interface as the solvent evaporates. In such experiments, the number of molecules is usually known, and thus the surface excess is a control parameter. Isotherms are usually represented with surface pressure Π as y-coordinate, defined by Equation (1.7), and the area per molecule $1/\Gamma$ as x-coordinate.

Surface excess can be controlled by compression of the interface with a barrier, as illustrated in Figure 1.12b.

(a) Insoluble surfactants are present only at the interface.

(b) When interface is compressed with a barrier, there is no exchange with the volume so the number of molecules at the interface remains constant.

Figure 1.12: Insoluble surfactants on an oil (yellow)/water (blue) interface: (a) at rest and (b) under interfacial compression.

For low surface excess Γ of neutral molecules, surface pressure Π is proportional to Γ:

$$\Pi = k_{\mathrm{B}} T \cdot \Gamma \quad , \tag{1.8}$$

where k_{B} is the Boltzmann constant, and T the temperature. Equation (1.8) can be compared with the ideal gas equation, where pressure P is proportional to concentration c: $P = RT \cdot c$, where R is the gas constant.

For higher surface excess, phase transitions are observed during which surface pressure is constant. For further compression, when the phase transition is over, surface pressure rises again.

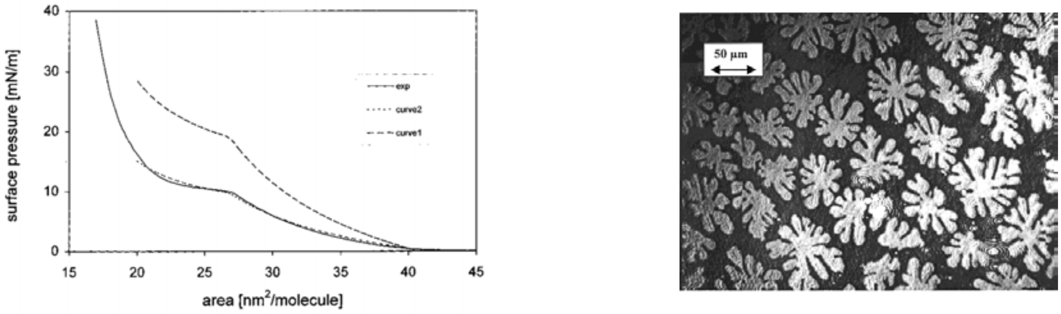

(a)

(b)

Figure 1.13: (a) Isotherm of 1-dodecanol at air/water interface. Dashed lines are the theoretical curves (for two possible molecular organization: individual molecules for the upper one, and dimers of molecules for the lower one), and the solid line is the experimental one. Surface pressure increases during compression (from right to left), which means that the interfacial tension decreases. The break point at $27\,\mathrm{nm}^2$/molecule and the plateau are the signature of a phase transition of the molecules at the interface. (b) Picture of the interface under Brewster angle microscopy (BAM), for area per molecule smaller than the $27\,\mathrm{nm}^2$/molecule break point. Figure from Vollhardt *et al.* [32].

The isotherm of molecules of dodecanol at the air/water interface has been measured by Volhardt *et al.* [32], and reported in Figure 1.13a. We observe that surface pressure decreases when the area per molecule increases, which means that the surface pressure increases during compression. Moreover, we observe a break point, and a plateau, which are the evidence of a phase transition in the surfactants organization at the interface, as visible in Figure 1.13b [32].

Interfacial tension decreases during compression, because of the increase of surface excess. This is possible only if the surfactant desorption time is significantly longer than the experiment. On the contrary, if adsorption and desorption time are significantly shorter than the experiment time, the behaviour is drastically different: this is the case of soluble surfactants.

1.2.3.b Soluble surfactants

Soluble surfactants (e.g., sodium dodecyl sulfate (SDS) in water) are characterized by the fact that they exhibit fast dynamics of exchange between the adsorbed state (at an interface) and the dissolved one (in water or oil). As a consequence, the equilibrium between these two states is quickly reached. Thus we consider that there is always an equilibrium between the number of adsorbed molecules N_S on the interface of area A, the molecules dissolved in the first phase (N_V^1 in a volume V_1) and the molecules dissolved in the second one (N_V^2 in a volume V_2). For the sake of simplicity, and because it is often the case in reality, we consider here the case in which the surfactants are soluble in only one phase (phase 1), as represented in Figure 1.14.

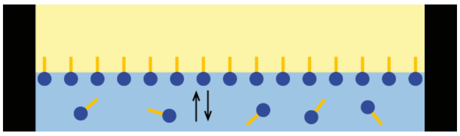

Figure 1.14: Soluble surfactants are present at the interface and in one phase at least. The exchange between surface and volume are fast enough to consider that there is a constant equilibrium between the interface and the volume.

1.2.3.c Interface at equilibrium

At equilibrium, at temperature T, we can write the interfacial Gibbs free energy G^S as a function of interfacial tension γ, surface area A, entropy S, and chemical potentials of different species i at the interface $\mu_\mathrm{i}^\mathrm{S}$ and the number of molecules N_i^S (there is no volume for the interface, and thus no $V\mathrm{d}P$ term):

$$\mathrm{d}G^\mathrm{S} = -S\,\mathrm{d}T + \gamma\,\mathrm{d}A + \sum_\mathrm{i} \mu_\mathrm{i}^\mathrm{S}\,\mathrm{d}N_\mathrm{i}^\mathrm{S} \quad . \tag{1.9}$$

Equilibrium leads to equal chemical potential in every phase and at the interface for a given component: $\mu_\mathrm{i}^\mathrm{S} = \mu_\mathrm{i}$. Moreover, at constant temperature, Equation (1.9) becomes:

$$\mathrm{d}G^\mathrm{S} = \gamma\,\mathrm{d}A + \sum_\mathrm{i} \mu_\mathrm{i}\,\mathrm{d}N_\mathrm{i}^\mathrm{S} \quad . \tag{1.10}$$

Then Equation (1.10) can be integrated owing to Euler's theorem [29], to write:

$$G_\mathrm{S} = \sum_\mathrm{i} \mu_\mathrm{i} N_\mathrm{i}^\mathrm{S} + \gamma A \quad . \tag{1.11}$$

Equation (1.11) can be differentiated:

$$\mathrm{d}G^\mathrm{S} = \sum_\mathrm{i} \mu_\mathrm{i}\,\mathrm{d}N_\mathrm{i}^\mathrm{S} + \sum_\mathrm{i} N_\mathrm{i}^\mathrm{S}\,\mathrm{d}\mu_\mathrm{i} + \gamma\,\mathrm{d}A + A\,\mathrm{d}\gamma \quad . \tag{1.12}$$

Difference between Equations (1.10) and (1.12) yields

$$0 = \sum_{\mathrm{i}} N_{\mathrm{i}}^{\mathrm{S}}\, \mathrm{d}\mu_{\mathrm{i}} + A\, \mathrm{d}\gamma \ \ , \tag{1.13}$$

which leads to the *Gibbs adsorption isotherm*:

$$\mathrm{d}\gamma = -\sum_{\mathrm{i}} \Gamma_{\mathrm{i}} \cdot \mathrm{d}\mu_{\mathrm{i}} \ \ . \tag{1.14}$$

We consider the case where only one kind of molecules is adsorbed ($i \equiv 1$). The equilibrium between the bulk at low concentration C_0 and the interface implies that the chemical potential is the same at the interface (μ_{S}) and in the bulk (μ_{V}):

$$\mu = \mu_{\mathrm{S}} = \mu_{\mathrm{V}} = \mu_0 + k_{\mathrm{B}} T \ln C_0 \ \ , \tag{1.15}$$

where k_{B} is the Boltzmann constant and μ_0 is a constant which only depends on the species and on temperature.

This leads to the following equation for the surface excess Γ:

$$\Gamma = -\frac{1}{k_{\mathrm{B}} T} \cdot \frac{\mathrm{d}\,\gamma}{\mathrm{d}\ \ln\, C_0} \ \ , \tag{1.16}$$

where γ is the interfacial tension, C_0 the bulk concentration, and T the temperature.

This equation can be used when interfacial tension, bulk concentration and their respective derivatives are known.

Several models exist to link interfacial tension γ and surface excess Γ. They are the results of a balance between adsorption and desorption processes, that will be described latter. We present here the Henry and the Langmuir isotherms.

Henry isotherm. In the Henry model, there is no interaction between the molecules, and the number of molecules which is possible to adsorb is infinite: these hypothesis are true at low concentration and surface excess. The surface excess is thus directly proportional to the bulk concentration:

$$\Gamma = K_{\mathrm{H}}\, C_0 \ \ , \tag{1.17}$$

where K_{H} is a constant called the Henry constant. Using Equations (1.14) and (1.17), we easily write the interfacial tension γ for neutral surfactants (for charged surfactants, there is a difference in the prefactor):

$$\gamma = \gamma_0 - k_{\mathrm{B}} T \cdot \Gamma \ \ , \tag{1.18}$$

where γ_0 is the interfacial tension with no surfactant ($\Gamma = 0$), k_{B} and T are respectively the Boltzmann constant and the temperature. Equation (1.18) is the same as Equation (1.8), and is a 2D analogue to the *ideal gas* Equation.

Langmuir isotherm. For higher concentrations, the *Langmuir* isotherm is used. In this model, surface excess is

$$\Gamma = \Gamma_\infty \left(\frac{K_\mathrm{L} C_0}{1 + K_\mathrm{L} C_0} \right) \quad , \tag{1.19}$$

where K_L is the Langmuir constant and Γ_∞ the surface excess upper limit. Hence, combining Equations (1.16) and (1.19), we write:

$$\gamma = \gamma_0 + k_\mathrm{B} T \Gamma_\infty \ln \left(1 - \frac{\Gamma}{\Gamma_\infty} \right) \quad . \tag{1.20}$$

1.2.3.d Adsorption dynamics

Surfactant adsorption dynamics can be diffusion controlled or kinetically controlled by an energy barrier [33].

Diffusion-limited adsorption: 1^{st} Ward and Tordai model. If there is no energy barrier to limit adsorption, in order to obtain the time-variation of the surface excess $\Gamma(t)$, one has to solve the diffusion equation:

$$\frac{\partial C}{\partial t} = D \frac{\partial^2 C}{\partial z^2} \quad , \tag{1.21}$$

where z is the direction orthogonal to the interface, $C(z,t)$ the local concentration close to the interface, and D the diffusion constant of surfactant molecules in the solvent. Moreover, mass conservation at the interface yields:

$$\frac{\partial \Gamma}{\partial t} = D \cdot \left(\frac{\partial C}{\partial z} \right)_{\mathrm{z=0}} \quad . \tag{1.22}$$

Integration of Equation (1.21) leads to the first Ward and Tordai Equation [34]. For short time, we neglect diffusion from the interface toward the bulk, and hence surface excess is:

$$\Gamma(t) = 2\, C_0 \cdot \sqrt{\frac{Dt}{\pi}} \quad . \tag{1.23}$$

According to Equations (1.18) and (1.23), interfacial tension is:

$$\gamma(t) = \gamma_0 - 2 k_\mathrm{B} T\, C_0 \cdot \sqrt{\frac{Dt}{\pi}} \quad . \tag{1.24}$$

Kinetically-limited adsorption: Henry model. When the surface excess becomes higher, adsorption and desorption are limited by energetic barriers E_ads and E_des, leading to adsorption and desorption constants k_ads and k_des which scale as:

$$k_\mathrm{ads/des} \propto \exp \left(- \frac{E_\mathrm{ads/des}}{k_\mathrm{B} T} \right) \quad . \tag{1.25}$$

The simplest adsorption model is described by the Henry model. It assumes an equilibrium between adsorbed molecules M_S, at the concentration Γ, and bulk molecules M_bulk at the concentration C_0. Adsorption transforms a bulk molecule M_bulk into an adsorbed molecule M_S:

$$M_\mathrm{bulk} \rightarrow M_\mathrm{S} \qquad \text{(Adsorption)} \quad , \tag{1.26}$$

and desorption transforms an adsorbed molecule M_S into a bulk molecule M_bulk:

$$M_\mathrm{S} \rightarrow M_\mathrm{bulk} \qquad \text{(Desorption)} \ . \tag{1.27}$$

The adsorption is described by Equation (1.26) and a kinetic constant k_ads, while the desorption is described by Equation (1.27) and a kinetic constant k_des. The adsorption rate v_ads and the desorption rate v_ads are thus equal to:

$$v_\mathrm{ads} = k_\mathrm{ads} \cdot C_0 \ , \tag{1.28}$$

$$v_\mathrm{des} = k_\mathrm{des} \cdot \Gamma \ . \tag{1.29}$$

The variation of the surface excess is the sum of the adsorption and desorption processes. Accordingly, the overall kinetics of the process is written:

$$\frac{\mathrm{d}\,\Gamma}{\mathrm{d}\,t} = v_\mathrm{ads} - v_\mathrm{des} = k_\mathrm{ads} \cdot C_0 - k_\mathrm{des} \cdot \Gamma \ . \tag{1.30}$$

Integration of Equation (1.30) yields:

$$\Gamma(t) = \Gamma_\mathrm{eq} + (\Gamma(t=0) - \Gamma_\mathrm{eq}) \cdot \exp\left(-k_\mathrm{des} t\right) \ , \tag{1.31}$$

where Γ_eq is the equilibrium surface coverage described by Equation (1.17) with $K_\mathrm{H} = \frac{k_\mathrm{ads}}{k_\mathrm{des}}$.

Kinetically-limited adsorption: Langmuir model. This model is more appropriate than the Henry model for high surface coverage. It is derived by another adsorption/desorption model developed by Langmuir [35]. The desorption is still described by Equation (1.27), whereas adsorption occurs when a bulk molecule M_bulk meets an empty spot S_empty at the interface. Adsorption transforms a bulk molecule M_bulk and an empty spot S_empty into an adsorbed molecule M_S:

$$M_\mathrm{bulk} + S_\mathrm{empty} \rightarrow M_\mathrm{S} \qquad \text{(Adsorption)} \ . \tag{1.32}$$

The adsorption rate is now:

$$v_\mathrm{ads} = k'_\mathrm{ads} \cdot C_0 \cdot \Gamma_\mathrm{empty} \ , \tag{1.33}$$

where Γ_empty is the surface concentration of empty spots, and k'_ads the kinetic constant. The overall number of adsorption spots is constant and called Γ_∞. It also represents the maximum surface excess which is possible to reach. Consequently,

$$\Gamma + \Gamma_\mathrm{empty} = \Gamma_\infty \ . \tag{1.34}$$

Using Equations (1.33) and (1.34), the adsorption rate is:

$$v_\mathrm{ads} = k'_\mathrm{ads} \cdot C_0 \cdot (\Gamma_\infty - \Gamma) \ . \tag{1.35}$$

Accordingly, the time-variation of surface excess is:

$$\Gamma(t) = \Gamma_\mathrm{eq,L} + (\Gamma(t=0) - \Gamma_\mathrm{eq,L}) \cdot \exp\left(-(k_\mathrm{des} + C_0 k'_\mathrm{ads}) \cdot t\right) \ , \tag{1.36}$$

where $\Gamma_{\mathrm{eq,L}}$ is the equilibrium surface excess described by Equation (1.19) in which the Langmuir constant is defined by $K_{\mathrm{L}} = \frac{k'_{\mathrm{ads}}}{k_{\mathrm{des}}}$.

When the kinetic constants are high, the equilibrium is quickly reached. Consequently, if a deformation of the interface is slowly applied, the interface maintains its equilibrium with the bulk, and the interfacial tension is constant.

Second Ward and Tordai model. When the surface excess is very high, the adsorption energetic barrier in Equation (1.25) depends on surface pressure. According to the second Ward and Tordai model [36], the energetic barrier corresponds to the interfacial area $\mathcal{A}$ which needs to be cleared to adsorb a new molecule:

$$E_{\mathrm{ads}} = \Pi \cdot \mathcal{A} \quad . \tag{1.37}$$

This dependency of the energetic barrier in surface pressure leads to slow logarithmic kinetics. This case will detailed further in Section 1.3.4.

1.2.4 Interfacial rheology, concept and measurements

1.2.4.a Interfacial tension in the general case

In the previous Section, we have discussed the fact that the non-miscibility of two fluids implies a surface energy at the boundary between the two fluid phases, and hence an interfacial stress (i.e. a force per unit length, in the plane of the interface). But interfacial stresses of various origins with several properties can also be observed. The study and the measurement of the interfacial stresses and their origins is the aim of interfacial rheology.

In the general case, the interfacial stresses are not isotropic and can be written as a tensor $\underline{\underline{T}}_{\mathrm{surface}}$. We can describe it as the sum of four canonical contributions:

$$\underline{\underline{T}}_{\mathrm{surface}} = \underline{\underline{T}}_{\mathrm{pure}} + \underline{\underline{T}}_{\Gamma} + \underline{\underline{T}}_{\mathrm{elastic}} + \underline{\underline{T}}_{\mathrm{viscous}} \quad , \tag{1.38}$$

where $\underline{\underline{T}}_{\mathrm{pure}}$, $\underline{\underline{T}}_{\Gamma}$, $\underline{\underline{T}}_{\mathrm{elastic}}$ and $\underline{\underline{T}}_{\mathrm{viscous}}$ represent respectively the interfacial tension between two pure phases (as presented in Section 1.2.1), the surface pressure due to surface excess (as presented in Section 1.2.3), the elastic and the viscous responses of the interface. We describe them in details below. Note that other effects, such as electro-magnetic stresses (e.g. Maxwell tensor) for instance, could be added to the list above if needed.

The interfacial tension between two pure phases is isotropic, as presented in Section 1.2.1:

$$\underline{\underline{T}}_{\mathrm{pure}} = \gamma_0 \cdot \underline{\underline{\mathbb{1}}} \quad , \tag{1.39}$$

where $\underline{\underline{\mathbb{1}}}$ is the identity tensor. Most of the time this component is constant upon compression (apart from the specific case of the Shuttleworth effect studied by Andreotti and Snoeijer [37]) and only depends on temperature.

The osmotic component is the surface pressure Π defined by Equation (1.7). It is also isotropic (in 2D) and depends on the surface excess Γ (and thus on area changes) as presented in Section 1.2.3, Equation (1.8):

$$\underline{\underline{T}}_{\Gamma} = -\Pi(\Gamma) \cdot \underline{\underline{\mathbb{1}}} \quad . \tag{1.40}$$

The elastic tension varies linearly with the strain tensor $\underline{\underline{\epsilon}}$ (defined in Section 1.2.4.b):

$$\underline{\underline{T}}_{\text{elastic}} = f(\underline{\underline{\epsilon}}) \quad , \tag{1.41}$$

where f is a function which depends on the chosen elastic model, as discussed later.

The viscous tension varies linearly with the strain-rate tensor $\underline{\underline{d}}$ (defined in Section 1.2.4.b):

$$\underline{\underline{T}}_{\text{viscous}} = g(\underline{\underline{d}}) \quad , \tag{1.42}$$

where g is a function which depends on the chosen viscous model, as discussed later.

The elastic and viscous tensions $\underline{\underline{T}}_{\text{viscous}}$ and $\underline{\underline{T}}_{\text{elastic}}$ are generally not isotropic, in contrast to $\underline{\underline{T}}_{\text{pure}}$ and $\underline{\underline{T}}_{\Gamma}$. Accordingly, we will refer to $\underline{\underline{T}}_{\text{viscous}}$ and $\underline{\underline{T}}_{\text{elastic}}$ as the *deviatoric components* of the interfacial stress.

Depending on the model used to describe the interface, some of these four components may be neglected. Below we discuss several specific cases summarized in Table 1.1.

	$\underline{\underline{T}}_{\text{pure}}$	$\underline{\underline{T}}_{\Gamma}$	$\underline{\underline{T}}_{\text{elastic}}$	$\underline{\underline{T}}_{\text{viscous}}$
Model 1	✓	0	0	0
Model 2	✓	✓	0	0
Model 3	✓	✓	✓	0
Model 4	✓	✓	✓	✓

Table 1.1: Depending on the model chosen to describe the interface, some surface stress components are considered (✓) and some are neglected (0).

The model 1 is used to characterize an interface between two pure phases. This case has been presented in Section 1.2.1. The model 2 can be used for interfaces covered by small surfactant molecules as presented in Section 1.2.3. The model 3 is relevant for instance for interfaces covered by polymers which are chemically cross-linked, and the model 4 typically for interfaces covered by physically cross-linked polymers.

Before introducing the models 2, 3 and 4, we need to detail the strain and strain-rate tensors.

1.2.4.b Strain and strain-rate

For a given deformation of the interface, we define the displacement $\underline{\xi}$ at every position M as follows:

$$\underline{\xi}(M) = \underline{OM} - \underline{OM}_{\text{initial}} \quad , \tag{1.43}$$

where the point O is the origin.

The deformation $\underline{\underline{\epsilon}}$ is defined from the displacement $\underline{\xi}$ through:

$$\underline{\underline{\epsilon}} = \frac{1}{2}\left(\underline{\underline{\mathrm{grad}}}\,\underline{\xi} + (\underline{\underline{\mathrm{grad}}}\,\underline{\xi})^{\top}\right) \quad . \tag{1.44}$$

Similarly, knowing the velocity field $\underline{u}(M)$, we define the strain-rate $\underline{\underline{d}}$:

$$\underline{\underline{d}} = \frac{1}{2}\left(\underline{\underline{\mathrm{grad}}}\,\underline{u} + (\underline{\underline{\mathrm{grad}}}\,\underline{u})^{\top}\right) \quad . \tag{1.45}$$

We define:

$$\dot{\underline{\underline{\epsilon}}} = \frac{\mathrm{d}\,\underline{\underline{\epsilon}}}{\mathrm{d}\,t} = \underline{\underline{d}} \quad . \tag{1.46}$$

We detail here how to model two elementary deformation fields: shear deformation and compression/dilatation. Every deformation can locally be decomposed as the superposition of a shear transformation and a pure compression/dilatation.

The shear deformation is characterized by the conservation of the area, and the change of shape illustrated in Figure 1.15. The scalar strain ϵ_{shear} is defined as follows:

$$\epsilon_{\text{shear}} = \frac{\Delta l}{h} \quad , \tag{1.47}$$

where Δl is the displacement, and h the corresponding height.

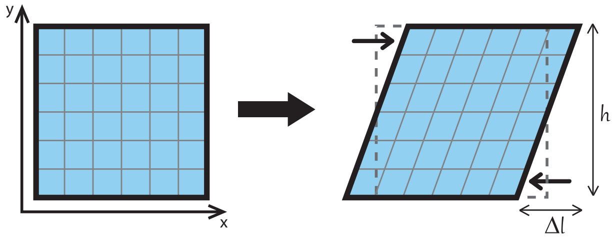

Figure 1.15: Pure shear of the interface: the angles are changed, but the area is preserved.

In this configuration, the strain tensor is written:

$$\underline{\underline{\epsilon}} = \frac{\epsilon_{\text{shear}}}{2} \cdot \begin{bmatrix} 0 & 1 \\ 1 & 0 \end{bmatrix} \quad . \tag{1.48}$$

We note here that in a frame of reference rotated by $\frac{\pi}{4}$, the strain tensor can be written:

$$\underline{\underline{\epsilon}} = \frac{\epsilon_{\text{shear}}}{2} \cdot \begin{bmatrix} 1 & 0 \\ 0 & -1 \end{bmatrix} \quad . \tag{1.49}$$

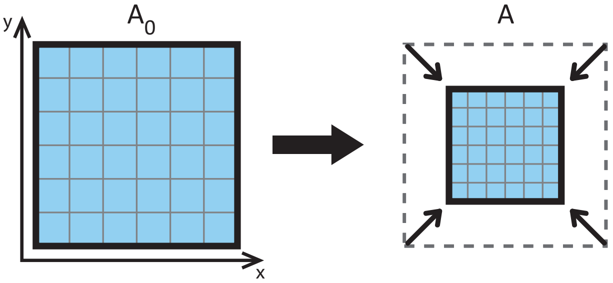

Figure 1.16: Pure compression of an interface: the area changes, but the shape is homothetically preserved.

The compression/dilatation of an interface is characterized by a homogeneous change in the area of the sample, as illustrated in Figure 1.16. The strain in compression/dilatation is defined by the variation of interfacial area A:

$$\epsilon_{\mathrm{dil}} = \frac{\Delta A}{A_0} \quad , \tag{1.50}$$

where A_0 is the initial area.

In this configuration, the strain tensor is:

$$\underline{\underline{\epsilon}} = \frac{\epsilon_{\mathrm{dil}}}{2} \cdot \begin{bmatrix} 1 & 0 \\ 0 & 1 \end{bmatrix} = \frac{\epsilon_{\mathrm{dil}}}{2} \cdot \underline{\underline{\mathbb{1}}} \quad . \tag{1.51}$$

In the general case, an in-plane deformation can always be decomposed as the sum of a compression/dilatation $\underline{\underline{\epsilon}}_{\mathrm{dil}}$ and a shear deformation $\underline{\underline{\epsilon}}_{\mathrm{shear}}$, as we show below.

We can see in Equation (1.44) that by construction, the strain tensor is symmetric. Accordingly, an arbitrary deformation can be written as follows:

$$\underline{\underline{\epsilon}} = \begin{bmatrix} a & c \\ c & b \end{bmatrix} \quad , \tag{1.52}$$

which can be written:

$$\underline{\underline{\epsilon}} = \frac{a+b}{2} \cdot \underline{\underline{\mathbb{1}}} + \begin{bmatrix} \frac{a-b}{2} & c \\ c & -\frac{a-b}{2} \end{bmatrix} \quad . \tag{1.53}$$

The second term of Equation (1.53) is real and symmetric and can thus be diagonalized. In other words, we can define a new frame of reference (by rotation) in which this second term is diagonal, and because the trace is preserved, the sum of the two diagonal terms must be zero. Accordingly, in this new frame of reference, the strain tensor can be written:

$$\underline{\underline{\epsilon}} = \frac{\epsilon_{\mathrm{dil}}}{2} \cdot \begin{bmatrix} 1 & 0 \\ 0 & 1 \end{bmatrix} + \frac{\epsilon_{\mathrm{shear}}}{2} \cdot \begin{bmatrix} 1 & 0 \\ 0 & -1 \end{bmatrix} \quad . \tag{1.54}$$

where $\epsilon_{\mathrm{dil}} = a + b$ and $\epsilon_{\mathrm{shear}} = 2\sqrt{c^2 + \left(\frac{a-b}{2}\right)^2}$.

1.2.4.c Model 2: liquid interfaces with surfactants

As presented in Section 1.2.3, in this model the interfacial tension shows no deviatoric component ($\underline{\underline{T}}_{\text{viscous}} \equiv 0$ and $\underline{\underline{T}}_{\text{elastic}} \equiv 0$). In the presence of adsorbed compounds, (surfactant or polymers) the isotropic tension depends on the surface excess and can thus decrease during compression. In this case, the interfacial stress is:

$$\underline{\underline{T}}_{\text{surface}} = \underline{\underline{T}}_{\text{pure}} + \underline{\underline{T}}_{\Gamma} = (\gamma_0 - \Pi(\Gamma)) \cdot \underline{\underline{\mathbb{1}}} = \gamma \cdot \underline{\underline{\mathbb{1}}} \ , \tag{1.55}$$

where γ is the total interfacial tension, γ_0 the interfacial tension corresponding to the $\underline{\underline{T}}_{\text{pure}}$ component and Π the surface pressure. Interfacial tension and strain tensors are scalars.

One can measure $\underline{\underline{T}}_{\Gamma}$ using various methods:

- the isotherm compression shows surface pressure Π versus the area per molecule a, for extremely slow compressions, i.e. quasi-static measurement (an example is given in Figure 1.13a). This method is mostly used with insoluble surfactants in Langmuir-trough where it is possible to know the number of molecules at the interface.
- the liquid dilational modulus can be obtained by oscillating a drop interface and recording γ as a function of the area A.

We define the liquid dilational modulus by:

$$E_\gamma = \frac{\partial \gamma}{\partial \ln(A)} = -\frac{\partial \Pi}{\partial \ln(A)} \ . \tag{1.56}$$

When the strain $\epsilon_{\text{dil}}(t)$ is sinusoidal with respect to time t, it is written

$$\epsilon_{\text{dil}}(t) = \epsilon_0 \cos(\omega t) \ , \tag{1.57}$$

where ϵ_0 is the amplitude and ω the angular frequency ($A = A_0(1 + \epsilon_0 \cos(\omega t))$). In complex notations (where $j^2 = -1$), the strain ϵ_{dil} is the real part of the complex strain ϵ^*_{dil}:

$$\epsilon^*_{\text{dil}}(t) = \epsilon_0 \cdot \mathrm{e}^{j\omega t} \ . \tag{1.58}$$

The complex strain-rate is then proportional to the strain, with an imaginary factor $j\,\omega$ (which implies a phase shift of $\frac{\pi}{2}$):

$$\dot{\epsilon}^*_{\text{dil}}(t) = j\omega\, \epsilon_0 \mathrm{e}^{j\omega t} = j\omega \cdot \epsilon^*(t) \ . \tag{1.59}$$

In the linear regime, i.e. for small strain (below 1%), the measured variation of stress is also sinusoidal and has the same frequency ω:

$$T^*_{\text{surface}} = T_{\text{surface},0} + T^*_{\text{surface},1}\, \mathrm{e}^{j\omega t} \ , \tag{1.60}$$

where $T_{\text{surface},0}$ is the mean value of T^*_{surface} and $T^*_{\text{surface},1}$ its complex amplitude.

In this regime, $T^*_{\mathrm{surface},1}$ is proportional to ϵ_0, and E^*_γ is the proportionality factor, called the *complex liquid modulus.*

$$E^*_\gamma = \frac{T^*_{\mathrm{s},1}}{\epsilon_0} = E'_\gamma + j\, E''_\gamma \ . \tag{1.61}$$

The real and imaginary parts of the complex liquid modulus are respectively:

- E'_γ, representing the in-phase response,
- E''_γ, representing the out-of-phase response.

A model of liquid dilational modulus E^*_γ was described by Lucassen *et al.* [38] in the case of an oscillatory deformation. In this model, the dilational modulus results from the diffusion of the surfactants between the bulk and the interface:

$$E^*_\gamma = E_0 \frac{1+\zeta+i\,\zeta}{1+2\zeta+2\zeta^2} \ , \tag{1.62}$$

with

$$\begin{cases} E_0 = -\dfrac{\mathrm{d}\,\gamma}{\mathrm{d}\ \ln(\Gamma)} \ , & (1.63\mathrm{a}) \\ \zeta = \dfrac{\mathrm{d}\,C_0}{\mathrm{d}\,\Gamma}\sqrt{\dfrac{D}{2\omega}} \ , & (1.63\mathrm{b}) \end{cases}$$

where D is the diffusion constant of the surfactant molecules, C_0 their bulk concentration, and ω the angular frequency of the deformation. E_0 is called the Gibbs modulus.

We observe two asymptotic behaviours in Equation (1.62).

- At low frequency (i.e. when $\zeta \gg 1$), diffusion occurs faster than the imposed deformation. The interface is thus always at equilibrium with the bulk and the interfacial tension is constant ($T^*_{\mathrm{surface},1} = 0$ and $T^*_{\mathrm{surface}} = T_{\mathrm{surface},0}$): $E^*_\gamma \to 0$.
- At high frequency (i.e. when $\zeta \ll 1$), diffusion is slower than the imposed deformation. The interface therefore acts as if there were no desorption ($\Gamma A = C^{ste}$): $E^*_\gamma \simeq E_0$.

1.2.4.d Model 3: capillarity and elasticity

In this model, the interfacial stress is:

$$\underline{\underline{T}}_{\mathrm{surface}} = \gamma_0 \cdot \underline{\underline{\mathbb{1}}} + \underline{\underline{T}}_{\mathrm{elastic}} \ . \tag{1.64}$$

The response of an elastic interface can be described by a Hookean model at small deformations [39, 40]. Other models exist (Mooney-Rivlin, Skalak, etc) but they are not described here .

Given a frame of reference defined by two orthogonal directions x and y in which the strain tensor is written

$$\underline{\underline{\epsilon}} = \begin{bmatrix} \epsilon_{\mathrm{x}} & 0 \\ 0 & \epsilon_{\mathrm{y}} \end{bmatrix} \ , \tag{1.65}$$

in the Hookean model the elastic stress tensor is:

$$\underline{\underline{T}}_{\mathrm{elastic}} = \begin{bmatrix} T_{\mathrm{x}} & 0 \\ 0 & T_{\mathrm{y}} \end{bmatrix} \quad , \tag{1.66}$$

where

$$\begin{cases} T_{\mathrm{x}} = \dfrac{Y_{\mathrm{s}}}{1-\nu_{\mathrm{s}}^2} \cdot \dfrac{1}{1+\epsilon_{\mathrm{y}}} \cdot (\epsilon_{\mathrm{x}} + \nu_{\mathrm{s}}\epsilon_{\mathrm{y}}) \quad , & (1.67\mathrm{a}) \\[2ex] T_{\mathrm{y}} = \dfrac{Y_{\mathrm{s}}}{1-\nu_{\mathrm{s}}^2} \cdot \dfrac{1}{1+\epsilon_{\mathrm{x}}} \cdot (\epsilon_{\mathrm{y}} + \nu_{\mathrm{s}}\epsilon_{\mathrm{x}}) \quad , & (1.67\mathrm{b}) \end{cases}$$

where Y_{s} is the surface Young modulus and $\nu_{\mathrm{s}} \in [-1;1]$ is the surface Poisson ratio.

In the specific case of pure compression/dilatation ($\epsilon_{\mathrm{x}} = \epsilon_{\mathrm{y}} = \epsilon$), Equation (1.67) yields:

$$T_{\mathrm{x}} = T_{\mathrm{y}} = \frac{Y_{\mathrm{s}}}{1-\nu_{\mathrm{s}}} \cdot \frac{\epsilon}{1+\epsilon} \quad . \tag{1.68}$$

In the specific case of pure shear deformation ($\epsilon_{\mathrm{x}} = -\epsilon_{\mathrm{y}} = \epsilon$), Equation (1.67) yields:

$$T_{\mathrm{x}} = -T_{\mathrm{y}} = \frac{Y_{\mathrm{s}}}{1+\nu_{\mathrm{s}}} \cdot \frac{\epsilon}{1+\epsilon} \quad . \tag{1.69}$$

Going back to the general deformation involving both compression/dilatation and shear deformation, we can introduce the elastic dilational modulus K and the elastic shear modulus G presented by Pozrikidis [31] and Barthes-Biesel *et al.* [41] in the Hookean frame at small deformation:

$$\begin{cases} G = \dfrac{1}{2} \cdot \dfrac{Y_{\mathrm{s}}}{1+\nu_{\mathrm{s}}} \quad , & (1.70\mathrm{a}) \\[2ex] K = \dfrac{1}{2} \cdot \dfrac{Y_{\mathrm{s}}}{1-\nu_{\mathrm{s}}} \quad . & (1.70\mathrm{b}) \end{cases}$$

According to Equation (1.70), Equation (1.67) becomes:

$$\begin{cases} T_{\mathrm{x}} = \dfrac{1}{1+\epsilon_{\mathrm{y}}} \cdot \left[K \cdot (\epsilon_{\mathrm{x}} + \epsilon_{\mathrm{y}}) + G \cdot (\epsilon_{\mathrm{x}} - \epsilon_{\mathrm{y}})\right] \quad , & (1.71\mathrm{a}) \\[2ex] T_{\mathrm{y}} = \dfrac{1}{1+\epsilon_{\mathrm{x}}} \cdot \left[K \cdot (\epsilon_{\mathrm{y}} + \epsilon_{\mathrm{x}}) + G \cdot (\epsilon_{\mathrm{y}} - \epsilon_{\mathrm{x}})\right] \quad . & (1.71\mathrm{b}) \end{cases}$$

In Equation (1.71), at small deformations, we neglect the prefactor, and thus the dilational term (proportional to K) is the same for T_{x} and T_{y}. Moreover, for small deformations, the area change is:

$$\frac{\Delta A}{A} = \epsilon_{\mathrm{x}} + \epsilon_{\mathrm{y}} \quad . \tag{1.72}$$

K is thus defined similarly as E_γ in pure dilatation by:

$$K = \frac{\mathrm{d}\, T_{\mathrm{elastic}}}{\mathrm{d}\, \ln A} \quad . \tag{1.73}$$

Addition of the osmotic component. The variation of the osmotic component $\underline{\underline{T}}_{\Gamma}$ depends only on area variation and not on shear strain, and is described by the liquid dilation modulus E_{γ} introduced above. When there are elasticity and osmotic pressure, the total interfacial stress is:

$$\underline{\underline{T}}_{\text{surface}} = \underline{\underline{T}}_{\text{pure}} + \underline{\underline{T}}_{\Gamma} + \underline{\underline{T}}_{\text{elastic}} \quad . \tag{1.74}$$

Because of the similarity between Equations (1.56) and (1.73), it is difficult to dissociate the two contributions of $\underline{\underline{T}}_{\Gamma}$ and $\underline{\underline{T}}_{\text{elastic}}$ of Equation (1.74) in the response to dilatation. For this reason, $\underline{\underline{T}}_{\Gamma}$ is usually considered as constant [42, 43] and all the variations are taken into account in $\underline{\underline{T}}_{\text{elastic}}$, with an effective dilational modulus:

$$E = K + E_{\gamma} \quad . \tag{1.75}$$

An example of this phenomenological approach to characterize interfacial properties is the model of Marmottant *et al.* [44].

1.2.4.e Model 4: capillarity, elasticity and viscosity

In this model, viscoelastic interfaces are described by Equation (1.38). The viscoelastic response of an interface ($\underline{\underline{T}}_{\text{elastic}} + \underline{\underline{T}}_{\text{viscous}}$) is usually described by the association of a spring for the elastic response, and a damper for the viscous response. Depending on the rheological model, the two elements can be associated in parallel (Kelvin-Voigt model, Figure 1.17a) or in series (Maxwell model, Figure 1.17b).

(a) Kelvin-Voigt model.

(b) Maxwell model.

Figure 1.17: The two simplest models of viscoelastic materials, with an elastic response (spring) and a viscous response (damper).

According to the complex formalism presented in Section 1.2.4.c, we define the complex elastic shear modulus $G^{*} = G' + j \cdot G''$ and the complex elastic dilational modulus $K^{*} = K' + j \cdot K''$.

The real and the imaginary parts of the complex elastic moduli are respectively:

- the *storage moduli*, representing the elastic in-phase responses,
- the *loss moduli*, representing the viscous out-of-phase responses.

We define the dilational and shear interfacial viscosities $\eta_{\text{k,s}}$ and $\eta_{\text{g,s}}$ as

$$\eta_{\text{k,s}} = \frac{1}{\omega} \cdot K'' \quad , \tag{1.76}$$

and

$$\eta_{\text{g,s}} = \frac{1}{\omega} \cdot G'' \quad . \tag{1.77}$$

As we have seen previously in the case of the elastic interfaces of the model 3, we consider that $\underline{\underline{T}}_{\Gamma}$ is constant upon deformation, and the variations are included in the deviatoric terms $\underline{\underline{T}}_{\text{elastic}}$ and $\underline{\underline{T}}_{\text{viscous}}$. In this case, the effective complex dilational modulus is:

$$E^* = E^*_{\gamma} + K^* \quad . \tag{1.78}$$

Petkov *et al.* [45] present a model of viscoelastic interfaces following the Kelvin-Voigt model where the elastic response is described by a Hookean model suggested by Landau and Lifshits [46]:

$$\begin{cases} \underline{\underline{T}}_{\text{elastic}} = (K' - G') \cdot \operatorname{tr} \underline{\underline{\epsilon}} \cdot \underline{\underline{\mathbb{1}}} + 2\, G' \cdot \underline{\underline{\epsilon}} \quad , & (1.79\text{a}) \\[2ex] \underline{\underline{T}}_{\text{viscous}} = (\eta_{\text{k,s}} - \eta_{\text{g,s}}) \cdot \operatorname{tr} \underline{\underline{d}} \cdot \underline{\underline{\mathbb{1}}} + 2\, \eta_{\text{g,s}} \cdot \underline{\underline{d}} \quad , & (1.79\text{b}) \end{cases}$$

where $\operatorname{tr} \underline{\underline{\epsilon}}$ is the trace of the tensor $\underline{\underline{\epsilon}}$.

In oscillatory deformation, we replace the strain tensor $\underline{\underline{\epsilon}}$ by $\underline{\underline{\epsilon}}^*$ and the strain-rate tensor $\underline{\underline{d}}$ by $\underline{\underline{d}}^* = j\omega \cdot \underline{\underline{\epsilon}}^*$. Moreover we define $\underline{\underline{T}}^*_{\text{viscoelastic}} = \underline{\underline{T}}^*_{\text{elastic}} + \underline{\underline{T}}^*_{\text{viscous}}$ and consequently, Equation (1.79) becomes:

$$\underline{\underline{T}}^*_{\text{viscoelastic}} = (K^* - G^*) \cdot \operatorname{tr} \underline{\underline{\epsilon}}^* \cdot \underline{\underline{\mathbb{1}}} + 2\, G^* \cdot \underline{\underline{\epsilon}}^* \quad . \tag{1.80}$$

1.2.4.f Examples of experimental set-ups for interfacial rheological measurements

Shear deformation. We present here the "double-wall ring" (DWR) geometry developed by TA Instruments with Vandrebril *et al.* [47], and illustrated in Figure 1.18. The two phases are poured into a trough delimited by two concentric walls, and a ring as the one shown in Figure 1.18a is placed at the interface. The ring is connected to a motor, which transfers a torque to it and one measures the angular displacement, as illustrated in Figure 1.18b. This setup has been used in the present thesis to characterize the interfacial shear properties of multilayers and will be detailed in Section 2.1.

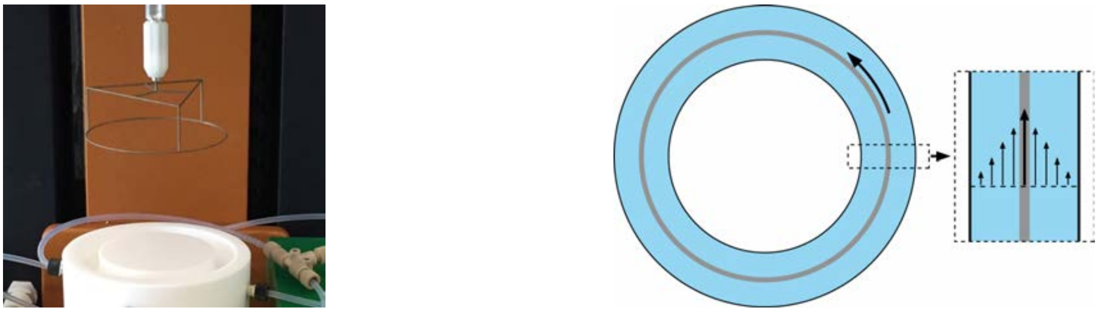

(a) Interfacial rheometer with "Double-wall ring" geometry. Ring and rheometer are provided by TA Instruments.

(b) Top view of the interface sheared by the rotation of the ring (grey). A torque (stress) is applied and the rotation (deformation) is measured.

Figure 1.18: Interfacial rheometer, picture and principle.

Compression/dilatation. The Langmuir-trough and pendant-drop apparati allow compression or dilatation of an interface and the measurement of interfacial tension as a function of area . A Langmuir-trough is a rectangular container in which the liquid offers a planar interface which can be compressed with a barrier, as illlustrated in Figure 1.12b. The pendant-drop apparatus consists in a droplet (or a bubble) whose interface is dilated or compressed when the volume is increased or decreased.

In these two methods the deformation is not isotropic, which can be problematic for viscoelastic interfaces, as shear viscosity and modulus may contribute to the measured signal.

An isotropic compression/dilatation is difficult to obtain experimentally, as shown by Cicuta *et al.* [48]. Such a deformation can be reached using a radial trough, as used in Vermant's group. In their experiment, the interface is deformed using twelve moving arms pulling on a rubber band held at the interface, and the interfacial tension is measured using a Wilhelmy plate in the middle of the deformed interface, as illustrated in Figure 1.19. This method has been used in the present thesis to characterize the polymer bilayers, and will be detailed in Section 2.1.

Figure 1.19: Radial trough apparatus. The trough (in white) contains a liquid, and a rubber band is held on the air/liquid interface to delimit and deform a portion of the interface. The shape of the rubber band is controlled by the twelve arms. The Wilhelmy plate is not shown on the picture. (Picture by M. Pepicelli).

Compression/dilatation of membranes is the appropriate geometry to investigate surface excess effects, and possible adsorption/desorption processes.

1.2.4.g Link between 3D and 2D moduli

Considering a thin membrane of homogeneous and isotropic material with air on both sides as presented in Figure 1.20, we can measure the force applied to stretch the membrane along the x direction. For the sake of simplicity, we also consider in this example that there is no Poisson effect (i.e., traction along the x direction does not implies lateral compression along y or z directions): $\nu_{3D} = 0$. The traction force f exerted on the membrane is the integral of the internal stress σ over the width (along the y direction) and the thickness (along the z direction) of the membrane, respectively W and h:

$$f = \iint_{W,h} \sigma \, \mathrm{d}y \mathrm{d}z \quad . \tag{1.81}$$

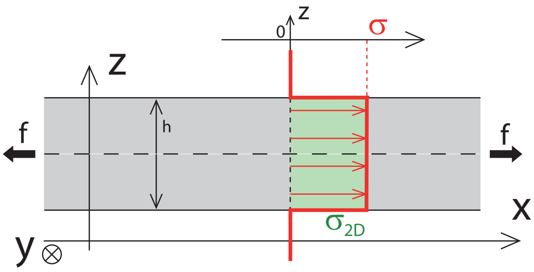

Figure 1.20: Geometry of the homogeneous thin membrane stretched in one direction.

The membrane being thin, it is convenient to get rid of the thickness parameter h, which is typically smaller than the other length scales by several orders of magnitude. We thus write:

$$f = \int_W \left(\int_h \sigma \, \mathrm{d}z \right) \cdot \mathrm{d}y \quad . \tag{1.82}$$

A 2D stress σ_{2D} naturally appears:

$$\sigma_{\mathrm{2D}} = \int_h \sigma \, \mathrm{d}z \quad . \tag{1.83}$$

The force is thus:

$$f = \int_W \sigma_{\mathrm{2D}} \cdot \mathrm{d}y \quad . \tag{1.84}$$

Because of the large aspect ratios of membranes, their properties and behaviours are better described by their 2D parameters, which are indeed easier to measure. More generally, interfacial stresses are the integration of bulk stresses over the thickness of the interface, and the interfacial moduli describe the link between these stresses and 2D deformation.

As we define the 3D Young modulus Y_{3D} with the deformation ϵ

$$Y_{\mathrm{3D}} = \frac{\sigma}{\epsilon} \quad , \tag{1.85}$$

we define the 2D Young modulus Y_{2D} as the ratio between σ_{2D} and ϵ:

$$Y_{\mathrm{2D}} = \frac{\sigma_{\mathrm{2D}}}{\epsilon} \quad . \tag{1.86}$$

Combination of Equations (1.83), (1.85) and (1.86) leads to:

$$Y_{\mathrm{2D}} = \int_h Y_{\mathrm{3D}} \, \mathrm{d}z \quad . \tag{1.87}$$

For an homogeneous and isotropic material with a Poisson ratio $\nu_{\mathrm{3D}} = 0$, Equation (1.87) becomes:

$$Y_{\mathrm{2D}} = h \cdot Y_{\mathrm{3D}} \quad . \tag{1.88}$$

If there is a non-zero 3D Poisson ratio, as explained by Quilliet *et al.* [49] for homogeneous and isotropic free-standing materials, the link between 3D and 2D moduli is:

$$\begin{cases} G'_{\mathrm{2D}} = \dfrac{Y_{\mathrm{3D}}h}{2(1+\nu_{\mathrm{3D}})} = G'_{\mathrm{3D}}h \ , & (1.89\mathrm{a}) \\[2ex] K'_{\mathrm{2D}} = \dfrac{Y_{\mathrm{3D}}h}{2(1-\nu_{\mathrm{3D}})} = K'_{\mathrm{3D}}h \cdot \dfrac{3(1-2\cdot\nu_{\mathrm{3D}})}{2(1-\nu_{\mathrm{3D}})} \ . & (1.89\mathrm{b}) \end{cases}$$

The measurement of interfacial modulus G'_{2D} and thickness h allows the calculation of bulk modulus G'_{3D}, through Equation (1.89).

We would like here to emphasize that in the case of anisotropic materials, like multilayers of polymers, the calculated 3D shear modulus is not relevant: it is impossible to define a multilayer as an isotropic 3D material as a multilayer is intrinsically non-isotropic.

Moreover, in the case of a material at an interface between two fluids, the effects of the term $\underline{\underline{T}}_{\Gamma}(\Gamma)$ of Equation (1.74) are not taken into account in Equation (1.89). According to Equation (1.40) the term $\underline{\underline{T}}_{\Gamma}(\Gamma)$ shows no shear contribution, but a dilational one. Accordingly, we usually don't know the contribution of K'_{2D} in the effective dilational modulus, and consequently Equation (1.89) can not be used to evaluate K'_{3D} via K'_{2D}.

Nevertheless, Equation (1.89) offers a good estimate to compare the values of interfacial shear moduli to the known values of their bulk counterparts.

1.2.5 Deformation of droplets under a viscous stress

Previously presented measurements are performed on model geometries: flat interfaces for the radial trough and the double-wall ring, and millimeter-sized droplets for the pendant-drop experiment. However it is possible to measure rheological properties in-situ on real objects, i.e. micrometer-sized droplets or capsules. Rheological measurements typically consist either in applying a deformation and measuring the stress, or in applying a stress and measuring the associated deformation. We want here to apply a viscous stress and record the deformation.

1.2.5.a Fluid mechanics at the micrometer scale

Laminar flows and Reynolds number. In microfluidics, the fine control of flow is possible because the flows are laminar. The laminar character of the flow is indicated by the *Reynolds*' dimensionless number. Reynolds number is defined as the ratio of inertia over viscous effects. This number depends on the typical length scale of the experiment L, the dynamical viscosity η and the density of the continuous phase ρ, and the typical flow speed v:

$$\mathcal{R}e = \frac{\rho v L}{\eta} \ . \tag{1.90}$$

A high Reynolds number indicates the predominance of inertial effects, which might further lead to the turbulent regime, while a low Reynolds number indicates the predominance of viscous stresses, which is characteristic of the laminar regime. We usually distinguish two regimes:

- the laminar regime, for $\mathcal{R}e \ll 1$ (illustrated in Figure 1.21a).

(a) Laminar regime

(b) Turbulent regime

Figure 1.21: The different regimes of flow, for low and high Reynolds numbers. The fluids is moving from left to right and meet an inclined plate. Pictures from Van Dyke [50]

- the turbulent regime for $\mathcal{R}e \gg 1000$ (illustrated in Figure 1.21b).

As we can see on Equation (1.21), the Reynolds number is proportional to the length scale of the experiment L. Thus, flows near small settings are more likely to be laminar. As a consequence, almost only the laminar regime ($\mathrm{R}e \ll 1$) can be observed in microfluidic experiments.

From the general Navier-Stokes equation to the Stokes equation. For incompressible flows, the Navier-Stokes equation links the velocity of the fluid $\underline{u}$, the dynamical viscosity η, the density ρ, and the pressure p, in an external force field $\underline{f}_{\text{ext}}$ through:

$$\rho\,\frac{\partial \underline{u}}{\partial t} + \rho\,(\underline{u}\cdot \underline{\underline{\mathrm{grad}}})\underline{u} - \eta\nabla^2\,\underline{u} = -\underline{\mathrm{grad}}\,p + \underline{f}_{\text{ext}} \quad . \tag{1.91}$$

The operator ∇^2 is the *Laplacian* operator. In the steady-state regime, the first term of equation (1.91) is zero, and in the laminar regime ($\mathcal{R}_\mathrm{e} \ll 1$) $\rho\,(\underline{u}\cdot\nabla)\underline{u}$ is negligible with respect to $\eta\nabla^2\,\underline{u}$. As a consequence, when $\underline{f}_{\text{ext}} = 0$ the Navier-Stokes equation (1.91) becomes the Stokes equation, which is linear with respect to the velocity $\underline{u}$:

$$\eta\nabla^2\,\underline{u} = \underline{\mathrm{grad}}\,p \quad . \tag{1.92}$$

The Stokes equation (1.92) is completed by the continuity equation, that states for incompressible flows:

$$\mathrm{div}\,\underline{u} = 0 \quad . \tag{1.93}$$

In the specific case of straight channels, we can consider that the velocity is always oriented in the direction of the channel, for instance $\underline{u} = u_x\,\vec{x}$. In these conditions, we can easily write, using equations (1.92) and (1.93), that the pressure gradient is proportional to the amplitude of the velocity field. This leads to a proportionality between the pressure difference ΔP between two points in the channel and the flow rate Q_v. Introducing the hydrodynamic resistance R_{hydro}, which is proportional to viscosity and depends on the channel geometry:

$$\Delta P = R_{\text{hydro}}\cdot Q_v \quad . \tag{1.94}$$

This equation is analogous to Ohm's law which relates the difference of electric potential ΔV and the current I through R_{elec}, the electric resistance: $\Delta V = R_{\text{elec}} \cdot I$. Indeed, microfluidic circuits can often be seen as electronic devices, where different elements are connected to build a whole set-up that manages complex operations, as DNA sequencing [51], blood-cell diagnosis [52], or interfacial tension measurements, as presented in 1.2.5.c.

1.2.5.b Viscous stress on interfaces

The stress $\underline{\underline{\sigma}}$ inside the fluid depends on the pressure and on the velocity gradient:

$$\underline{\underline{\sigma}} = -p\,\underline{\underline{\mathbb{1}}} + \eta \cdot \left(\underline{\underline{\text{grad}}}\,\underline{u} + (\underline{\underline{\text{grad}}}\,\underline{u})^{\top}\right) \quad , \tag{1.95}$$

where p is the pressure, η the viscosity of the fluid, and $\underline{u}$ is the velocity of the fluid.

Consequently, an element of interface immersed in the fluid is submitted to a force:

$$\delta\underline{F} = \underline{\underline{\sigma}} \cdot (\mathrm{d}S\,\underline{n}) = -p\,\mathrm{d}S\,\underline{n} + \eta \cdot \left(\underline{\underline{\text{grad}}}\,\underline{u} + (\underline{\underline{\text{grad}}}\,\underline{u})^{\top}\right) \cdot (\mathrm{d}S\,\underline{n}) \quad , \tag{1.96}$$

where $\underline{n}$ is a unit vector orthogonal to the interface pointing toward the fluid, and $\mathrm{d}S$ is the area of the interface element. We can distinguish two contributions in Equation (1.96): the one due to the pressure, and the one due to the viscosity.

In the geometry presented in Figure 1.22 (simple shear), the velocity is oriented along the x-axis and depends only on the y-coordinate: $\underline{u} = u_{\text{x}}(y) \cdot \underline{e}_{\text{x}}$. The viscous force on the surface S is:

$$\underline{f}_{\eta} = S \cdot \eta \cdot \frac{\partial\, u_{\text{x}}}{\partial\, y}(y=0) \cdot \mathrm{e}_{\text{x}} \quad . \tag{1.97}$$

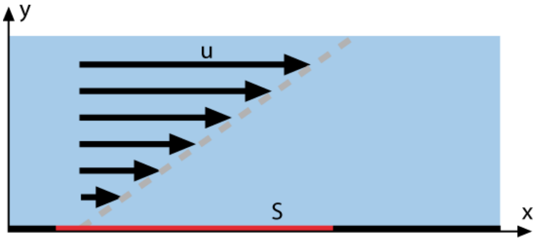

Figure 1.22: Simple shear geometry: the interface is flat, and the velocity is defined by: $\underline{u} = u_{\text{x}}(y) \cdot \underline{e}_{\text{x}}$.

Considering the pressure contribution, we can write the global stress on the interface (force per unit area) with the pressure p:

$$\underline{\underline{\sigma}}\,\underline{n} = -p(x, y=0) \cdot \underline{e}_{\text{y}} + \eta \cdot \frac{\partial\, u_{\text{x}}}{\partial\, y} \cdot \underline{e}_{\text{x}} \quad . \tag{1.98}$$

Equation (1.98) shows that the stress increases when:

- the viscosity of the surrounding fluid increases,
- the flow profile has strong variations on short length scales.

1.2.5.c Experimental deformation of droplets and capsules

The first quantitative experiments of droplet deformation were performed by Taylor [53]. Using the *Four-roller apparatus* described in Figure 1.23a, he set up a divergent flow: the fluid arrives from the top and the bottom parts, and leaves on the right and on the left. The flow consequently pulls on both sides of the droplets to elongate it, as illustrated in Figure 1.23b. The steady shape results from a balance of the driving viscous stresses and the restoring interfacial tension:

- at rest, the droplet is spherical because of interfacial tension,
- under moderate shear rates, the droplet is deformed according to a balance between shear stresses and interfacial tension,
- under high shear stress, there is no possible balance, and the droplet breaks up.

Consequently, for moderate shear stress, the knowledge of the stress at the interface, and the recording of the deformation, lead to a measurement of the interfacial tension.

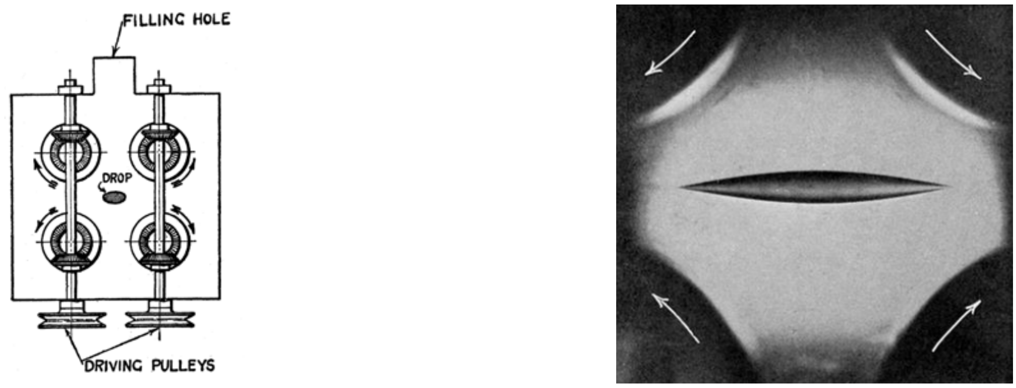

(a) The four counter-rotating wheels set a fully symmetric flow with a controlled shear rate and a stagnation point in the center.

(b) Deformation of a droplet in the set up.

Figure 1.23: The *Four-roller* apparatus of Taylor (Sketch and picture from [53]).

Lee *et al.* [54] and Deschamps *et al.* [55] miniaturized Taylor experiment in a microfluidic chip to measure interfacial properties of droplets and vesicles. In order to have more systematic measurements, Hudson *et al.* integrated this device into a microfluidic chip [56, 57] by using a convergent and then divergent channel. The convergent/divergent channel creates a gradient of velocity in the main direction of the flow, plus a converging flow, as shown in Figure 1.24a. Microfluidics allows to perform measurements on a large number of droplets, and hence enables a statistical treatment of the data which enhances the accuracy of the results.

This setup has been further adapted by Brosseau *et al.* in Baret's group [58] in order to deform capsules, which requires stronger stresses. They transformed the convergent and divergent channels into sharp steps between narrow channels where the capsules are confined and large chambers where the capsules are only interacting with the viscous flow, as shown in Figure 1.24b.

To relate the measured deformation to interfacial tension, Taylor developed a theoretical model [53], which was generalized by Barthes-Biesel *et al.* [59, 60], and summarized by Rallison [61]. This model was also used by Hudson *et al.* to extract the interfacial tension from the deformation measurements.

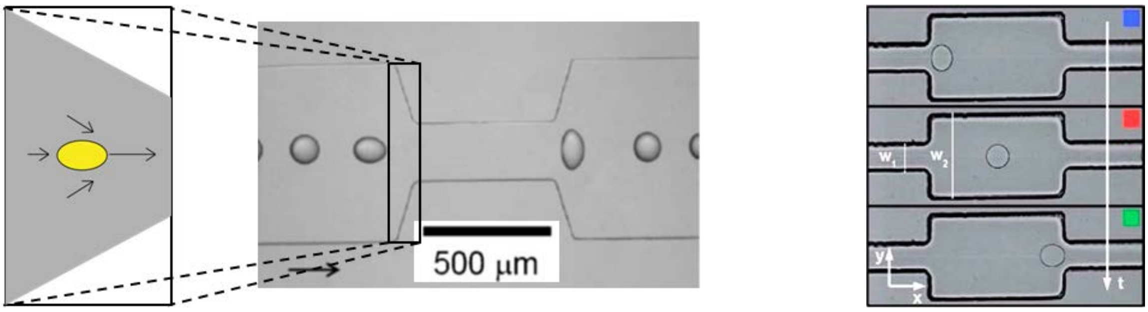

(a) Convergent and divergent channel used by Hudson *et al.* [56, 57] to shear and deform the droplets. Recording the deformation allows a measurement of interfacial tension.

(b) Step channel used by Brosseau *et al.* [58] to deform capsules ($W_1 = 100\,\mu$m, $W_2 = 300\,\mu$m).

Figure 1.24: Microfluidic geometries used to deform (a) droplets and (b) capsules.

1.2.5.d Theoretical deformation of droplets in a defined flow profile

Steady deformation. The model of Taylor considers a droplet of viscosity η_{drop} in a fluid of viscosity η_{bulk}. The radius of the droplet at rest is r, and the interfacial tension with the surrounding fluid is γ. The surrounding fluid undergoes a hyperbolic flow in the (O, x, y) plane defined by:

$$\underline{u} = \dot{\epsilon} \cdot (x, -y, 0) \quad , \tag{1.99}$$

where the shear rate is defined as:

$$\dot{\epsilon} = \frac{\partial u_{\text{x}}}{\partial x} \quad . \tag{1.100}$$

Moreover, Equation (1.93) is verified, and the shear rate does not depend on the position.

Taylor defines the viscosity contrast λ and the capillary number $\mathcal{C}a$ as follows:

$$\lambda = \frac{\eta_{\text{drop}}}{\eta_{\text{bulk}}} \quad , \tag{1.101}$$

$$\mathcal{C}a = \frac{\eta_{\text{bulk}}\, \dot{\epsilon}\, r}{\gamma} \quad . \tag{1.102}$$

Furthermore, he defines the droplet deformation as a dimensionless number calculated with the x-axis width a and the y-axis height b of the droplet:

$$D = \frac{b - a}{b + a} \quad . \tag{1.103}$$

Under these conditions, the steady deformation is [53]:

$$D_{\text{steady}} = 2 \cdot \frac{19\lambda + 16}{16\lambda + 16} \cdot \mathcal{C}a \quad . \tag{1.104}$$

When the flow is less regular than the hyperbolic flow described by Taylor, Barthes-Biesel *et al.* [59] state that Equation (1.104) must be defined with the eigenvalues e_{max} and e_{min} of the deformation tensor defined by Equation (1.45):

$$D_{\text{steady}} = \frac{19\lambda + 16}{16\lambda + 16} \cdot \frac{\eta_{\text{bulk}}\, r}{\gamma} \cdot (e_{\text{max}} - e_{\text{min}}) \quad . \tag{1.105}$$

Transient regime. Barthes-Biesel *et al.* [59] also describe the transient regime as a first order relaxation towards the steady state previously described by Equation (1.105). The derivative of the deformation D with respect to time t depends on the steady deformation D_{steady} and the actual deformation:

$$\frac{\mathrm{d}\,D}{\mathrm{d}\,t} = \frac{1}{\tau_{\text{ca}}} \cdot (D_{\text{steady}} - D) \quad , \tag{1.106}$$

with a relaxation time τ_{Ca} defined as follows:

$$\tau_{\text{ca}} = \frac{2}{5} \cdot (2\lambda + 3) \cdot \frac{19\lambda + 16}{16\lambda + 16} \cdot \frac{\eta_{\text{bulk}}\, r}{\gamma} \quad . \tag{1.107}$$

This relaxation time depends on the interfacial tension γ. Therefore the fitting of such relaxation toward the steady state provides a way to measure γ. This will be used and developed in more details in Chapter 3.

We have presented the interfacial tension, and more generally the interfacial rheology. We have seen the formalism that we will need in the next chapters, and we have introduced a few measurement setups that are used in this thesis. In this work we use polymers to tune these interfacial properties. We need therefore to present the basis of the polymer physics and more specifically the theoretical description of polymer at interfaces.

To summarize this section:

As soon as two immiscible fluids are in contact, there is an interface associated with an energy cost. This energy implies a force exerted on every system containing a part of the interface: this is the interfacial tension. Surfactant molecules tend to adsorb at interfaces and to decrease their interfacial tension. When an interface contains bigger molecules or objects, it can exhibit more complex behaviours, from viscosity to elasticity.

Interfacial rheology consists in relating stress and deformation of the interface through the elastic and viscous moduli, which can be measured in compression/dilatation, or in shear deformation.

Moreover, it is possible to use microfluidics to deform droplets and capsules with a known stress. The deformation is thus a measurement of interfacial tension.

1.3 Polymers at interfaces

One way to tune the interface rheological properties and to observe viscosity or elasticity as presented in Table 1.1 is to have polymers at the interface. We first present basic notions related to polymers in solution, the static structure of a layer of polymer, and how it affects interfacial tension. Then we detail the adsorption kinetics of various systems of polymers, and the interfacial rheology of polymer monolayers and multilayers.

1.3.1 Polymer in solution

We present here the conformation of the polymer chains in solution. This conformation depends on the interaction between the units and with the solvent.

1.3.1.a Random walk

We consider linear polymer chains of N units ($N \gg 1$) with b the size of these units. For an ideal polymer chain the configuration of the repeated units describes the trajectory of a random walk. The end-to-end distance of the chain $R_{\mathrm{end-end}}$ depends on the size of the units, b, and of the number of units, N, as detailed by Rubinstein and Colby [62]:

$$\langle R^2_{\mathrm{end-end}} \rangle = N \cdot b^2 \quad . \tag{1.108}$$

The radius of the chain R_Θ is defined as follows:

$$R_\Theta = \sqrt{\langle R^2_{\mathrm{end-end}} \rangle} = b \cdot N^{1/2} \quad . \tag{1.109}$$

1.3.1.b Excluded volume

There is an interaction energy between the units, which diverges when they start to overlap. In a solvent, the energy required to bring two units from an infinite distance to a distance r is called $U(r)$. There are three model cases for the shape of $U(r)$, as represented in Figure 1.25:

- first case: there is no specific interaction except a steric repulsion, for $r < b$ (orange in Figure 1.25),
- second case: there is an additional repulsion energy, which occurs for charged units, or when the units prefer to be surrounded by solvent than by themselves (red in Figure 1.25)
- third case: there is an attractive energy, for example when units prefer to be surrounded by themselves than by solvent (blue in Figure 1.25).

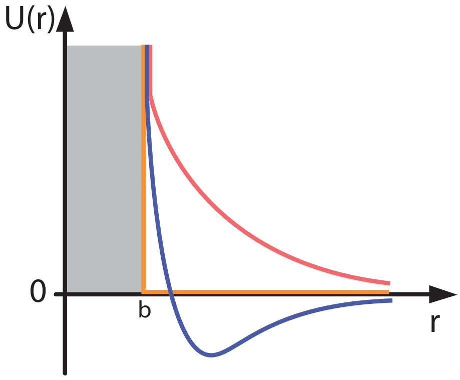

Figure 1.25: Interaction energy U between the units of a polymer chain as a function of the distance r. U tends to infinity because of steric repulsion, when the distance r between units is smaller than their size b. The orange line describes the case when there is no additional interaction, the red line when there is an additional net repulsion, and the blue line when there is an additional net attraction.

The Mayer f-function is defined as follows:

$$f(r) = \exp\left(-\frac{U(r)}{k_\mathrm{B}T}\right) - 1 \quad , \tag{1.110}$$

where T is temperature and k_B the Boltzmann constant.

The Mayer f-function represents how the density of probability to have a unit at a distance r from the origin is modified by the presence of another unit at the origin.

The *excluded volume* v is the integral on the whole space of the Mayer f-function:

$$v = -\int f(r)\mathrm{d}^3r = \int \left(1 - \exp\left(-\frac{U(r)}{k_\mathrm{B}T}\right)\right) \mathrm{d}^3r \quad . \tag{1.111}$$

Without any interaction energy ($U(r) \equiv 0$), the excluded volume is zero. The steric repulsion, and any repulsive interaction bring a positive contribution to the excluded volume, while an attractive interaction brings a negative contribution to the excluded volume, as presented in Figure 1.26.

1.3.1.c Quality of the solvent

The sign of the excluded volume determines the quality of the solvent:

- if the excluded volume is positive (e.g. red and orange cases in Figure 1.25), the chain is more expanded than if it was ideal (random walk), as illustrated in Figure 1.27a: the chain is in *good solvent*,
- if the excluded volume is negative (e.g. blue case in Figure 1.25), the chain is more collapsed than if it was ideal, as illustrated in Figure 1.27b: the chain is in *poor solvent*,
- if the excluded volume is zero, the chain describes a random walk, as illustrated in Figure 1.27c: the chain is in θ-*solvent*.

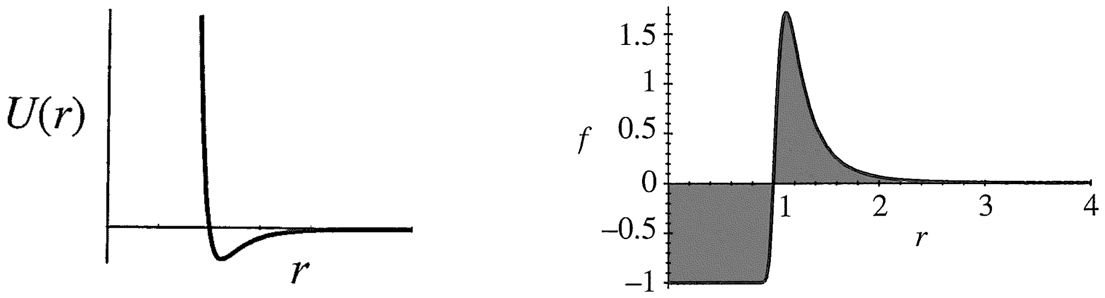

(a) Interaction energy as a function of distance. (b) Mayer f-function as a function of distance.

Figure 1.26: Mayer f-function in the case of an interaction energy presenting steric repulsion and an attractive contribution (a). The excluded volume is the opposite of the area under the curve of the Mayer f-function ((grey zone) in (b)). Here, the excluded volume presents a positive contribution due to the steric repulsion, and a negative contribution due to the attractive interaction. Figure from Colby and Rubinstein [62].

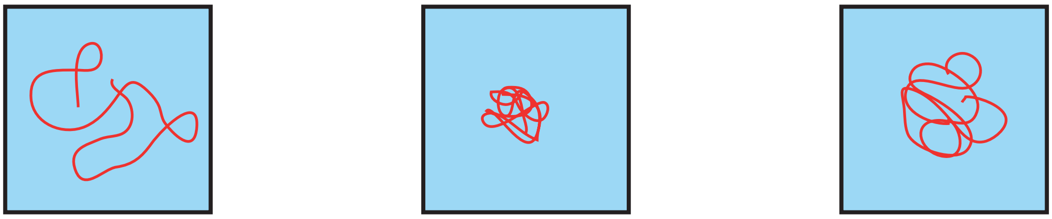

(a) Good solvent. (b) Poor solvent. (c) θ-solvent.

Figure 1.27: The size of the polymer coil defines the quality of the solvent. (a): if the chain is more expanded than a random-walk trajectory, it is in *good solvent.* (b): if the chain is more collapsed than a random walk trajectory, it is in *poor solvent.* (c): if the chain has the same volume than a random walk, it is in θ*-solvent.*

A chain in a good solvent has a larger radius than the one predicted by equation (1.109): the chains form a coil, whose radius is called the *Flory radius* R_F. The radius is no longer proportional to $N^{1/2}$, but because of the good interaction with the solvent, the chain is expanded and the radius is larger and scales as:

$$R_\mathrm{F} = b\, N^{3/5} \quad . \tag{1.112}$$

1.3.2 Adsorbed polymer layers

When a polymer chain is adsorbed at an interface, the adsorption energy of each unit is of the order of $k_B\, T$, so the overall adsorption energy of the polymer chain is of the order of $N \cdot k_B\, T$. Therefore, the adsorption of polymer molecules can be considered as irreversible.

Layers of polymers at interfaces have been studied for their ability to control the wettability of surfaces (hydrophobic or hydrophilic) [63, 64], the dispersion of colloids in solution [65], or to produce bio-compatible microparticles [66].

We first describe the case of polymers chemically grafted on a solid interface by one end, and then the case of homopolymers at a liquid interface.

1.3.2.a Layers chemically grafted on solid interface by one end

Here we consider that the polymers are chemically grafted at one end to the interface, and the chains are soluble in the surrounding solution. The best description of such layers was brought by Alexander [67] and de Gennes [68], and is known as the *Alexander-de Gennes* model. The polymer chains contain N repeated units of size b. We define the grafting density Γ_{chains} as the number of chains per unit area: $\Gamma_{\text{chains}} = \frac{1}{N} \cdot \Gamma$, where Γ is the surface excess, i.e. number of repeated unit per unit area.

The dimensionless chain grafting density $\overline{\Gamma}_{\text{chains}}$ corresponds to the number of chains grafted on an area πb^2.

$$\overline{\Gamma}_{\text{chains}} = \Gamma_{\text{chains}} \cdot \pi b^2 \quad . \tag{1.113}$$

When the grafting density $\overline{\Gamma}_{\text{chains}}$ is low, the chains are far enough from each other and do not overlap. Each chain is free and occupies a half-sphere of radius comparable to the Flory radius described by Equation (1.112): this is the *mushroom-state* pictured in Figure 1.28a. The volume fraction of polymer Φ depends on the distance from the interface z. De Gennes [68] showed that at small distance from interface:

$$\Phi = \overline{\Gamma}_{\text{chains}} \cdot \left(\frac{z}{b}\right)^{2/3} \quad . \tag{1.114}$$

The chains do not interact when they do not overlap, which means that there is less than one chain on a surface equal to πR_{F}^2:

$$\frac{\overline{\Gamma}_{\text{chains}}}{\pi b^2} \cdot \pi R_{\text{F}}^2 < 1 \quad . \tag{1.115}$$

In other words, using Equation (1.112):

$$\overline{\Gamma}_{\text{chains}} < N^{-6/5} \quad . \tag{1.116}$$

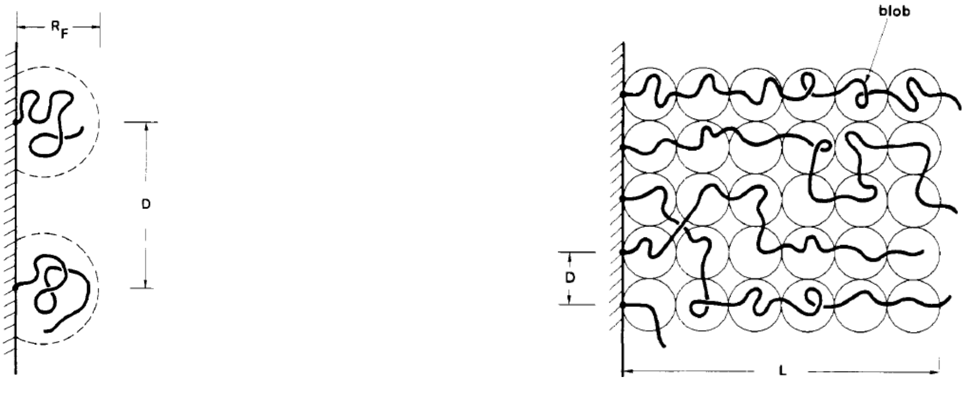

(a) The mushroom-state corresponds to low grafting density: the chains describe portions of spheres.

(b) The brush-state corresponds to high grafting density: the chains are stretched away from the wall. Circles delimit blobs of size D, which is the mean distance between two neighbouring chains.

Figure 1.28: Structure of the polymers grafted on an interface. The structure of the polymer layers highly depends on their grafting density. Figure adapted from de Gennes [68]

For higher grafting density ($\overline{\Gamma}_{\text{chains}} > N^{-6/5}$), the chains stretch in the direction orthogonal to the wall, as illustrated in Figure 1.28b. In this configuration, the chains are repelled from the interface because of excluded-volume effects: this is the *brush-state*.

It is then natural to define the length D which is the average distance between two grafting points:

$$D = b\,\overline{\Gamma}_{\text{chains}}^{-1/2} \quad . \tag{1.117}$$

The chain is divided into sections of size D called *blobs*, containing g repeated units each. We assume that in these sections the chain conformation is the same as in the bulk solution [62]. The chain is thus described as a chain of blobs of size D, represented in Figure 1.28b by the circles. The units are in good solvent, and therefore, according to Equation (1.112) the size of the blobs is:

$$D = b \cdot g^{3/5} \quad . \tag{1.118}$$

Considering that space is densely filled by the spherical blobs, the volume fraction of the brush is equivalent to the volume fraction in a blob:

$$\Phi = \frac{g \cdot b^3}{D^3} \quad . \tag{1.119}$$

Using Equations (1.117) and (1.118), Equation (1.119) implies:

$$\Phi \simeq \overline{\Gamma}_{\text{chains}}^{2/3} \quad . \tag{1.120}$$

The volume fraction can also be written:

$$\Phi = \frac{N \cdot b^3}{L \cdot D^2} \quad , \tag{1.121}$$

where L is the thickness of the brush. Combining Equations (1.117), (1.120) and (1.121), the thickness is:

$$L \simeq N \cdot b \cdot \overline{\Gamma}_{\text{chains}}^{1/3} \quad . \tag{1.122}$$

1.3.2.b Adsorbed layers of homopolymers

When the polymers are not chemically grafted but simply physically adsorbed at an interface every part of the chain has the same affinity with the interface. As described by De Gennes [69], the configuration of the interface consists in *trains* and *loops* as illustrated in Figure 1.29:

- the trains are the regions of the chains which are adsorbed and contained in the plane of the interface. The adsorption energy makes the trains energetically favorable.
- The loops are the regions of the chains which are extending in the bulk. The supplementary degree of freedom makes the loops entropically favorable.

Noskov [70] describes the point between a train and a loop as a *transitional point*, called n_i ($i \in \{1; 2; 3; 4; 5; 6\}$) in Figure 1.29. These transitional points are mobile along the chains, because of the fast adsorption/desorption of single repeated units.

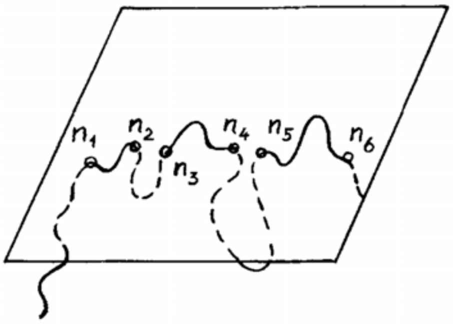

Figure 1.29: The layer of soluble adsorbed polymers at the interface is composed of trains (solid lines, as between n_1 and n_2) and loops extending in the bulk (dashed lines, as between n_2 and n_3) separated by transitional points (Figure adapted from B.A. Noskov [70]).

1.3.2.c Adsorbed layers of copolymers

When hydrophobic stickers (or *anchors*) are randomly grafted along the chain, the conformation is a bit different, as shown by Millet *et al.* [71, 72]. These authors studied modified poly(acrylic acid) (PAA): the backbone is a negatively-charged PAA chain, which adsorbs weakly at the interface and the stickers are hydrophobic alkyl chains. Using X-ray measurements, they studied the structure of polymer layers adsorbed on vertical films of water in air. They showed that almost all the hydrophobic stickers were adsorbed at the interface, and that the portion of chains between the stickers were stretched loops. The loops are stretched by the osmotic pressure of the counterions.

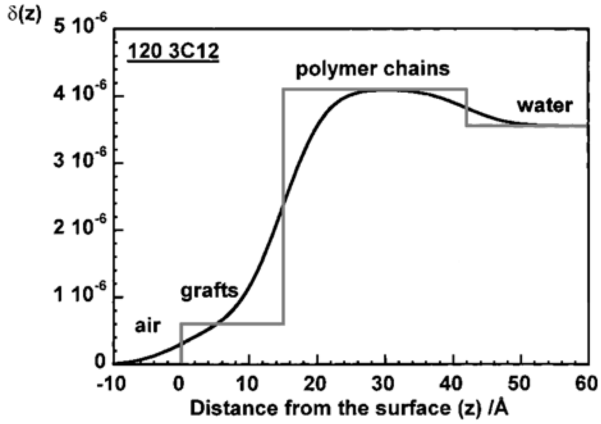

Figure 1.30: The density profile of electrons measured by F. Millet *et al.* through X-ray scattering is close to what is predicted by the model of Gennes-Alexander: a low density close to the interface, and a large region of high density in the brush, and then the bulk solution. The measured profile (black) is smoother than the step model (grey), partly because of the scattering due to the roughness of the vial interfaces. Figure adapted from Millet *et al.* [72].

In conclusion, the layer of copolymers is more stretched than the homogeneous polymers described by Noskov in Section 1.3.2.b, because of the competition of th osmotic pressure of the counter ions and the high adsorption energy of the grafts.

1.3.3 Equation of state

The interfacial tension of a polymer solution is affected by polymers at the interface, but the link between surface pressure Π and surface excess Γ (number of repeated units per unit area) is more complex than what was presented for classical surfactants in Section 1.2.3. It depends on the conformation of the polymer chains at the interface, which strongly depends on the nature of the polymers, on the surface excess, and on the solubility of the chains in the bulk phase.

Daoud *et al.* theoretically studied the surface pressure of interfaces covered by multiblock copolymers [73]. The polymers considered in their models consist in an succession of segments alternatively hydrophobic, and hydrophilic, as illustrated in Figure 1.31a. Their purpose was to mimic the adsorption of complex proteins.

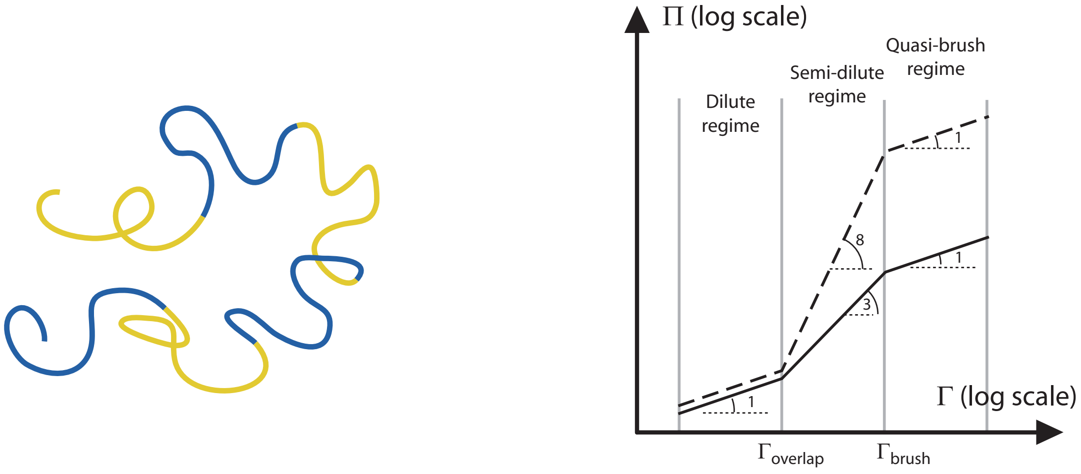

(a) Multiblock copolymers consists of a succession of hydrophobic (yellow) and hydrophilic (blue) segments. [73].

(b) Scaling laws for surface pressure Π as a function of surface excess Γ, for hydrophilic region in θ-solvent (dashed line), and in good solvent (solid). For $\Gamma < \Gamma_{\text{overlap}}$, the surface pressure is proportional to the surface excess (dilute regime), then to the surface excess to the power y ($y \in \{3; 8\}$) (semi-dilute regime) and finally, when $\Gamma > \Gamma_{\text{brush}}$ the surface pressure is proportional to the surface excess (quasi brush). Adapted from Daoud *et al.* [73]

Figure 1.31: Daoud *et al.* [73] studied the theoretical behaviour of multiblock copolymers, for various ranges of surface excess and different interactions polymer/solvent.

Surface pressure as a function of surface excess follows three successive power laws represented in Figure 1.31b. For low surface excess, molecules do not interact with each other, and acts as individual objects. Surface pressure Π follows a linear scaling law with surface excess Γ, and depends on temperature T and the Boltzmann constant k_{B}:

$$\Pi_{\text{dilute}} \simeq k_{\text{B}}T \cdot \Gamma/N = k_{\text{B}}T \cdot \Gamma_{\text{chains}} \quad . \tag{1.123}$$

For higher surface excess values, when $\Gamma > \Gamma_{\text{overlap}}$, the chains start to overlap: this is the semi-dilute regime. Surface pressure now depends on surface excess to a power y depending on the chain/solvent interaction:

$$\Pi_{\text{semi-dilute}} \simeq k_{\text{B}}T \cdot \Gamma^{y} \quad (y \in \{3; 8\}) \quad , \tag{1.124}$$

where $y = 3$ in good solvent conditions, and $y = 8$ in θ-solvent conditions.

When surface excess increases and $\Gamma > \Gamma_{\text{brush}}$, surface pressure rises, and the chains start to create more loops in the solution: this is the quasi-brush regime:

$$\Pi_{\text{quasi brush}} \simeq k_{\text{B}}T\, Z_{\text{B}}^{-1} \cdot \Gamma \quad , \tag{1.125}$$

where Z_{B} is the mean number of repeated units per loop.

The authors consider that the chains can eventually form two dimensional micelles at the interface, leading to intermediate regimes which are not presented here.

Graham and Phillips [74] have shown experimentally that Equation (1.123) is no longer appropriate for surface pressure exceeding $2-3\,\text{mN/m}$. Benjamins *et al.* [75] have performed experiments with various proteins, which tend to show that the transition toward quasi-brush regime occurs for surface pressure around $10\,\text{mN/m}$.

1.3.4 Adsorption dynamics of polymers

1.3.4.a Experimental observations

Millet *et al.* [71, 72, 76] and Aricov *et al.* [77] performed interfacial tension measurements for copolymer solutions as presented in Section 1.3.2.c: a hydrophilic backbone of negatively-charged poly(acrylic acid) randomly grafted with short hydrophobic alkyl chains. They observed a fast adsorption at short times, and then a slow adsorption over several hours. A typical adsorption plot of Millet and al [76] is represented in Figure 1.32. They divide the dynamics into three regimes: a first regime at short time scale, a logarithmic decay in an intermediate regime and a slow down at long time scale: after a few hours, the decay slows down, but even after more than 20 h, interfacial tension is still decaying.

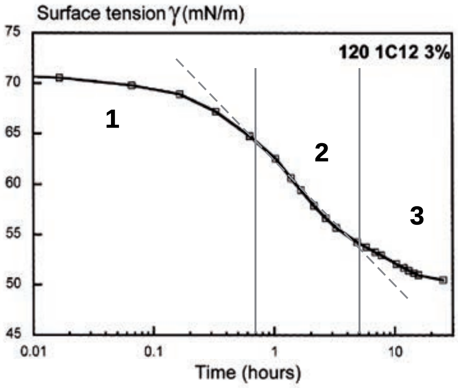

Figure 1.32: Typical evolution of interfacial tension γ with respect to time t during adsorption of hydrophobically-modified polymers. Three regimes (delimited by the grey lines) can be observed: (1) a fast regime at short time scale; (2) after a fraction of hour, interfacial tension decreases like $\log(t)$; (3) after a few hours the process slows down, but does not stop, even after more than 20 h. Figure adapted from Millet *et al.* [76].

1.3.4.b Theoretical models

Several models have been suggested to describe the adsorption dynamics of polymers, depending on the nature of the chains.

Johner and Joanny [78] studied theoretically the adsorption dynamics of block copolymers: in their study, one block is hydrophilic and the other is hydrophobic. The bulk chains in solution form micelles. They reported three steps in the adsorption process:

1. the diffusion-limited regime,
2. the brush regime,
3. the saturation regime.

Diffusion-limited regime: at short time, the adsorption is diffusion limited. During this regime, according to Section 1.2.3.d, the surface excess Γ is:

$$\Gamma = 2\Phi_{\mathrm{cmc}} \left(\frac{D\,t}{\pi} \right)^{1/2} \quad , \tag{1.126}$$

where Φ_{cmc} is the volume fraction of free chains in the bulk and D is the diffusion constant.

Quasi-brush regime: when the interface becomes crowded, the adsorption is limited by the deformation of the incoming chains. To access the interface despite the presence of the quasi-brush, the incoming chains stretch, as illustrated in Figure 1.33a. This deformation requires an energy E which limits the adsorption: only the chains which have enough energy to deform will adsorb. This energy barrier becomes significant only in the brush or quasi-brush regime, presented in Section 1.3.3. The adsorption flux at the interface scales as:

$$\frac{\mathrm{d}\Gamma}{\mathrm{d}t} \propto \exp\left(-\frac{E}{k_{\mathrm{B}}T} \right) \quad , \tag{1.127}$$

where the energy barrier is:

$$E \propto \Gamma^{5/6} \quad . \tag{1.128}$$

Integration of Equation (1.127) leads to a logarithmic adsorption with a characteristic time τ:

$$\Gamma \propto \ln \left(\frac{t}{\tau} \right)^{6/5} \quad . \tag{1.129}$$

Saturation regime: when the interface is crowded, and the chemical potentials of the chains in the brush and the one in the solution are similar, which kills the driving force of the adsorption. The interface becomes closer to its saturation coverage, the process slows down, and the surface excess tends toward a finite value Γ_{eq}. But this value is almost never reached experimentally.

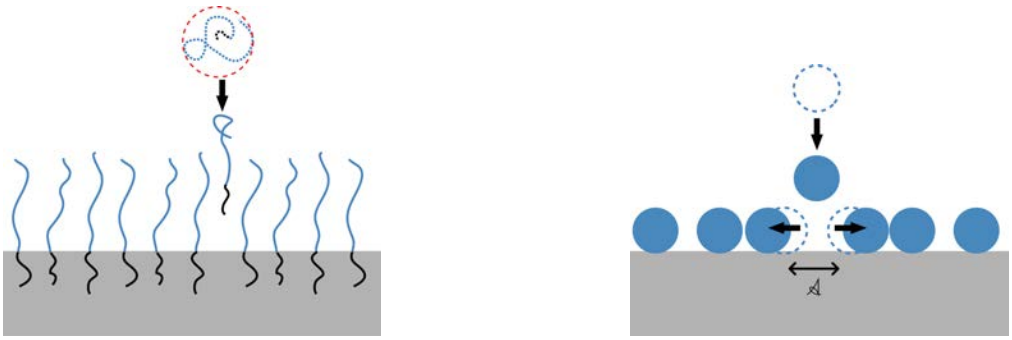

(a) In the model described by Johner and Joanny [78], the energetic barrier is due to the deformation of the incoming molecule.

(b) In the model suggested by Ward and Tordai [36], the energetic barrier is due to the clearing of the interface.

Figure 1.33: The models take into account different energy contributions to calculate the energetic barrier which limits the adsorption during the logarithmic regime.

Ligoure and Leibler [79] suggested a model for end-functionalized polymer chains: the chains are hydrophilic apart from a small chemical group at one end of the chain which is hydrophobic. The process is very similar to the one suggested by Johner and Joanny, but the energetic barrier of the brush regime is calculated in a different way and takes into account the variation of chemical potential along the height of the brush, leading to slightly different results:

$$\Gamma(t) = \frac{1}{B^{1/3}} \cdot \left(W\left(\frac{A\,B^2}{3\mathrm{e}^1} \cdot t \right) + 1 \right)^{1/3} \quad , \tag{1.130}$$

where A and B are two fitting parameters and the function W is the Lambert's function, also called omega function. It is defined by $W(x) = y \Leftrightarrow x = y \cdot \exp(y)$. Furthermore, they studied the desorption process due to the osmotic pressure which occurs when the brush is put in contact with pure solvent.

Ward and Tordai [36] described the adsorption of molecules which do not deform, as illustrated in Figure 1.33b. They predict similar regimes as Johner and Joanny: a first regime controlled by diffusion, an intermediate regime showing logarithmic adsorption, and a saturation regime. In the model of Ward and Tordai, the energetic barrier of the intermediate regime is due to the clearing of the portion of interface necessary to adsorb a new molecule. The critical area to be cleared is called $\mathcal{A}$. If γ is the interfacial tension of the interface with adsorbed molecules and γ_0 the interfacial tension of the pure interface, the energy needed to clear a portion $\mathcal{A}$ of the interface is:

$$E_{\mathrm{W-T}} = \gamma_0 \cdot \mathcal{A} - \gamma \cdot \mathcal{A} = \Pi \mathcal{A} \quad . \tag{1.131}$$

The complete equation ruling the adsorption depends on two kinetic constants k_{ads} and k_{des} respectively for adsorption and desorption, on the bulk concentration C_0, the surface excess Γ, and on two energetic barriers $E_{\mathrm{W-T}}$ and E_{des}, for the adsorption and the desorption:

$$\frac{\mathrm{d}\,\Gamma}{\mathrm{d}\,t} = k_{\mathrm{ads}} \cdot C_0 \cdot \exp\left(-\frac{E_{\mathrm{W-T}}}{k_{\mathrm{B}}T}\right) - k_{\mathrm{des}} \cdot \Gamma \cdot \exp\left(-\frac{E_{\mathrm{des}}}{k_{\mathrm{B}}T}\right) \quad . \tag{1.132}$$

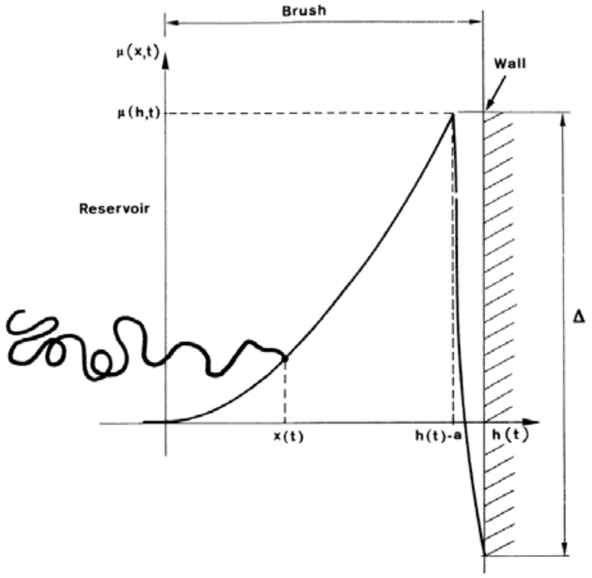

Figure 1.34: Energetic landscape for a polymer chain adsorbing from the bulk (left) to an interface (right) in the logarithmic regime described by Leibler *et al.* The polymer chain is hydrophilic and terminated by a hydrophobic group. The adsorption is limited by the energetic barrier $\mu(h,t)$ but occurs because of the adsorption energy Δ. Figure from Ligoure and Leibler [79].

Far from saturation, desorption flux in negligible with respect to adsorption flux, leading to a logarithmic adsorption.

1.3.5 Rheology of polymer layers

The interfacial rheology of polymer layers presents rich behaviours, which depend on the nature of the polymers.

1.3.5.a Rheology of polymer monolayers

The interfacial tension remains homogeneous and isotropic during solicitation, similarly to surfactant layers presented in Section 1.2.3 because of the fast exchanges between trains and loops.

Barentin *et al.* [80] studied the compression of telechelic polymers (hydrophilic chains of poly(ethylene oxyde) (PEO) with two hydrophobic ends (C_{12} alkyl chains)) at the air/water interface in a Langmuir-trough. The isotherms presented in Figure 1.35 show that for large area, the surface pressure follows the prediction of semidilute regime in good solvent ($\Pi \propto \Gamma^3$). For higher compression (smaller area), the isotherms of the telechelic polymer and of pure PEO differ: PEO desorbs easily and the surface pressure levels off on a plateau, while the telechelic polymer (C_{12}-PEO-C_{12}) is anchored at the interface by the alkyl ends, and hence only the center of the chain desorbs. For higher compression, the C_{12} anchors desorb, leading to the second short plateau on the isotherm of the telechelic polymers.

Noskov *et al.* [81] measured the dilational modulus (presented in Section 1.2.4.c) of triblock copolymers, made of two segments of hydrophilic PEO, connected by a segment of hydrophobic

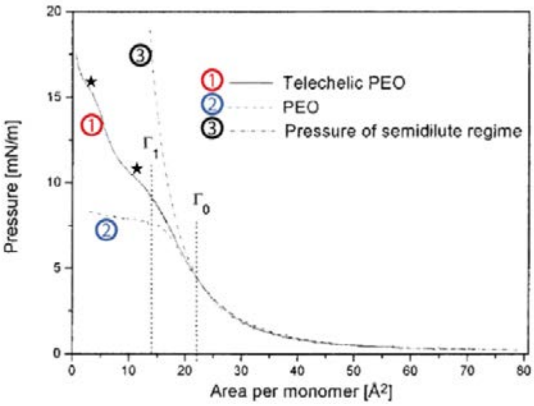

Figure 1.35: Isotherms of telechelic polymers ① (hydrophilic poly(ethylene oxyde) chain with hydrophobic alkyl chains (C_{12}) at both ends) and of chains of poly(ethylene oxyde) ②. For large areas (larger than the position Γ_0), the isotherms follow the model of the semidilute regime ($\Pi \propto \Gamma^3$) ③. For higher compression (smaller area), the isotherms do not follow the model, because of polymer desorption: pure PEO ② desorb easily leading to a nearly constant surface pressure, whereas telechelic chains ① first partially desorb (only the PEO part), and then the alkyl anchors desorb, leading to the two plateaus (inflection points reported by $\star$). Figure adapted from Barentin *et al.* [80].

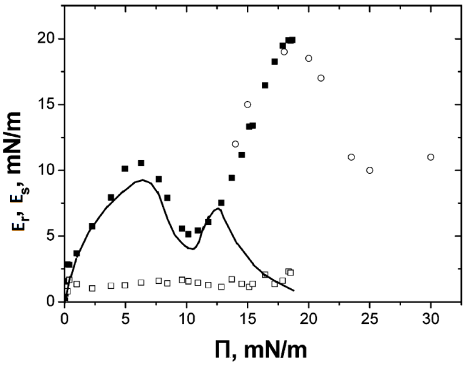

Figure 1.36: Dilational modulus for the compression of monolayer of triblock copolymers: hydrophilic segments of poly(ethylene oxyde) connected by a segment of hydrophobic poly(propylene oxyde). The modulus is plotted versus the surface pressure. Real part of the modulus is represented by empty circles and filled squares, and the imaginary part by the empty squares. The solid line represent the modulus extracted from the isotherm. Adapted from Noskov *et al.* [81]

poly(propylene oxyde) (PPO). They measured the dilational modulus in oscillatory solicitations, in order to have the real part (in-phase response, represented by filled squares and empty circles in Figure 1.36)) and the imaginary one (out-of-phase response, represented by empty squares in Figure 1.36)) of the modulus. They measure the dilational modulus as a function of surface pressure. They measure a low out-of-phase response. They showed that for $\Pi \in [5, 10]$ mN/m and $\Pi > 20$ mN/m, the real part of the modulus decreases when surface pressure increases. This behaviour is the signature of phase transitions, conformational changes or desorption. They also observed that the dilational modulus can be extracted from the isotherm in small deformation (solid line in Figure 1.36).

1.3.5.b Rheology of polymer multilayers

Ferri *et al.* [43, 82] studied polymer multilayers assembled at liquid interfaces, directly on pendant drops. They measured the modulus of polyelectrolyte multilayers assembled as illustrated in Figure 1.37: a negatively charged surfactant adsorb at the interface, and then layers of polymers are adsorbed layer-by-layer, as presented in Section 1.1.2. The polycation is poly(allylamine hydrochloride) (PAH), and the polyanion is poly(sodium 4-styrenesulfonate) (PSS).

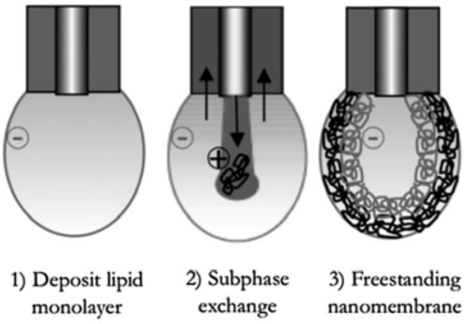

Figure 1.37: Layer-by-layer adsorption of elastic polyelectrolyte complex at an interface in the pendant-drop geometry, by Ferri *et al.* [43]. The interface is rinsed from the inside of the droplet.

From the shape of the drop, considering the $\underline{\underline{T}}_{\text{pure}}$, $\underline{\underline{T}}_{\Gamma}$ and $\underline{\underline{T}}_{\text{elastic}}$ contributions of interfacial tension, they obtained the Young modulus of the interface, Y_{s} which takes into account the variations of $\underline{\underline{T}}_{\Gamma}$ and $\underline{\underline{T}}_{\text{elastic}}$. They found that Y_{s} increases with the number of layers and that the equivalent bulk Young modulus $Y = \frac{Y_{\text{s}}}{h}$ (where h is the thickness of the membrane) decreases with the number of layers. According to the authors, this behaviour is due to the fact that for small number of layers, because of confinement, the chains behave differently, leading to higher modulus.

To the best of our knowledge, the interfacial rheology of polymer multilayers has been seldom studied, and there is therefore substantial work to be done to identify the main phenomena ruling these properties and the key levers of control to tune them.

To summarize this section:

Polymers are long linear molecules which consist in a large number a repeated units. The interaction with the solvent determines how developed or collapsed the molecules are in solution.

The shape of the molecules at the interface depends on the surface excess and on the affinity of the chains with the interface, which depends on the nature of the chains. When the surface excess is high enough, some parts of the chains are out of the interface plane and form a brush.

For small surface excess, surface pressure is proportional to surface excess. When the chains start to overlap, depending on the polymer/solvent interaction, surface pressure is proportional to surface excess to the power 3 or 8 (respectively for good solvent or θ-solvent). When the chains are significantly deformed out of plane because of the high surface excess, surface pressure is proportional to surface excess again.

The adsorption dynamics of polymers at interfaces successively describes three regimes: a diffusion-limited regime (scales with the square root of time), a brush regime (scales with logarithm of time) and a saturation regime (exponential dynamics towards equilibrium state).

Interfacial rheology of polymer layers shows that monolayers exhibit liquid behaviours, with conformational changes, phase transitions or desorption, leading to plateaus in the isotherms. When the interaction is strong between the layers, multilayers can show viscoelastic properties, both in compression and in shear deformation.

1.4 Conclusion

In this chapter, we presented a few methods to produce microcapsules. We especially described the advantages of the Layer-by-Layer (LbL) adsorption, and of microfluidics. The LbL method allows a fine control of the membrane composition whereas microfluidics enables precise handling of the capsules. We also introduced the concept of interfacial tension and more generally the complexity of the interfacial rheology. We showed that in the specific case where interfacial tension is a scalar constant with respect to time and position, droplets deformation in a viscous flow field can give access to interfacial tension. Moreover we presented the basis of polymer physics and especially of polymers at interfaces. We showed that the adsorption dynamics can be diffusion limited or kinetically limited. In the latter case, depending on the model and on the nature of the molecules, the energetic barrier comes either from the deformation of the adsorbed polymer layer or from the incoming-chains deformation. Finally we had an overview of the rheology of polymer monolayers, and polymer multilayers. We saw that the rheology of monolayers is mostly tuned by adsorption/desorption processes leading to variations of surface excess. We presented at last a case of multilayers where the membrane is elastic and described by an interfacial Young modulus.

This review raises several questions that we would like to address. We wonder first if we can combine the advantages of the LbL method and those of microfluidics to build large populations of microcapsules of controlled size and composition. Moreover, to have a fine understanding of the link between the interactions at the nano-scale and the rheological properties of the membrane, we will have to select a model system in which we will be able to tune independently the different kinds of interaction, with the interface and between the layers layers themselves. With such a system, it should be possible to study the effect of these different interactions on the polymer-assembly dynamics, and on the rheological properties of these assemblies.

Moreover the measurement processes themselves raise questions. The pendant-drop apparatus for example is often used to measure interfacial properties, but because of the complex shape of the pendant drops, the relevance of these measurements is sometimes called into question. We suggest in this thesis to address this question and to present the range of validity of this method. At a smaller scale, experiments of droplets deformation in microfluidics always neglect the effect of the droplet itself on the flow field. We will offer a complete analysis of the problem and explore the conditions in which such approximation is correct. In this geometry, no prediction of the droplet evolution with respect to time has been suggested in similar systems. We can wonder why. This is all of these questions that we will attempt to answer in the following chapters.

Chapter 2

Monolayers and multilayers of polymers in a model geometry

Contents of this chapter

2.0 Introduction

We would like to use model membranes to understand the assembly process of multilayers and relate their dynamics to the interaction of the polymers with the interface. Moreover we would like to link the rheological properties of monolayers and multilayers to the nature of the polymer chains.

As we have seen in the previous chapter, there is a need for model interfaces in terms of composition and shape. To this aim we have choosen a model system in which we can independently tune the anchoring energy of the polymers with the interface, and the interaction between the different polymer layers. Moreover, we will use a rising bubble as a model interface: the interface of the bubble can indeed be easily compressed or dilated. The interface of the rising bubble will be prepared and probed in a pendant-drop apparatus.

In Section 2.1, I will present the polymers and the different setups used in this chapter. Then I will summarize in Section 2.2 the work that was previously performed in our group on this topic and which I will consider as a starting point for my thesis. In Section 2.3 we will study the adsorption dynamics of a range of hydrophobically-modified polymers for which we can tune the anchoring energy with the interface. We will describe and model how this dynamics depends on the anchoring energy. As we will see, because of their high anchoring energy, these polymers will be later used as a first layer. Consequently we need to investigate the rheology and the stability of this layer. In Section 2.4 we will analyse how this anchoring energy rules the rheological behaviour of such polymer monolayers upon compression or dilatation. Our goal in Section 2.5 will be to understand how the anchoring energy and the inter-layer interactions set the rheological properties of the multilayers. We will focus on the compression of multilayers in the pendant-drop apparatus. Although the pendant-drop apparatus is convenient to study monolayers and to assemble multilayers, the deformations of pendant drops (or rising bubbles) are a complex combination of compression and shear deformation. Owing to this statement, in Section 2.6 we will compare the results of compression in pendant-drop apparatus with isotropic compression or shear deformation of planar interfaces for a given bilayer. This work will enable us to set the limitations and the range of validity of the pendant-drop measurements.

2.1 Materials and methods

2.1.1 Polymers: choice and preparation

The polymers have been chosen to be soluble in water, to adsorb spontaneously at the oil/water and air/water interfaces, and to exhibit interactions between the layers.

2.1.1.a Interaction between the polymers

We chose to work with polymers that interact through hydrogen bonds. The hydrogen bond (H-bond) is a directional bond of the order of $\sim 10\,k_{\mathrm{B}}T$, which links an H-donnor (typically an acid function) to an H-acceptor (typically a chemical group showing conjugated lone pairs). The H-bond is exothermic and consequently weaken with temperature.

The proton donors are a series of poly(acrylic acid) of various hydrophobicity shown in Figure 2.1: poly(acrylic acid) (PAA), poly(methacrylic acid) (PMAA), hydrophobically-modified PAA (PAA-α-C_{12} and PAA-α-C_8 described in Section 2.1.1.b).

(a) Poly(acrylic acid): PAA. (b) Poly(methacrylic acid): PMAA.

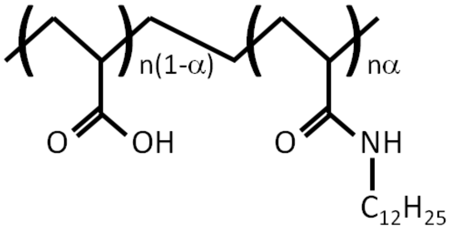

(c) Grafted poly(acrylic acid): PAA-α-C_{12} (similarly, we have PAA-α-C_8).

Figure 2.1: Proton donors.

The proton acceptor is polyvinylpyrrolidone (PVP). As illustrated in Figure 2.2, hydrogen bonds exist between the hydrogen of the poly(acid) and PVP.

(a) Polyvinylpyrrolidone (PVP) (b) Hydrogen bonds between PVP and PAA.

Figure 2.2: The proton acceptor (polyvinylpyrrolidone (PVP)) establishes hydrogen bonds with the proton donors.

As it will be explained in Section 2.2, PAA interacts with PVP only through hydrogen bonds, whereas PMAA interacts with PVP through hydrogen bonds and hydrophobic interactions. Hydrophobic interaction is an effective attraction which concerns slightly hydrophobic molecules soluble in water. If the attraction between molecules of water is stronger than the attraction between polymer chains and water, brownian motion leads to an effective attraction between the chains.

Consequently, hydrophobic interaction is an endothermic interaction which becomes stronger with temperature, and which, unlike H-bonds is not directional.

Characteristics of the commercial polymers. PAA is provided by Polysciences Inc. Gel permeation chromatography (GPC) measurements gives us the length of the chains: $M_\mathrm{n} = 50\,000\,\mathrm{g/mol}$ and $M_\mathrm{w} = 100\,000\,\mathrm{g/mol}$.
PMAA is provided by Polysciences Inc, and the molecular weight is $M_\mathrm{w} = 100\,000\,\mathrm{g/mol}$.
PVP is provided by Sigma-Aldrich and $M_\mathrm{w} = 30\,000\,\mathrm{g/mol}$.

2.1.1.b Grafted polymers: PAA-α-C$_\mathrm{n}$

To combine a good solubility of the chains in water, and a good adsorption at the interface, we use hydrophobically modified PAA.

The polymer chains consist in a hydrophilic backbone of PAA, grafted with hydrophobic alkyl chains, as allustrated in Figure 2.3. The length of the grafts n (number of carbons) and the grafting degree α (number of grafts divided by the number of repeated units) are controlled. Such polymer chains are called PAA-α-C$_\mathrm{n}$, where $\alpha \in [0, 100]$ is the percentage of grafting units.

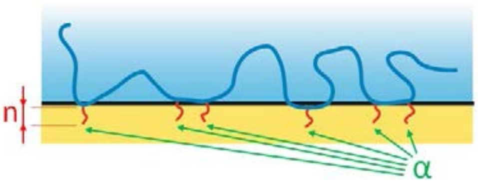

Figure 2.3: PAA-α-C$_\mathrm{n}$ chains consist in hydrophilic PAA backbone on which a controlled proportion α of hydrophobic alkyl chain of controlled length n (number of carbons) are grafted.

PAA-α-C$_\mathrm{n}$ ($n \in 8; 12$) was chosen for its large anchoring energy with the interface.

Synthesis and constraints. This modified polymers are synthesized in the laboratory by Pr. Perrin, starting from linear PAA. The synthesis has been developed by Wang *et al.* [83], and is summarized in Figure 2.4. The purification of the polymers requires to use the deprotonated form of the polymer, so the polymer is stored in its basic form.

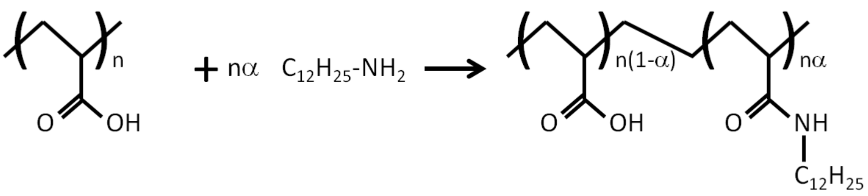

Figure 2.4: Summary of the synthesis of the hydrophobically modified PAA developed by Wang *et al.* [83] PAA-α-C$_{12}$.

Higher adsorption is expected for higher degree of grafting α and longer grafts. The chains without grafts are in good solvent in water, but with too many grafts, they could be in bad solvent, or even not soluble in water. Consequently, the grafting must be carefully controlled, to have chains which are soluble in water and would adsorb at the interface.

Characterization of the obtained chains. We have studied five types of grafted polymers:

- PAA-0.7-C_{12},
- PAA-0.8-C_8,
- PAA-2.4-C_8,
- PAA-3.8-C_8,
- PAA-4.3-C_8.

All these polymers are soluble enough to be dissolved at 1 wt% (weight fraction) in water. Low-shear measurement of the viscosity of PAA and PAA-0.8-C_8 solutions at shear rate $50\,s^{-1}$ showed that $\eta_{PAA} = 1.40\,mPa \cdot s$ and $\eta_{PAA-0.8-C_8} = 1.07\,mPa \cdot s$, as presented in Figure 2.5. Viscosities of PAA, PMAA and PAA-0.8-C_8 are slightly higher that viscosity of water ($\eta_{water} = 1\,mPa.s$) and do not depend on shear rate. Moreover, we observe that the solution of PAA-0.8-C_8 is less viscous that the solution of non-grafted PAA. This means that because of the low concentration (lower than the overlap concentration) there is no intermolecular interaction which would increase the viscosity, and that the hydrophobicity of the grafts decreases the size of the polymer coils: the hydrophobic grafts exhibit intramolecular hydrophobic interactions and thus decrease the size of coils.

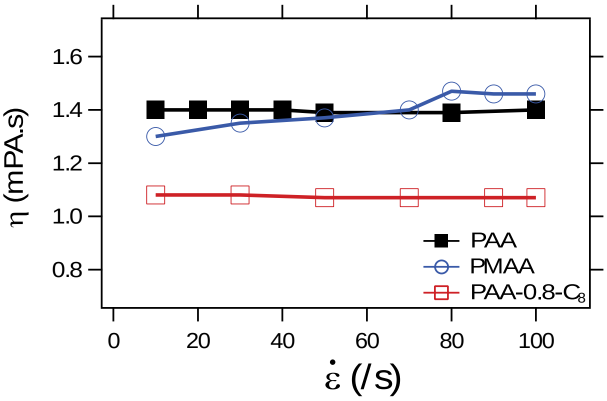

Figure 2.5: Viscosity of polymer solutions of PAA, PMAA and PAA-0.8-C_8 versus shear rate (1 wt%). Solutions are newtonian (no dependency on shear rate), which indicates that there is no intermolecular interaction. Furthermore, PAA-0.8-C_8 is less viscous than PAA, which means that the polymer coils are smaller, due to intramolecular hydrophobic interaction between the grafts.

2.1.1.c Preparation of the solutions

The polymer are dissolved in water at 1 wt% and the solutions are stirred 24 h for linear chains, and 72 h for grafted chains. The solution are then set to pH 3, with solution of HCl 1 mol/L or NaOH 1 mol/L. The solutions are stored at 5 °C and thermalized at room temperature one night before the experiments.

In order to avoid modification of the polymer properties, the solution are kept no longer than a week. Moreover, the vials containing the polymer powder are sealed to prevent moisture to damage the chains over time.

2.1.2 Pendant-drop apparatus: protocol

Interfacial tension is measured using a pendant-drop apparatus Tracker provided by Teclis ©. The apparatus allows an easy assembling of the multilayers, the deformation of the interface, and interfacial tension measurements.

2.1.2.a Set-up

A millimeter size air bubble is blown in 5 mL of water solution at the tip of a needle connected to a syringe, as presented in Figure 2.6a. The needle is connected through a T-junction to a pressure probe, and pictures of the bubble are recorded and transferred to a computer. Temperature of the syringe and of the water solution are controlled and set to 20 °C. Image analysis provides the volume of the droplet allowing a monitoring of the volume.

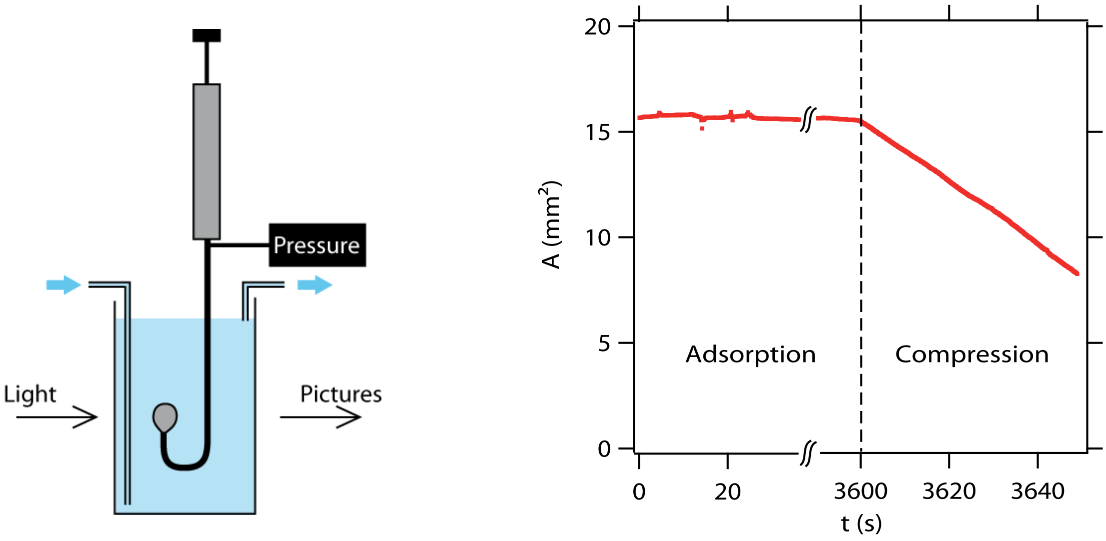

(a) An air bubble is pinned at the tip of a needle connected to a syringe. A pressure probe is also connected to the setup. Pictures of the bubble are made to measure the volume, the area and the interfacial tension. Tubings allows a rinsing of the water solution to adsorb additional layers.

(b) Two steps of a pendant-drop experiment: adsorption (constant area), compression (or dilatation) (decreasing area).

Figure 2.6: Setup and steps of a pendant-drop experiment (in the rising bubble configuration).

The experiments consist in two steps illustrated in Figure 2.6b:

- preparation of the interface,
- deformation of the interface,

Preparation of the interface. The preparation of the multilayers is achieved by successive phase changes, allowed by the two tubing in Figure 2.6a. The bubble is blown in a first solution of polymer at pH 3, as illustrated in Figure 2.7a. To add a second layer, the solution is rinsed with a solution of hydrochloric acid at pH 3 (Figure 2.7b), and then rinsed with a second polymer solution (Figure 2.7c). Before the measurements on multilayers, the interface is rinsed with a solution of

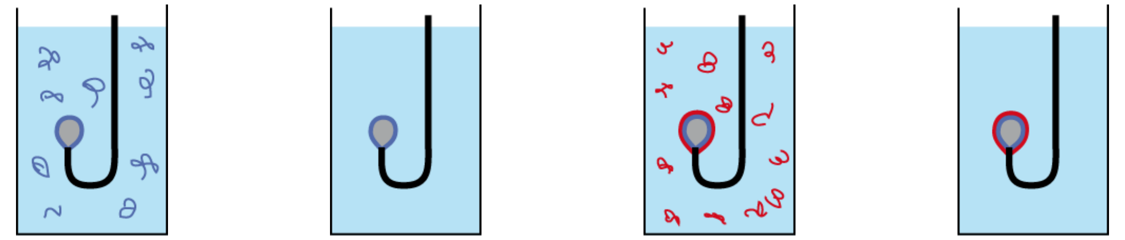

(a) Adsorption of the first layer.

(b) Rinsing of the first polymer.

(c) Adsorption of the second layer.

(d) Rinsing of the second polymer.

Figure 2.7: Preparation of the multilayers at the air water interface. (a) The polymer in solution spontaneously adsorb at the interface. (b) The solution is rinsed to keep only the polymer at the interface. (c) A new polymer solution is introduced to adsorb the second layer. (d) The solution is rinsed to clear the polymer in the solution, in order to reproduce steps (a) and (b), or to start the deformation of the interface.

hydrochloric acid (Figure 2.7d). The different steps are detailed in Table 2.1. During all the preparation, the volume is monitored to be constant, despite any dissolution of the air in water.

For the monolayers, the deformation starts after the adsorption of the first layer, without rinsing.

Step	Duration (min)	Action
1	60	Adsorption of the first layer
2a	15	Rinsing with acid water (HCl, pH 3) (flow rate: 10 mL/min)
2b	15	Rest
3a	5	Rinsing with new polymer solution (flow rate: 10 mL/min)
3b	25	Adsorption of the new polymer
4a	15	Rinsing with acid water (HCl, pH 3) (flow rate: 10 mL/min)
4b	15	Rest

Table 2.1: Steps of preparation of the bilayers in pendant-drop apparatus. The preparation of the monolayer stops after step 1, before rinsing. For more than three layers, steps 3 and 4 must be reproduced for every additional layer.

Deformation of the interface. To deform the interface, the volume of the bubble is modified using the syringe. An increase of the volume dilates the interface, and a decrease of the volume compresses the interface. The volume follows a ramp, which leads, for small deformation, to a linear variation of the area. Deformation were reproduced for various maximal deformations and deformation speeds.

2.1.2.b Two measurements of interfacial tension

Classical method: Laplacian fit. This first method is valid under a few conditions: interfacial tension must be homogeneous and isotropic, and the droplet must be axisymmetric. Consequently, this method can only be used for interfaces corresponding to the model 2 of Table 1.1, called *liquid interfaces*. At rest, the shape of a bubble in water results from a balance between buoyancy and interfacial tension: buoyancy elongates the bubble, while interfacial tension keeps it as spherical as possible.

We have seen in Section 1.2.1 that a curved interface applies a pressure difference between the two sides of the interface which is proportional to interfacial tension. This pressure difference is described by Young-Laplace Equation (Equation 1.2). The balance of the Laplace pressure and the hydrostatic pressure yields:

$$(\rho_{\text{out}} - \rho_{\text{in}}) \cdot gz - \gamma \left(\frac{1}{R_\xi} + \frac{1}{R_\Phi} \right) = C^{ste} \quad , \tag{2.1}$$

where z is the height, ρ_{in} and ρ_{out} are respectively the inner and outer density, γ is the interfacial tension, g is the gravity, and R_ξ and R_Φ are the two radii of curvature, as represented in Figure 2.8a.

Integration of Equation 2.1 leads to theoretical shapes of the bubble as function of interfacial tension. The calculated shapes are compared with the actual shape extracted from the pictures recorded by the computer, as presented in Figure 2.8b. Fitting the actual shape with the theoretical one gives the interfacial tension.

(a) Geometrical and physical parameters describing the shape of the bubble: height z, radii of curvature R_ξ and R_Φ, densities ρ_{in} and ρ_{out}.

(b) Picture of an air bubble in water captured by the apparatus. Picture analysis gives the volume, the area, and interfacial tension by comparison with the theoretical shapes. The bubble appears black because of the high optical index mismatch, and the high curvature of the interface. Scale: the needle at the bottom has a diameter of 1.2 mm.

Figure 2.8: The analysis of the shape of the bubble gives a measurement of interfacial tension.

Second method: pressure measurement. The previous method works only when the interface is liquid (homogeneous and isotropic interfacial tension). To investigate the case of viscoelastic interfaces, a second method is required. In this case, the tension of the interface depends on the direction along which the tension is measured, as illustrated in Figure 2.9. The Young-Laplace Equation (Equation 1.2) becomes [84]:

$$\Delta P = \frac{T_\xi}{R_\xi} + \frac{T_\Phi}{R_\Phi} \quad , \tag{2.2}$$

where T_ξ and T_Φ are the tensions in the two orthogonal directions of the interface, $\Delta P = P_{\text{out}} - P_{\text{in}}$, where P_{out} and P_{in} are respectively the pressure inside the bubble and outside the bubble, as presented in Figure 2.9.

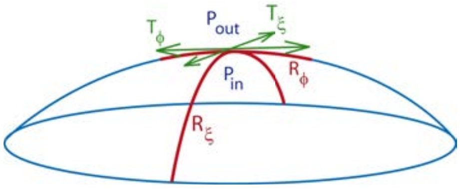

Figure 2.9: When the interface is viscoelastic, tension depends on the position and on the orientation. Two directions can be defined, ξ and Φ, and for each direction, there are a tension, T_ξ and T_Φ, and a radius of curvature, R_ξ and R_Φ. These tensions and curvatures usually lead to an inside pressure P_{in} higher than the outside pressure P_{out}.

It is difficult to know the whole field of tension from the pressure measurement. However, at the apex of the bubble, for symmetry reasons, the two directions ξ and Φ are equivalent: $T_\xi = T_\Phi = T_{\text{apex}}$ and $R_\xi = R_\Phi = R_{\text{apex}}$. Equation (2.2) becomes:

$$\Delta P = 2 \cdot \frac{T_{\text{apex}}}{R_{\text{apex}}} \quad . \tag{2.3}$$

The radius of curvature and the pressure being measured, Equation (2.3) gives access to the tension at the apex T_{apex}:

$$T_{\text{apex}} = \frac{1}{2} \cdot \Delta P \cdot R_{\text{apex}} \quad . \tag{2.4}$$

2.1.2.c Comparison of the methods

Both methods are always simultaneously used.

When the two measurements give the same result ($T_{\text{apex}} = \gamma$), it means that the assumptions of the Laplacian fit are verified. Consequently, the interface is liquid: interfacial tension is homogeneous and isotropic.

When the two measurements do not give the same result ($T_{\text{apex}} \neq \gamma$), it means that the assumptions of the Laplacian fit are not verified. Interfacial tension is either not homogeneous or not isotropic. Consequently, we know that the interface is viscoelastic, and hence that interfacial tension depends on the position and on the direction along which the tension is measured. In this case, the value of γ given by the first method is irrelevant, and T_{apex} given by the second method gives the tension of the interface at the apex.

2.1.3 Radial trough: geometry and protocol.

The radial trough has been developed by Vermant *et al.*. The set up is presented in Figure 2.10: a region of the air/water interface is isolated by a PTFE ribbon hold by 12 arms. The arms can move to increase or decrease the interfacial area of the inner region from $A_{\text{min}} = 34\,\text{cm}^2$ to $A_{\text{max}} = 136\,\text{cm}^2$. The arms are controlled through a computer to be synchronized in order to preserve symmetry and to ensure smooth variations of the area. A cylindrical rod is placed in the center of the trough to measure interfacial tension similarly to the Wilhelmy plate method presented in Section 1.2.2.a.

To prepare the PVP/PMAA multilayer at the interface, the trough is rinsed with water or polymer solutions using peristaltic pumps. The inlets are in the positions marked by red arrows

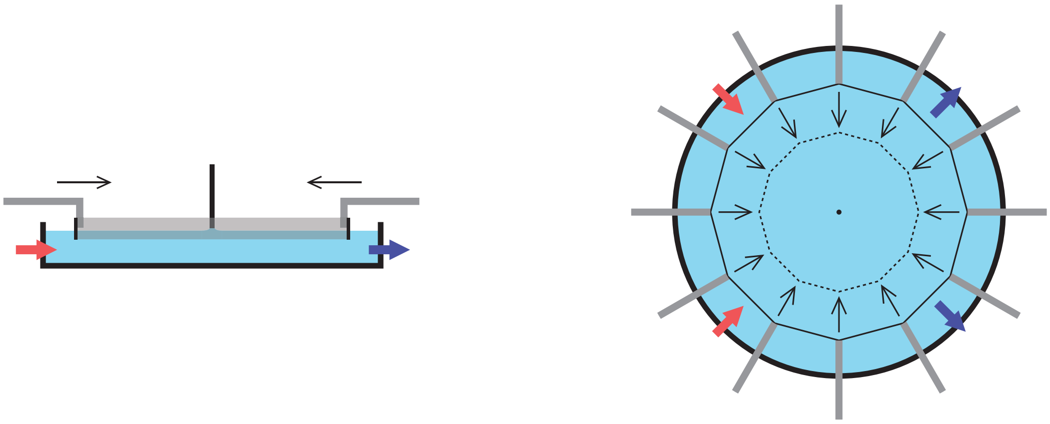
(a) Side view. (b) Top view.

Figure 2.10: Top view of radial trough. A PTFE ribbon is placed at the air/water interface and moved by twelve arms to compress or dilate the interface. Blue and red arrows represent the fluxes for the rinsing.

in Figure 2.10, and the outlets are marked by blue arrows. The volume of the trough is 300 mL. Accordingly, to add the second layer the trough is rinsed with 900 mL of water, and with 600 mL of PMAA solution, as reported in Table 2.2. The rod is placed after the preparation of the interface.

Step	Duration (min)	Action
1	60	Adsorption of PVP (300 mL)
2	45	Rinsing with acid water (HCl, pH 3) (900 mL)
3	30	Rinsing with PMAA solution (600 mL)
4	45	Rinsing with acid water (HCl, pH 3) (900 mL)

Table 2.2: Steps of preparation of the bilayers in radial trough.

2.1.4 Interfacial rheometer

Shear measurements were performed in an TA Instrument rheometer mounted with a Double Wall Ring as presented in Section 1.2.4.f. Rinsing was performed using syringe pumps and a modified trough with four inlets in the bottom and four lateral outlets. This modified trough was built by Vermant *et al.*. The volume of the trough is 50 mL, and the rinsing was performed according to Table 2.3. After the preparation of the interface, the measuring ring is placed at the interface.

Step	Duration (min)	Action
1	60	Adsorption of PVP (50 mL)
2	30	Rinsing with acid water (HCl, pH 3) (200 mL)
3	30	Rinsing with PMAA solution (200 mL)
4	30	Rinsing with acid water (HCl, pH 3) (200 mL)

Table 2.3: Steps of preparation of the bilayers in shear rheometer.

We have a set of polymers which adsorb at the interface. By varying the nature of polymers, we can tune the anchoring energy of the first layer and the interaction between the layers. Some features of this system have been studied in our group in the context of an industrial thesis which is the basis on which this work has been built. We summarize now the key points of this thesis.

To summarize this section:

The polymers used to build the monolayers and the multilayers are: Poly(vinylpyrrolidonne) (PVP), poly(acrylic acid) (PAA), poly(methacrylic acid) (PMAA), and hydrophically-modified PAA (PAA-α-C_n). All these polymers are amphiphilic polymers soluble in water.

PVP and PAA interact through hydrogen bonds. PVP and PMAA interact through hydrogen bonds and hydrophobic interactions.

PAA-α-C_n consists in a backbone of PAA with hydrophobic grafts. α is the degree of grafting (percentage), and n the length of the grafts (number of carbons).

The pendant-drop apparatus allows the preparation of monolayers and multilayers, and the measurement of interfacial tension with two methods: the Laplacian fit and the pressure measurement. The comparison of the two methods indicates whether the interface is liquid (homogeneous and isotropic interfacial tension) or viscoelastic.

Radial trough and interfacial rheometer allow independent measurements of dilational and shear properties.

2.2 Previously performed studies

In the scope of an industrial thesis carried out in our group by S. Le Tirilly, some features of layer-by-layer (LbL) membranes had been investigated when I started. More precisely, she showed that layers interacting by hydrogen bounds are a matter of interest, while the classical LbL membranes use electrostatic interactions. Moreover she selected a polymer system for the strength of the interactions taking place between the layers and the possibility to tune these interactions. I present here the main results of her work.

2.2.1 Interactions between the polymers

Using isothermal titration calorimetry of the polymer complexes in solution, Le Tirilly *et al.* [21] measured a strong endothermic interaction upon addition of PVP in a PMAA solution, showing that the PMAA/PVP complexes interact through strong hydrophobic interactions (Figure 2.11). In the same conditions, the interaction between PAA and PVP is weakly exothermic. They note that, for technical reasons, these measurements were performed at pH = 4, where the hydrogen bonds between the polyacids and PVP are weak because this pH is close to the pKa of the polyacids. Therefore, their ITC measurements are mostly sensitive to the hydrophobic interaction between the polyacids and PVP. At $pH = 3$, they expect that the hydrogen bonds between PAA and PVP are stronger, which is confirmed by the fact that PAA/PVP solutions become turbid at this pH. They conclude that, at $pH = 3$, PMAA/PVP interact through strong hydrophobic interactions and hydrogen bonds, while PAA/PVP interact mostly with hydrogen bonds.

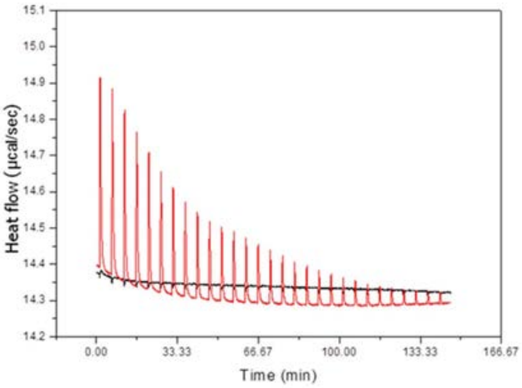

Figure 2.11: ITC experiment showing the heat effect produced by injecting 10 μL aliquots of a 10 mM PVP solution in water (pH 4) to a 1 mM PMAA solution (red curve) and by injecting 10 μL aliquots of a 10 mM PVP solution in water (pH 4; $T = 25\,°C$) to pure water (pH 4; black curve; $T = 25\,°C$). Peaks directed upward correspond to an endothermic interaction (hydrophobic interaction).

2.2.2 Effect of hydrophobic interactions

Interfacial rheometers as presented in Section 1.2.4.f have been used by Le Tirilly *et al.* [21] to measure precisely the shear modulus of polymer multilayers at dodecane/water interface, in order

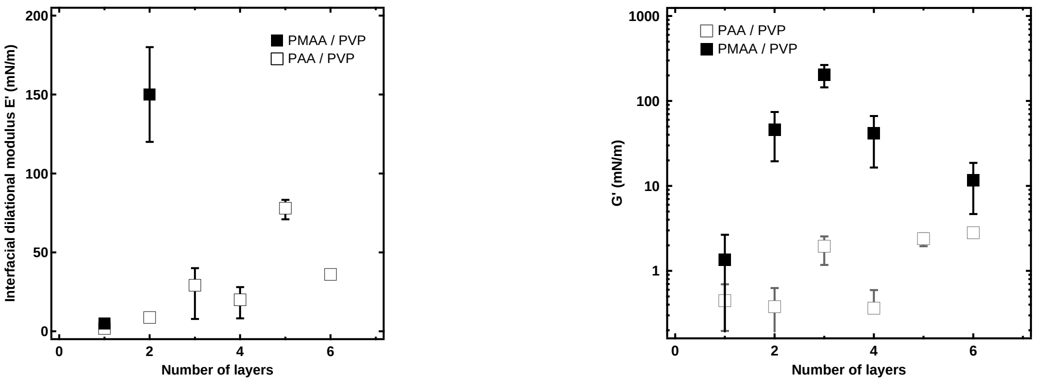

(a) Compression elastic modulus of PAA/PVP and PMAA/PVP multilayers versus the number of layers. There is no elasticity for the monolayers of PAA and PMAA. The elastic modulus of PAA/PVP multilayers remains small and comparable to the Gibbs modulus, while the elastic modulus of PMAA/PVP is high.

(b) Shear elastic modulus of PAA/PVP and PMAA/PVP multilayers versus the number of layers. The shear modulus of the monolayers of PMAA and PAA are comparable, and of the order of the modulus of PAA/PVP multilayers, while the moduli of the PMAA/PVP are more than ten times greater.

Figure 2.12: Compression and shear elastic moduli of multilayers of polyvinylpyrrolidone (PVP) with poly(acrylic acid (PAA), or with poly(methacrylic acid) (PMAA) on dodecane/water interface. The moduli are stronger with PMMA than with PAA, and increase with the number of layers. Angular frequency is $\omega = 0.6\,\mathrm{rad/s}$. Figure from Le Tirilly *et al.* [21].

to complement and support their pendant-drop measurements which provide compression moduli. The multilayers consist in alternated layers of PAA, PAA-1-C_{12} or PMAA, and PVP.

They measured that the compression and shear moduli of monolayers are weak, as well as the moduli of PAA/PVP multilayers. On the contrary, the shear and compression elastic moduli of PMAA/PVP multilayers are approximately ten times higher, of the order of 100 mN/m, as presented in Figure 2.12. Elastic properties are observed for PMAA/PVP multilayers only, and neither for monolayers nor for PAA/PVP multilayers.

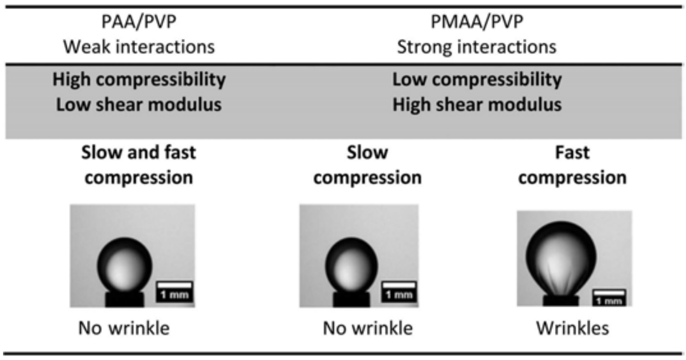

Figure 2.13: Effect of interlayer interactions on the shape of the compressed interface: wrinkles appear for fast compression of PMAA/PVP because of the hydrophobic interactions. Figure from Le Tirilly *et al.* [21].

They interpret these observations as follows: the elastic properties comes from the interactions between the layers of PMAA and PVP, and not from the layers themselves. Moreover, the interaction between PVP and PMAA is significantly stronger than the interaction between PVP and PAA, leading to very high moduli.

2.2.3 Effect of anchoring energy

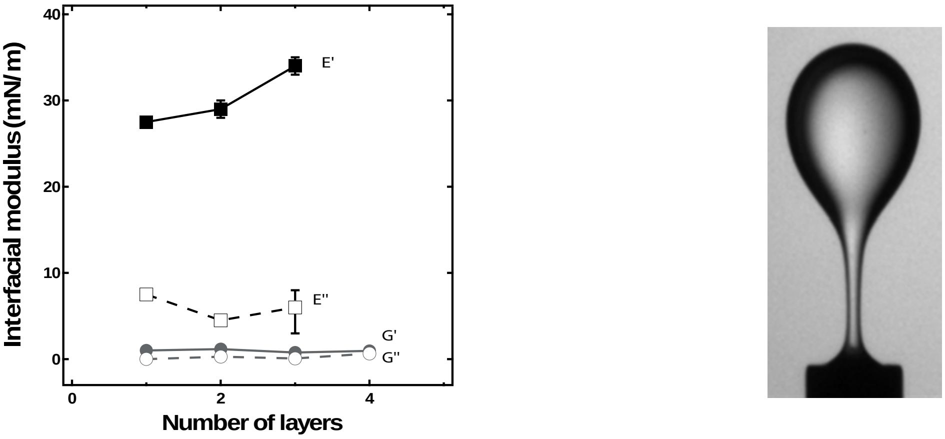

(a)

(b)

Figure 2.14: (a) Elastic moduli of grafted mutilayers on dodecane/water interface (PAA-1-C_{12}, PAA-1-C_{12}/PVP, PAA-1-C_{12}/PVP/PAA, PAA-1-C_{12}/PVP/PAA/PVP). The shear moduli G' and G'' are low because of the weak interaction between the PAA backbone of PAA-1-C_{12} and PVP. In the same time, the bilayer shows a high elastic compression modulus due to the strong interaction of the grafts of PAA-1-C_{12} with the interface. Angular frequency is $\omega = 0.6\,\mathrm{rad/s}$. (b) Dodecane droplet with PAA-1-C_{12}/PVP/PAA multilayer upon compression. Needle diameter is 1.2 mm. Figures from Le Tirilly *et al.* [85].

The authors also showed [85] that grafted multilayer PAA-1-C_{12}/PVP shows weak shear modulus, according to the PAA backbone of PAA-1-C_{12}, as illustrated in Figure 2.14. In the contrary, a high compression modulus is measured due to the strong anchoring of PAA-1-C_{12} at the interface. The anchoring leads indeed to limited desorption and rearrangements, and thus to high compression modulus.

In the frame of a PhD thesis performed in our group, Le Tirilly *et al.* have shown the advantages of the systems PAA/PVP and PMAA/PVP to build multilayers at oil/water interfaces: solubility in water, strong interactions, etc. They highlighted the possibilities offered by the hydrophobically-modified PAA when used as a first layer. They have shown that the key parameters to control the multilayers mechanical properties are the anchoring energy with the interface and the interaction between the layers.

Based on these results, we decided to study more specifically the adsorption dynamics and the rheology of the first layer for various kinds of grafting, and then to rationalize the compression of multilayers in the pendant-drop geometry. Unlike this previous work, in our study our polymers will be adsorbed at an air/water interface.

To summarize this section:

Previous studies showed that the behaviours of multilayers at dodecane/water interface strongly depend on the nature of the polymers. PVP/PMAA exhibits high shear modulus whereas PVP/PAA only exhibits dilational modulus, which allowed the authors to highlight the importance of the interaction between the layers.

They also worked with hydrophobically-modified PAA: PAA-1-C_{12}. Comparison of PAA-1-C_{12}/PVP and PAA/PVP showed that anchoring energy at the interface increases the dilational modulus of the multilayers.

2.3 Adsorption dynamics of the monolayers

The work of Le Tirilly *et al.* highlighted the importance in multilayers of the first layer and of its anchoring energy. Moreover they presented the benefits of using hydrophobically-modified polymers as a first layer. As it is the main lever to control the amount of polymer at the interface, we focus in this section on the adsorption dynamics of such polymers at an air/water interface.

To monitor the adsorption dynamics of the monolayers, we measure their interfacial tension as a function of time. Interfacial tension is indeed a measurement of surface excess according to Equation (1.125) established by Daoud *et al.* [73] for a quasi-brush. In our case, the factor Z_{B} in Equation (1.125) becomes $\frac{1}{\alpha}$, where α is the grafting degree. Accordingly, Equation (1.125) becomes:

$$\gamma = \gamma_0 - \Pi = \gamma_0 - k_{\mathrm{B}} T \alpha N \Gamma_{\text{chains}} \quad , \tag{2.5}$$

where γ is the interfacial tension, γ_0 the interfacial tension of the interface with no polymer, N the number of repeated unit per chain, and Γ_{chains} the surface excess (number of chains per unit area).

2.3.1 Experimental observations

The interfacial tension of the air bubble in the polymer solution is recorded as a function of time, and presented in Figure 2.15a. We observe that interfacial tension decreases over time, meaning that surface excess increases.

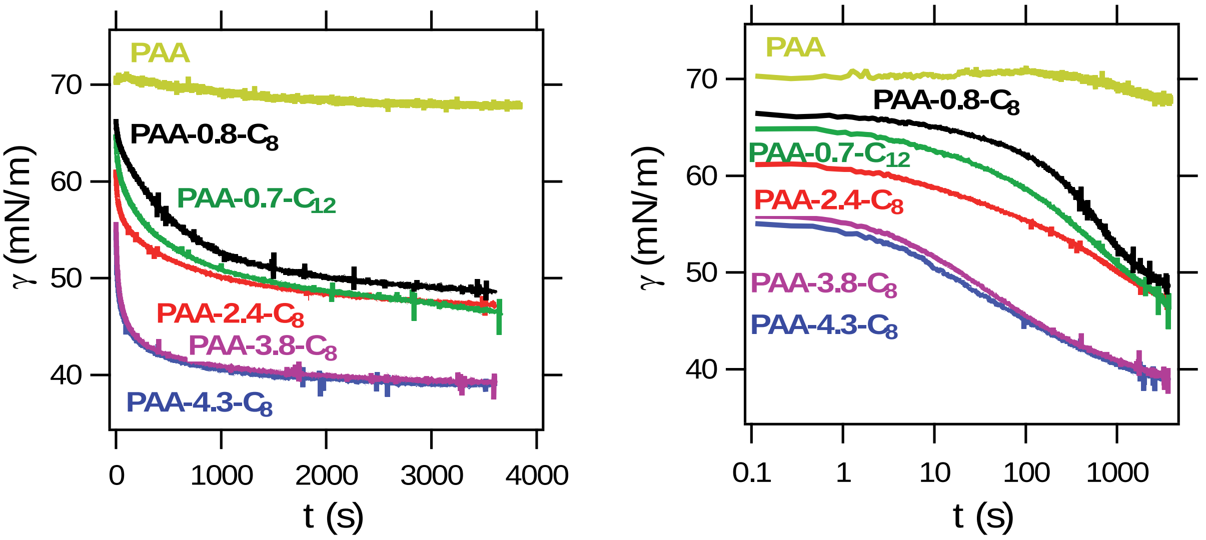

(a) Adsorption as a function of time in linear scale: the process is very fast at the beginning and slows down with time.

(b) Adsorption as a function of time in logarithmic scale: after a time lag, adsorption follows a logarithmic decay, and then eventually slows down.

Figure 2.15: Interfacial tension versus time during the polymers adsorption on an air bubble. Adsorption of polymer induces a decrease of interfacial tension. Non-grafted PAA (yellow) poorly adsorbs, while all the grafted chains show significant adsorption, which slows down with time. The adsorption increases with the grafting density and the length of the grafts.

Effect of grafting: PAA vs PAA-α-C$_n$. Interfacial tension between air and a solution of PAA (yellow in Figure 2.15a) is very close to the interfacial tension of water ($\gamma_0 = 72\,\mathrm{mN/m}$), which means that the surface pressure is small and thus that there is a small quantity of polymer adsorbed at the interface.

For the grafted polymers PAA-α-C$_n$, interfacial tension decreases faster and to a larger extent than for non-grafted PAA: the grafts enable to increase and speed up the adsorption process. All interfacial tensions were lower than 66 mN/m, because of the few seconds needed to create the bubble. After a time lag of the order of 10 s, adsorption dynamics becomes logarithmic, as shown in Figure 2.15b in a semilog scale.

Effect of grafting density and graft length. Interfacial tension of the PAA-3.8-C$_8$ and PAA-4.3-C$_8$ solutions are significantly lower than the ones of PAA-2.4-C$_8$ and PAA-0.8-C$_8$. For a constant graft length ($n = 8$), an increase of the grafting density enhances the adsorption. Moreover, interfacial tension of the PAA-0.8-C$_8$ solution is higher than for PAA-0.7-C$_{12}$. This means that the length of the grafts also increases the adsorption.

2.3.2 Model

As explained in Section 1.3.4, a logarithmic adsorption dynamics can be explained by the fact that the adsorption is limited by an energetic barrier which grows over time, as surface excess increases. In Section 1.3.4 we presented three different models from litterature, which lead to logarithmic adsorption dynamics:

- a model for diblock copolymers by Johner and Joanny [78]
- a model for end-functionnalized polymers by Ligoure and Leibler [79]
- a model for non-deformable molecules by Ward and Tordai [36].

2.3.2.a Limitations of the existing models

In Figure 2.16, we plot our experimental results as well as the prediction of Johner and Joanny for the brush regime (described respectively by Equations (1.126) and (1.127)), the prediction of Ward and Tordaï (Equation (1.132)), and the one of Ligoure and Leibler (Equation (1.130)).

First we notice that the model of Ligoure and Leibler does not describe satisfactorily our data. Second, Equation (1.127) of Johner and Joanny's model fits well the logarithmic decay of our interfacial tension data, but the time constant extracted from the fit varies over several orders of magnitudes, as presented in Figure 2.17a. Moreover according to the authors, the second equation of the model, the diffusive Equation(1.126), can only be used when surface pressure is lower than 3 mN/m, while in our case, the surface pressure is equal to $10 - 15\,\mathrm{mN/m}$ even at short times.

In fact, the architecture of our molecules, where the hydrophobic grafts are randomly distributed on our PAA backbones, is quite different from the diblocks studied by Joanny/Johner and the end-functionnalized polymers used by Ligoure/Leibler, which may explain why the model does not fit our data. We suggest that in our case the adsorbed chains are less stretched in the brush than in

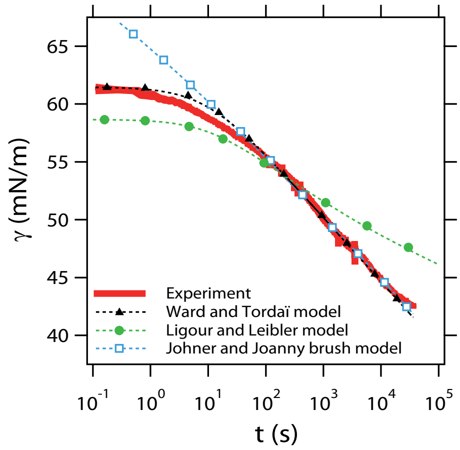

Figure 2.16: Interfacial tension versus time during adsorption. Comparison of the three models with the experimental data for PAA-2.4-C$_8$: the model described by Johner and Joanny for the brush adsorption, the model of Ligoure and Leibler, and the model of Ward and Tordaï modified for polymers. Ligoure and Leibler's model do not fit with our data. Johner and Joanny's model describe correctly the asymptotic behaviour. Ward and Tordaï model can correctly fit our data.

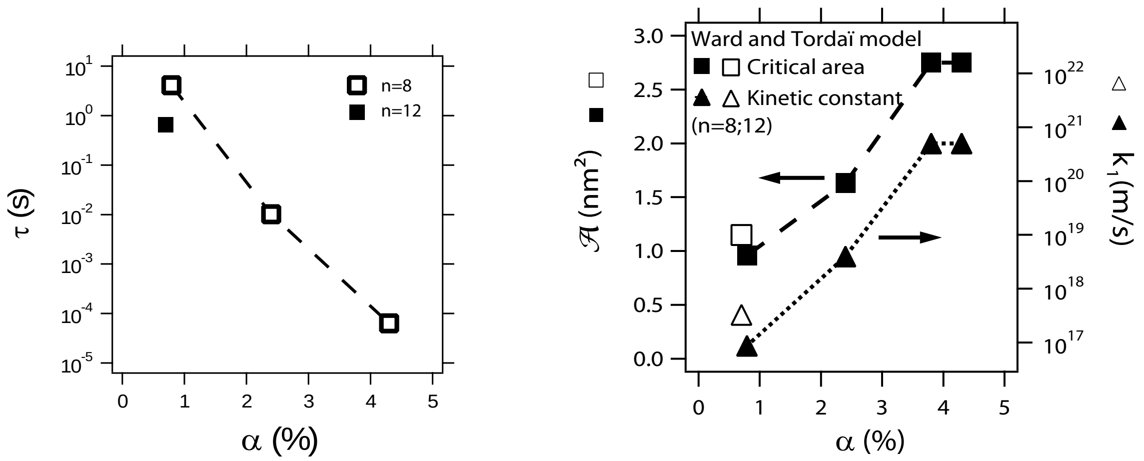

(a) Value of the fitting parameter in the model of Johner and Joanny in the kinetically limited case. The time constant varies over several orders of magnitudes.

(b) Values of the fitting parameters using the classical Ward and Tordaï model versus the grafting density α. This model gives a regular trend for the parameters, but the kinetic constant varies over 4 orders of magnitude when it is supposed to be roughly constant.

Figure 2.17: Value of the parameters extracted from fit of the experiments the Johner and Joanny model (a), and with the Ward and Tordai model (b). In both cases, the constants vary over several orders of magnitudes.

the case of diblocks or end-functionnalized polymers. We therefore come back to a model which is not specific to polymers: the energy barrier may then come from the adsorbing chains having to find a hole in the brush to reach the interface as in the Ward and Tordaï model.

To fit our data with the Ward and Tordaï model, we neglect the desorption term in the right hand side of the Equation (1.132) leading to Equation (2.6), which is consistent with a logarithmic adsorption far from saturation:

$$\frac{\mathrm{d}\,\Gamma_{\text{chains}}}{\mathrm{d}\,t} = k_1 \cdot C_0 \cdot \exp\left(-\frac{E_{\mathrm{W-T}}}{k_{\mathrm{B}}T}\right) \quad , \tag{2.6}$$

where Γ is the surface excess, k_1 the adsorption kinetic constant (corresponding to k_{ads} in Equation (1.132)), C_0 the bulk concentration and $E_{\mathrm{W-T}}$ the energy barrier that molecules need to overcome in order to adsorb. T and k_{B} are respectively the temperature and the Boltzmann constant.

The Ward and Tordaï model can describe well our data. From the fit shown in Figure 2.16, we obtain two parameters, the critical area $\mathcal{A}$ (the area to be cleared in order to adsorb a new molecule) and the kinetic constant k_1 shown in Figure 2.17b as a function of α, the grafting density of the polymers.

Surprisingly, we find that $\mathcal{A}$ is lower than the area predicted by the hydrodynamic radius of the chains (gel permeation chromatography for chains with no grafts indicates $R_{\mathrm{H}} = 10\,\mathrm{nm}$) and increases from 1 to $2\,\mathrm{nm}^2$ with the grafting density, and that k_1 increases over several orders of magnitude with the grafting density α although it is expected to be constant and determined by the hydrodynamic radius of an adsorbing polymer coil.

These conclusions motivate us to refine the Ward and Tordai model.

2.3.2.b Energy barriers to be considered

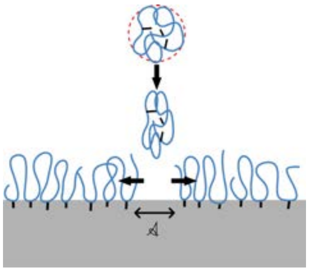

Figure 2.18: Experiments show that there are two energy barriers to consider: the cleaning of the interface, and the deformation of the incoming molecules.

To account for these results, we suggest that the adsorbing coils have to stretch to enter the hole created through the brush (Figure 2.18): this description is actually a combination of the Johner and Joanny approach and the Ward and Tordai one. This description explains why $\mathcal{A}$ is smaller than the section of non-deformed polymer coils. The stretching of the chains should create a second energy barrier which was not taken into account yet in the Ward and Tordai model, explaining why k_1, the apparent kinetic constant, varies strongly with grafting density α. The deformation energy corresponding to a chain of radius $R_{\mathrm{F}} = b \cdot N^{3/5}$ (b being the size of a repeated unit, and N their number) entering a pore of cross section $\mathcal{A}$ (diameter $= 2\sqrt{\mathcal{A}/\pi}$), was predicted by Colby and Rubinstein [62]:

$$E_{\text{def}} = k_{\mathrm{B}}T \cdot \left(\frac{R_{\mathrm{F}}}{D}\right)^{5/3} = k_{\mathrm{B}}T \left(\frac{\sqrt{\pi}}{2}\right)^{5/3} \cdot N \cdot \left(\frac{b^2}{\mathcal{A}}\right)^{5/6} \quad . \tag{2.7}$$

Thus we rewrite the adsorption constant k_1 as follows:

$$k_1 = k_1' \cdot \mathrm{e}^{-E_{\mathrm{def}}/k_{\mathrm{B}}T} \quad , \tag{2.8}$$

where

$$k_1' = \frac{R_{\mathrm{F}}}{\tau_0} = \frac{k_{\mathrm{B}}T\, N^{3/5}}{6\,\pi\eta\, b^2} \quad , \tag{2.9}$$

where $\tau_0 = \frac{b^2}{D} = \frac{6\,\pi\,\eta\, b^3}{k_{\mathrm{B}}T}$ is defined as the time for a molecule to diffuse over its own size, and D is a diffusion constant $D = \frac{k_{\mathrm{B}}T}{6\,\pi\,\eta\, b}$ [86], where η is the viscosity of the solvent. This constant k_1' represent the number of possible adsorption events per unit time and per unit area, divided by the number of molecules in the corresponding volume.

2.3.2.c Theoretical evolution of interfacial tension

Using Equations (2.7), (2.8) and (2.9), Equation (2.6) becomes:

$$\frac{\mathrm{d}\,\Gamma_{\mathrm{chains}}}{\mathrm{d}\,t} = C_0 \cdot k_1' \cdot \mathrm{e}^{-\frac{\Pi\cdot\mathcal{A}+E_{\mathrm{def}}}{k_{\mathrm{B}}T}} \quad . \tag{2.10}$$

This equation, coupled with Equation (2.5), leads to a logarithmic dependency of the interfacial tension versus time:

$$\gamma = \gamma_{\mathrm{t=0}} - \frac{k_{\mathrm{B}}T}{\mathcal{A}} \cdot \ln\left(1 + \alpha N \mathcal{A} k_1' C_0 \cdot t \cdot \exp\left(-\frac{\mathcal{A}\Pi_{\mathrm{t=0}} + E_{\mathrm{def}}}{k_{\mathrm{B}}T}\right)\right) \quad . \tag{2.11}$$

This equation, when fully developed, is written:

$$\gamma = \gamma_{\mathrm{t=0}} - \frac{k_{\mathrm{B}}T}{\mathcal{A}} \cdot \ln\left(1 + \alpha N \mathcal{A} \cdot \frac{k_{\mathrm{B}}T\, N^{3/5}}{6\,\pi\eta\, b^2} \cdot C_0 \cdot t \cdot \mathrm{e}^{-\frac{\mathcal{A}\cdot(\gamma_0 - \gamma_{\mathrm{t=0}}) + k_{\mathrm{B}}T\left(\frac{\sqrt{\pi}}{2}\right)^{5/3} \cdot N \cdot \left(\frac{b^2}{\mathcal{A}}\right)^{5/6}}{k_{\mathrm{B}}T}}\right) \quad . \tag{2.12}$$

2.3.3 Comparison of the model with the data

Equation (2.12) was used to fit our data, with $\mathcal{A}$ and b as fitting parameters (respectively the critical area for adsorption and the size of a monomer). The initial tension $\gamma(t = 0)$ is obtained from experiments. This model yields curves with the same shape as the Ward and Tordai model, only the parameters to describe it differs. In Figure 2.16, we show that this modified version of the Ward and Tordai model fits our data very well over the whole time scale i.e. both the lag time and model and the logarithmic decay for the PAA-2.4-C$_8$. In Figure 2.19 we present the values of the fitting parameters $\mathcal{A}$ and b obtained from the fits for the series of grafted polymers used in this study.

We find that the monomer size b is of the order of 1.5Å and does not depend on α, which is expected. The area $\mathcal{A}$ increases from 1 to 2 nm with the percentage of grafts α on the polymers. We interpret this result as follow: the chains adsorb with all the grafts oriented toward the interface, so the more grafts there are on the molecules, the more space is needed, as sketched in Figure 2.20a. The slope of the curve, $\mathcal{A}(\alpha)$, corresponds to an area of 5.8Å^2 per graft, which is of the expected order of the size of a graft [87]. Indeed when one graft is added on the molecule, a zone corresponding to a graft has to be cleared on the interface.

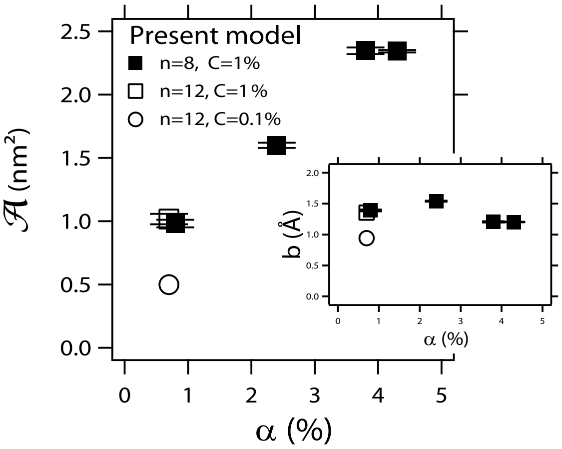

Figure 2.19: Values of the fitting parameters using the modified Ward and Tordaï model: the critical area to clean to adsorb a new molecule is increasing with the grafts density α, with a slope of $0.39\,\mathrm{nm}^2$ for 1%, which means 5.8Å^2 per graft. In the same time, the size of the monomer is roughly constant.

2.3.4 Discussion

Millet *et al.* [76] studied experimentally the adsorption kinetics of the same PAA-α-$\mathrm{C_n}$ polymers at high pH, where the chains are fully charged. They observed a logarithmic decay of the interfacial tension but unlike in our case, they found that the kinetics does not depend on the number of grafts on the chains. They concluded from their data that the adsorption is limited by the adsorption dynamics of the first graft (Figure 2.20b). We suggest that in their case the adsorbed charged chains form a more extended and stretched brush because of the osmotic pressure of the counter-ions and that the adsorbing charged chains are strongly repelled by the similarly charged brush. Consequently the adsorbing charged chains stretch much more strongly when they approach the interface and are only able to adsorb one hydrophobic graft at a time.

In our case, as the chains are neutral, it is likely that a larger number of grafts can adsorb simultaneously at the interface. Therefore, the more grafted the chains, the larger the area $\mathcal{A}$ to free. This is why the interfacial tension decreases faster for highly grafted chains, even if the energetic barrier is greater.

The adsorption dynamics of our grafted polymers can not be described by the classical adsorption models. When a chain approaches the interface, it encounters the brush made of the adsorbed chains. We showed that the energy barrier for the adsorption consists of two contributions: the clearing of a portion of the crowded interface and the deformation of the incoming chain to fit in this portion of interface. The area of this portion and thus the adsorption dynamics is a function of the grafting degree.

We are now able to control the amount of polymer at the interface. We need to understand the robustness of these monolayers. We focus here more specifically on the behaviour of these interfaces upon compression and dilatation.

(a) Our results suggest that the number of adsorbing grafts is proportional to the number of grafts on the molecule, on the contrary to the observation of F. Millet for charged molecules.

(b) Interpretation of Millet for fully charged chains leading to repulsive interaction between the brush and the adsorbing chains.

Figure 2.20: The dynamics of adsorption of the polymers strongly depends on the charge of the chains.

To summarize this section:

The grafting strongly modifies the dynamics of adsorption: grafted chains PAA-α-C$_\mathrm{n}$ adsorb faster and to a larger extent than non-grafted PAA. The adsorption of grafted polymers follows a logarithmic decay due to an energetic barrier for adsorption. The energetic barrier is the result of the clearing of a portion of interface to adsorb a new molecule, and the deformation of the chain to fit in this portion of interface of area $\mathcal{A}$. This area increases with the degree of grafting α, what can be interpreted as a simultaneous adsorption of all the grafts of a polymer molecule at the same time.

2.4 Compression/Dilatation of the monolayers

In this section we want to study the stability of monolayers of hydrophobically-modified polymer at the interface. More precisely, we investigate the adsorption/desorption processes triggered by the deformation of the interface.

To probe the behaviour of the polymer layers under compression/dilatation we deflate/inflate a rising bubble and we record the area and the interfacial tension through the two methods presented in Section 2.1.2.b. Deformation ϵ is defined as the relative change in surface area:

$$\epsilon = \frac{A_\mathrm{i} - A}{A_\mathrm{i}} \quad , \tag{2.13}$$

where A_i is the initial area, and A the area at time t. Therefore, deformation is positive ($\epsilon > 0$) for compressions, and negative ($\epsilon < 0$) for dilatations.

2.4.1 Compression

We plot in Figure 2.21 the interfacial tension versus deformation for slow compressions of various monolayers of PAA and PAA-α-C$_\mathrm{n}$.

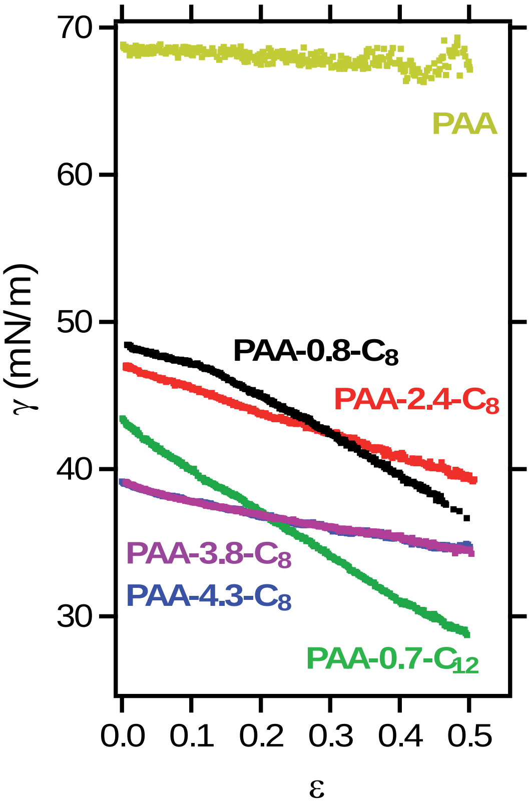

Figure 2.21: Evolution of the interfacial tension during compression. The interfacial tension decrease during a compression because of the accumulation of polymer on the interface. The interfacial tension at zero compression depends on the adsorption process.

We observe in Figure 2.21 that the interfacial tension for grafted polymers decreases during a compression meaning that the polymer surface excess increases, whereas the interfacial tension for non-grafted PAA show no significant variation.

In the situation where the chains and the trains do not desorb upon compression, we can easily estimate the surface excess (in terms of repeated units) as a function of deformation. Indeed the number of adsorbed unit, ΓA remains constant and is equal to the initial number of adsorbed chains $\Gamma_\mathrm{i} A_0$. We can then easily predict the evolution of the theoretical surface excess, $\Gamma_{\text{no desorption}}$, as a function of the initial surface excess, Γ_i, and the deformation ϵ:

$$\Gamma_{\text{no desorption}} = \frac{\Gamma_\mathrm{i} A_0}{A} = \Gamma_\mathrm{i} \cdot \frac{A_\mathrm{i}}{A} = \Gamma_\mathrm{i} \cdot \frac{1}{1-\epsilon} \quad . \tag{2.14}$$

Without desorption, and according to Equation (2.5) which was derived for polymers adsorbed in a quasi-brush, the interfacial tension γ is related to the initial interfacial tension γ_i according to the following equation:

$$\gamma_{\text{no desorption}} = \gamma_0 - (\gamma_0 - \gamma_\mathrm{i}) \cdot \frac{A_0}{A} = \gamma_0 - \frac{\gamma_0 - \gamma_\mathrm{i}}{1-\epsilon} \quad . \tag{2.15}$$

$\gamma_{\text{no desorption}}$ can also be written:

$$\gamma_{\text{no desorption}} = \gamma_0 - \Pi_{\text{no desorption}} \quad , \tag{2.16}$$

with

$$\Pi_{\text{no desorption}} = \frac{\gamma_0 - \gamma_\mathrm{i}}{1-\epsilon} \quad , \tag{2.17}$$

which is the surface pressure obtained if no chain desorption occurs.

In Figure 2.22 we plot the measured interfacial tension γ as a function $\Pi_{\text{no desorption}}$ defined by Equation (2.17). The dashed line predicts the interfacial tension in the case where the chains do not desorb. Any desorption will lead to a higher interfacial tension and will be above the dashed line.

The compression curves of PAA-0.8-C_8 and PAA-0.7-C_{12} in Figure 2.22b present two regimes. At low compression, the interfacial tension superimposes well with the red dashed line, which means that there is no desorption in this regime. In the second regime, the interfacial tension remains on a plateau above the dashed line meaning that desorption or partial desorption of molecules occurs and that the surface excess remains constant.

Effect of speed: two compression speed are compared: slow ($\dot{\epsilon} \simeq 7 \cdot 10^{-3}\,\mathrm{s}^{-1}$) and fast ($\dot{\epsilon} \simeq 1 \cdot 10^{-1}\,\mathrm{s}^{-1}$) compressions. For a faster compression of the PAA-0.7-C_{12} layers the desorption occurs later and the transition between the two regimes is sharper. The driving force of the desorption is the increase of the chemical potential of the chains in the brush and the rate of desorption is limited by the anchoring energy of the chains at the interface. For a given anchoring energy, we expect that at higher compression speed, less monomers will have time to desorb.

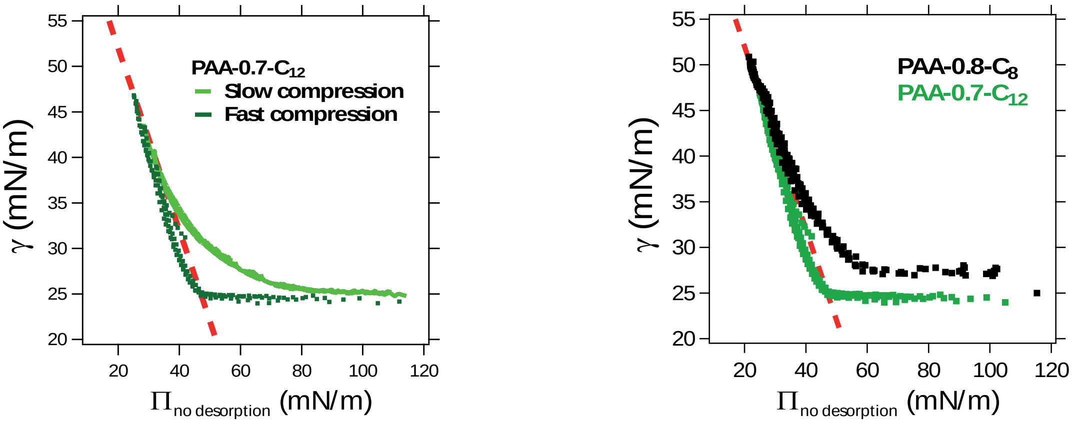

(a) Compression of PAA-0.7-C_{12} at two compression rates. Fast compression delays the desorption.

(b) Compression of monolayers for different length of grafts (fast compression). Shorter grafts lead to earlier desorption.

Figure 2.22: Representation of the compression: the interfacial tension is plotted versus the surface pressure which would be measured without desorption, which means with a constant quantity of polymer at the interface. Without desorption, the interfacial tension would follow the red dashed line. Polymer desorption leads to higher interfacial tension, above the dashed line.

Effect of graft size: in Figure 2.22b we compare the compression behaviour of the PAA grafted with C_8 and C_{12} chains within similar proportions. During the compression the interfacial tension remains higher for smaller grafts. This means that desorption occurs earlier for shorter grafts which is consistent with the fact that they have a lower anchoring energy.

Effect of grafting degree: in Figure 2.23 we study the influence of the degree of grafting on the compression behavior for the PAA-α-C_8 chains. We observe that the more grafted the chains are, the lower the initial interfacial tension. This is expected because more grafted chains have higher affinity with the interface, as detailed in Section 2.3. However surprisingly for the more grafted chains, the interfacial tension obtained at large compressions is higher than the one obtained for less grafted chains. Desorption seems to be easier for the more grafted chains.

To rationalize the results obtained for polymers with different grafting degrees shown in Figure 2.23, we define the following dimensionless numbers: the relative change in surface pressure, $\overline{\Delta\Pi}$, and the compression parameter $\overline{\epsilon}$ defined by

$$\overline{\Delta\Pi} = \frac{\Pi - \Pi_\mathrm{i}}{\Pi_\mathrm{i}} \quad , \tag{2.18}$$

and

$$\overline{\epsilon} = \frac{1}{1-\epsilon} - 1 = \frac{A_0 - A}{A} \quad . \tag{2.19}$$

The compression parameter $\overline{\epsilon}$ increases during compression starting from zero.

If there is no polymer desorption, using Equation (2.17), the relative change in surface pressure is

$$\overline{\Delta\Pi} = \frac{\Pi_\mathrm{i} \cdot \frac{1}{1-\epsilon} - \Pi_\mathrm{i}}{\Pi_\mathrm{i}} = \overline{\epsilon} \quad . \tag{2.20}$$

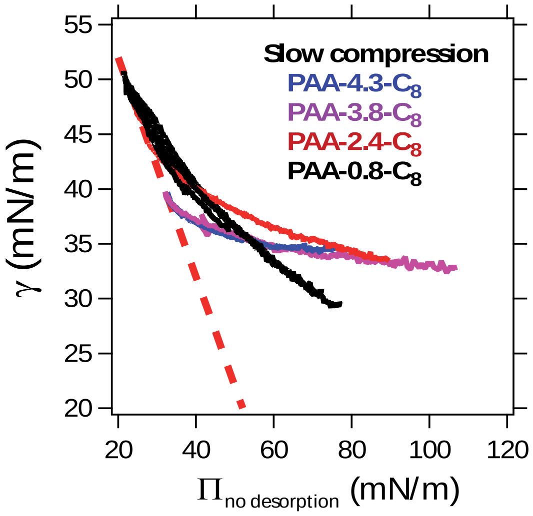

Figure 2.23: Compression of monolayer for different grafting densities. The red dashed line represent the theoretical tension in the quasi-brush regime if there is no desorption. The deviation from this line shows the desorption of the chains from the interface. The more grafted chains (PAA-4.3-C_8 and PAA-3.8-C_8, in pink and blue) desorb faster.

In Figure 2.24, we plot the relative change in surface pressure versus the compression parameter $\bar{\epsilon}$ for slow compression of polymer PAA-α-C_8, for different grafting densities. The red dashed line represents the theoretical case with no desorption described by Equation (2.20). We find that $\overline{\Delta\Pi} < \bar{\epsilon}$. The more grafted the chains are, the stronger is the deviation from Equation (2.20), which means that the desorption of polymer chains is stronger. Surprisingly, grafting seems to favour the chains desorption.

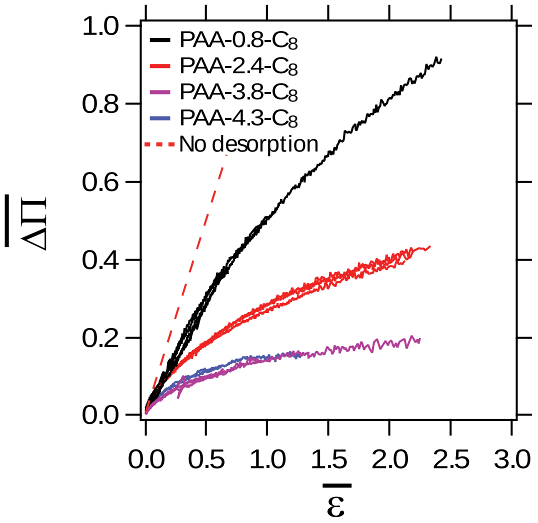

Figure 2.24: The variation of surface pressure due to compression increases with compression, and stay lower than what is predicted if no desorption. The more grafted the chains are, the faster is the deviation from the prediction in the case where there is no desorption.

We suggest the following interpretation: these pseudo brushes are known to present adsorbed grafts and stretched loops. As a consequence, the quantity of graft directly determines the length of the loops, and hence the thickness of the brush, as illustrated in Figure 2.25. For the same amount of polymer per unit area, the more grafted chains are concentrated in a thinner layer, and therefore are more concentrated in volume, creating an osmotic pressure which leads to a faster desorption.

(a) Poorly grafted chains result in thick polymer layer.

(b) More grafted chains result in thin dense polymer layer.

Figure 2.25: Effect of grafting density α on layer density according to compression results.

2.4.2 Dilatation

It is also possible to inflate bubbles and probe their dilational behaviours. Interfacial tension increases during dilatation, as shown in Figure 2.26, which means that surface excess decreases owing to the increase of area.

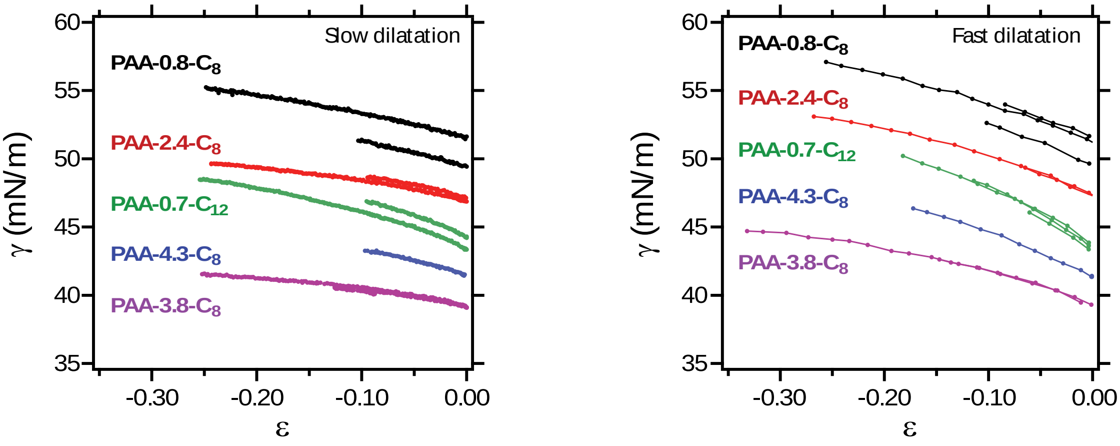

(a) Slow dilatation.

(b) Fast dilatation.

Figure 2.26: Interfacial tension as a function of deformation during dilatation of the monolayers.

We compare in Figure 2.27 the measured interfacial tension with the theoretical prediction in the case where no adsorption and no desorption occurs. In some cases, we observe a slight adsorption taking place during dilatation, leading the interfacial tension to be a bit lower than expected. Nevertheless in most cases, during dilatation the interfacial tension is equal to the predicted one, which means that chains from the bulk solution do not have time to adsorb, according to the slow adsorbtion dynamics presented in Section 2.3.

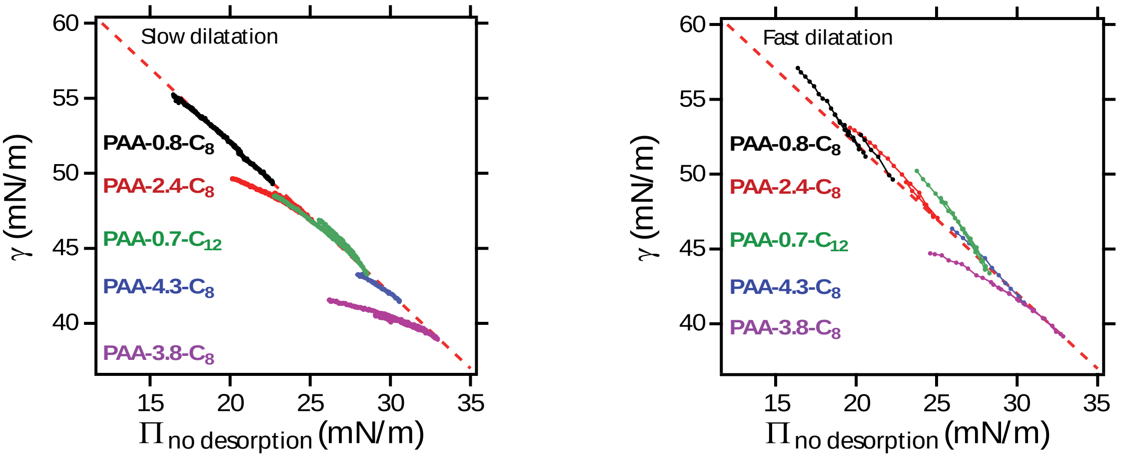

(a) Slow dilatation.

(b) Fast dilatation.

Figure 2.27: Dilatation of monolayers: interfacial tension versus surface pressure if no desorption occurs (and also no adsorption). Interfacial tension increases during dilatation because an increase of the area decreases the surface excess. Moreover, most of the measurements are in good agreement with the prediction of no further adsorption and desorption (red dashed line). On the contrary, PAA-2.4-C_8 (red) and PAA-3.8-C_8 (pink) shows some adsorption during the dilatation.

Compression of PAA-α-C_n monolayers yields desorption of the polymers. We showed that this desorption can be limited by increasing the deformation speed, the length of the grafts, or by decreasing the grafting density. Accordingly, among our different grafted polymers, PAA-0.7-C_{12} seems to be the best basis to grow multilayers on.

We study now the effect of the interactions between the layers and of the anchoring energy on the rheological properties of multilayers.

To summarize this section:

Compression of monolayers results in an accumulation of polymer at the interface, and consequently in a decrease of interfacial tension. This decrease is limited by the polymer desorption. This desorption can be limited by increasing the size of the grafts. An increase of the grafting density results in denser polymer layers which desorb more easily. During dilatation, no significant adsorption/desorption is observed.

2.5 Pendant-drop measurements on multilayers

We assemble multilayers of polymers at air/water interface in order to measure the rheological properties of such assemblies. To this aim, we follow the protocol described in Section 2.1. Rheological properties are measured using three geometries: a pendant-drop apparatus, a radial trough, and an interfacial shear rheometer. In this section we present the results of pendant-drop experiments. Radial-trough and interfacial shear rheometer measurements will be presented in Section 2.6.

Pendant-drop experiments were conducted combining the two measurements presented in Section 2.1: the Laplacian fit and the pressure measurement. We investigate here the link between molecular interactions and rheological response of the multilayers, first with two layers only (bilayers), and then with more layers.

2.5.1 Influence of grafting of the first layer

Two bilayers are compared to observe influence of grafting: PVP/PAA (no grafts), and PAA-0.7-C_{12}/PVP (hydrophobic grafts in the first layer). Interfacial tension during compression is shown in Figure 2.28 for these two bilayers. The polymer which shows higher surface pressure as a monolayer is chosen to be adsorbed first: PAA-0.7-C_{12} > PVP > PAA. In Figure 2.28, dashed line represents interfacial tension calculated under homogeneous and isotropic assumptions, while solid line represents interfacial tension extracted from pressure measurements. For each system, the two methods presented in Section 2.1.2.b yield the same interfacial tension value. This implies that interfacial tension is homomgeneous and isotropic.

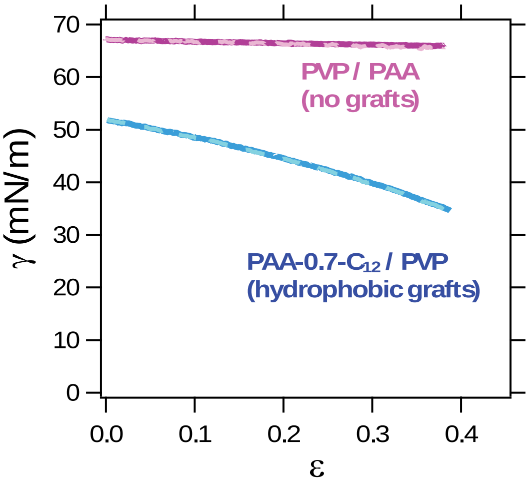

Figure 2.28: Interfacial tension during compression of bilayers, without and with grafts (respectively pink and blue curves). In both cases, both methods agree, meaning that interface is liquid (no elasticity).

PVP/PAA shows high interfacial tension, which means low surface pressure and thus low surface excess. We should note that we measure the same interfacial tension for PAA/PVP. Moreover, interfacial tension is constant during compression. This means that surface excess is constant, and therefore that desorption and rearrangements occur as fast as compression, as for the case of soluble surfactants. On the contrary, for PAA-0.7-C_{12}/PVP, the interfacial tension is lower, and decreases during compression: there is a higher surface excess, which increases during compression. This means that grafts enable to slow down desorption and rearrangements.

Increasing anchoring energy with the interface is thus a way to adjust the rheological properties of the multilayers.

2.5.2 Role of the interactions between the polymer layers

We now compare the PVP/PAA system (where the polymer chains bind only though hydrogen bonds) with the PVP/PMAA system where the polymer chains interact through hydrogen bonds and hydrophobic interactions. Interfacial tension versus deformation for these two bilayers is presented in Figure 2.29.

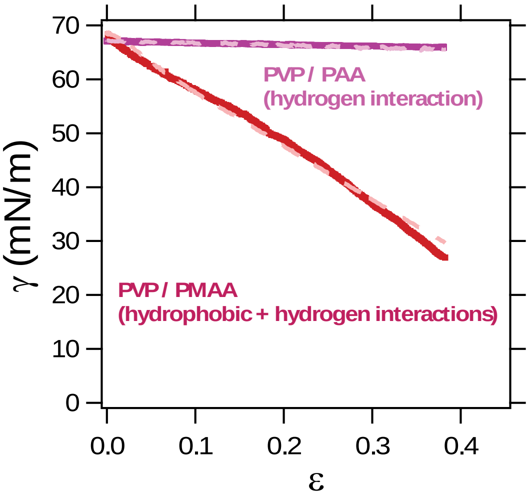

Figure 2.29: Interfacial tension during compression of bilayers with different interlayer interaction.

Comparison of the two interfacial tension measurement methods indicates that interfacial tension for PVP/PMAA is also homogeneous and isotropic. Moreover, we observe that interfacial tension decreases during compression, unlike the PVP/PAA bilayer. Therefore when the polymer chains interacts through an interplay of hydrogen bonds and hydrophobic interactions, trains desorption and rearrangements of the chains inside the layer are probably limited, which leads to an increase of the surface excess during compression. The slopes of the curves in Figure 2.29 give access to an interfacial modulus. We will show in Section 2.6 that it corresponds to the dilational modulus E. We measure $E_{\mathrm{PVP/PAA}} = 3\,\mathrm{mN/m}$ and $E_{\mathrm{PVP/PMAA}} = 100\,\mathrm{mN/m}$.

2.5.3 Combination of a high anchoring energy and strong inter-layer interactions

We found before that interlayer interaction and grafting energy are two control parameters that tune rheological properties of bilayers. We study here the behaviour of the PAA-0.7-C_{12}/PVP/PMAA system which combines a high anchoring energy and strong interaction in the following layers. We compare this system with another trilayer, PAA-0.7-C_{12}/PVP/PAA and also with the PAA-0.7-C_{12}/PVP bilayer.

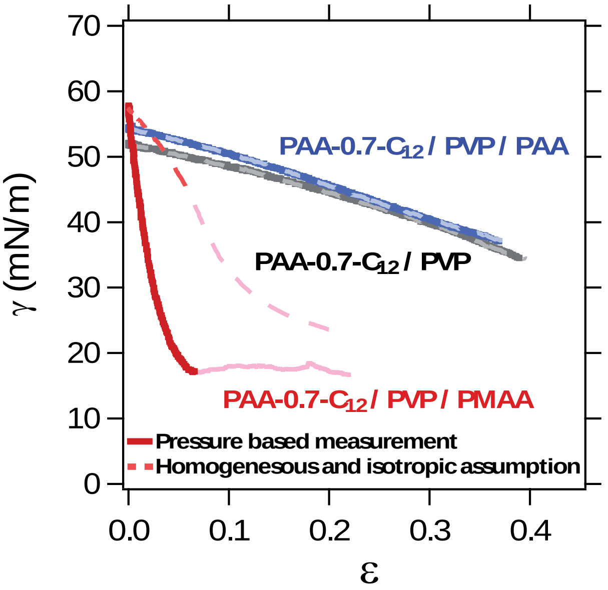

Figure 2.30: Interfacial tension during compression of three layered interfaces with different third layer, compared with the corresponding bilayer (PAA-0.7-C_{12}/PVP). Addition of PAA as a third layer does not modify the rheological properties of the multilayer (same liquid behaviour). On the contrary, addition of PMAA as a third layer drastically changes the rheological behaviour: the two methods do not concord any more, meaning that the interface is elastic. Moreover, interfacial tension decreases very fast with deformation, meaning that compression modulus is high. The slope at the origin gives a modulus of 1 200 mN/m.

A shown in Figure 2.30, there is almost no difference between PAA-0.7-C_{12}/PVP and PAA-0.7-C_{12}/PVP/PAA: interfacial tensions of the two systems are very similar. The third PAA layer seems to have poor influence on the compression behaviour of the multilayer. Moreover, the two interfacial tension measurements yield the same value, confirming the homogeneous and isotropic assumption. This indicates that the interface is still liquid, and the shape of the droplet corresponds to classical droplets shape, as shown in Figure 2.31a.

On the contrary, the PAA-0.7-C_{12}/PVP/PMAA system exhibits a different behaviour. As seen in Figure 2.30, the two interfacial tension measurements do not yield the same value any more. This means that interfacial tension can not be considered as homogeneous and isotropic: there is an elastic component in the interfacial tension. Moreover, interfacial tension decreases much more drastically than in the case of PAA-0.7-C_{12}/PVP/PAA, which means that the compression modulus is higher. The derivative of tension with respect to deformation for small deformation gives a dilational modulus $E = 1\,200\,\mathrm{mN/m}$.

A plateau is observed for deformation higher than $\epsilon = 0.06$ (faded area). According to the change in the shape of the bubble, it seems to correspond to wrinkling or buckling of the interface close to the tip of the needle. Wrinkling of the interface has indeed been observed for the bilayers on oil droplets, where the lower index mismatch allows a direct observation of the interface. An example of large deformation of bubble covered by PAA-0.7-C_{12}/PVP/PMAA is shown in Figure 2.31b: the curvature of the neck changes at small compression (second picture), leading to non-homogeneous deformations. Even if compression mostly occurs at the basis of the bubble, we expect a constant interfacial tension at the apex which is not further deformed.

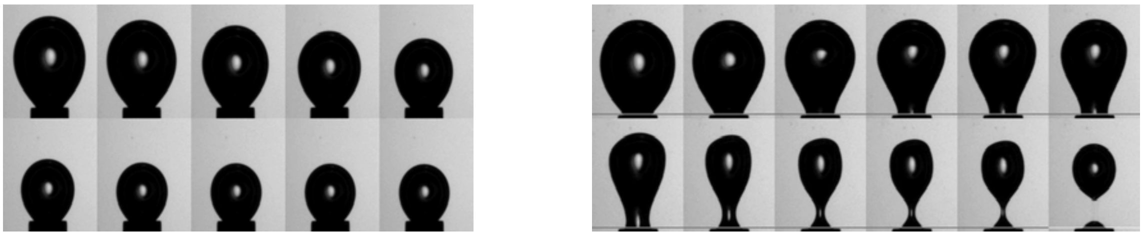

(a) PAA-0.7-C_{12}/PVP/PAA (b) PAA-0.7-C_{12}/PVP/PMAA

Figure 2.31: Compression steps of multilayers with different third layers. (a) PAA-0.7-C_{12}/PVP/PAA: classical bubble shape with liquid interface. (b) PAA-0.7-C_{12}/PVP/PMAA: large deviation from the shape in the liquid-interface case. The shape of the basis starting from the second picture ($\epsilon = 0.05$) suggests that interface is wrinkled. Last picture is after one night stand.

To check this hypothesis, we measure the variation of the radius of curvature at the apex, R_{apex}, and we relate it to the deformation of the apex as follows:

$$\epsilon_{\text{apex}} = \frac{R^2_{\text{apex},0} - R^2_{\text{apex}}}{R^2_{\text{apex},0}} \quad , \tag{2.21}$$

where $R_{\text{apex},0}$ is the radius of curvature of the apex before deformation. In the case of a homogeneous sphere under compression, ϵ_{apex} and ϵ (defined by Equation (2.13)) are strictly equivalent. In Figure 2.32 we plot ϵ_{apex} as a function of ϵ for different systems. We see that for all systems, except PAA-0.7-C_{12}/PVP/PMAA, both deformations are similar, meaning that deformation is homogeneous. On the contrary, for the PAA-0.7-C_{12}/PVP/PMAA system, for $\epsilon > 0.05$, the two deformations are not equivalent, according to the observation in Figure 2.30.

In conclusion, in Figure 2.30 for the PAA-0.7-C_{12}/PVP/PMAA system, only the part corresponding to $\epsilon < 0.05$ is relevant. For larger compression, the deformation is not homogeneous.

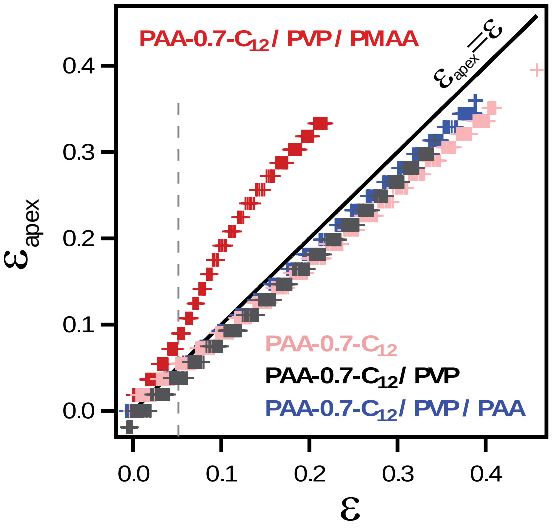

Figure 2.32: Deformation of the apex versus global deformation of the interface. Only the PAA-0.7-C_{12}/PVP/PMAA system for deformation larger than 0.05 shows significant disagreement between the two measurements. In all the other cases, deformation seems thus to be uniform.

We observed that multilayers based on PVP/PMAA shows higher moduli than other multilayers because of the strong interactions between the layers. Furthermore, the combination of high anchoring energy and strong interlayer interactions in the PAA-0.7-C_{12}/PVP/PMAA system yield a very high modulus, and complex deformation profile. We showed that in this case the deformation of the interface is not homogeneous for large compressions.

More generally for multilayers exhibiting elastic behaviours, we wonder what are the contributions of shear and of isotropic compression in the deformation. Because of the complex initial shape of the rising bubble, there is no trivial answer to this question. This raises the question of the nature of the measured moduli. To answer it, we will perform in parallel isotropic compression and pure shear deformation of PVP/PMAA in the adapted geometries: the radial trough and the shear rheometer.

To summarize this section:

Multilayers of polymers at air/water interface were compressed in pendant-drop apparatus. We showed that we can rigidify the multilayers by increasing either the anchoring at the interface (with grafts in the first polymer layer) or the interaction between the layers (by changing from PAA to PMAA to add hydrophobic interactions with PVP).

Furthermore, we showed that these two effects combined in a three-layer membrane make the membrane strongly viscoelastic.

2.6 Pure shear/compression measurements on PVP/PMAA bilayers

Despite all the advantages of the pendant-drop apparatus, the complex shape of a pendant droplet (or rising bubble) induces limitations. Compression and deformation can be non-homogeneous on the interface, as observed in Figure 2.31b. As a consequence, the measured tension is a combination of compression and shear.

Complementary experiments on PVP/PMAA bilayers at air/water interface are performed to know independently the compression and shear moduli, respectively using a radial trough and an interfacial rheometer. These experiments (interfacial rheometer and radial trough) were performed in the Soft Materials group in ETHZ, in collaboration with M. Pepicelli, B. Schroyen (from KUL), M. Nagel, and J. Vermant.

We chose PVP/PMAA as a model system to compare these three different measurement setups: the pendant-drop apparatus, the radial trough, and the interfacial rheometer. It is indeed the stiffest bilayer that we can build with our system, so we believe that it is the most susceptible to bring the different methods to disagree. This makes PVP/PMAA a good model system for this study.

2.6.1 Compression using the radial trough experiment

Using a radial trough (Figure 2.10), the interface is alternatively dilated and compressed, as presented in Figure 2.33a with a compression speed of 4.7 cm^2/min corresponding to a retraction speed of the ring of 1.5 mm/min. The corresponding isotherm (surface pressure vs area) is presented in Figure 2.33b.

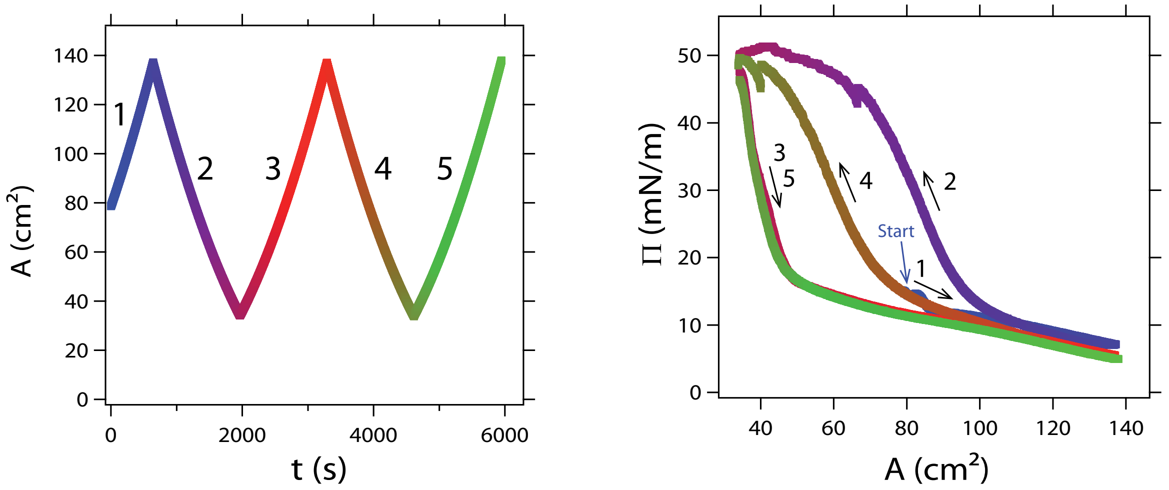

(a) Area versus time: after an initial dilatation, two full compression-dilatation cycles are performed.

(b) Isotherm: surface pressure versus area. Colour code represent time as presented in (a). Cycles are described anticlockwise.

Figure 2.33: Experiment for PVP/PMAA bilayer. (a) Area versus time. (b) Surface pressure isotherms for successive compression and dilatation cycles.

The interface is first expanded (number 1 in Figure 2.33a), then compressed (2) and expanded again (3), and then another compression/expansion cycle (4 and 5) is performed.

At high area ($A > 100\,\mathrm{cm}^2$), the surface pressure varies smoothly and the measurement is reversible. The value of the surface pressure is relatively low in this regime.

For smaller areas, we observe an hysteresis. The pressure upon compression (2 and 4) is higher than during dilatation (3 and 5). If we plot Π as a function of $\ln(A)$, we find a slope of $100\,\mathrm{mN/m}$ during the compression phases, which corresponds to the dilational modulus of this bilayer.

Hysteresis is an evidence of intermolecular attractive interactions: compression increases the contact between the molecules and thus the interaction between them. Moreover, the fact that the two compression ends reach the same surface pressure means that there is no material loss during the cycles, as explained by Theodoratou *et al.* [88].

We interpret the shift observed between the two compressions as follows: high compression of the first cycle brings into close contact the chains of PMAA and PVP, leading to irreversible complexation. This scenario is in good agreement with the interpretation of Theodoratou *et al.* [88] in a similar case. Ideally, the isotherms would have been measured as slow as possible in order to have quasi-static measurement: all the relaxation processes should be faster than the compression. In our case, such a slow compression is impossible to achieve, leading to the observed hysteresis between compression and dilatation, and between the cycles.

2.6.2 Interfacial shear rheology

Rheological measurements are performed with a double wall ring apparatus as presented in Section 1.2.4.f to measure the shear modulus of PVP/PMAA membrane at the air/water interface.

Strain sweep experiment are performed to know the linear regime, and the dynamic yield stress of the material: the angular frequency is fixed at $\omega = 1\,\mathrm{rad/s}$, and the shear strain varies from $\epsilon = 0.01\,\%$ to $\epsilon = 10\,\%$. The elastic storage and loss moduli are presented in Figure 2.34a as function of strain.

For small strain ($\epsilon < 0.1\,\%$), elastic moduli do not depend on strain: this is the linear regime. In this regime, the storage modulus, $G' = 200\,\mathrm{mN/m}$, is significantly higher than the loss modulus, $G'' = 40\,\mathrm{mN/m}$. For higher strain ($\epsilon \in [0.1,\,1]\,\%$), the storage modulus G' decreases and the loss modulus G'' increases: this is the non-linear regime. At higher strain $\epsilon > 1\,\%$, both moduli strongly decrease: the interface is damaged by the too large deformations. This is the destructive regime.

A frequency sweep has been performed at a given strain amplitude $\epsilon = 0.05\,\%$ for angular frequency ranging from $\omega = 0.1\,\mathrm{rad/s}$ to $\omega = 10\,\mathrm{rad/s}$. Moduli are presented as function of angular frequency in Figure 2.34b. The storage modulus increases whereas the loss modulus slightly decreases. Frequency has no strong influence in this range on elastic shear moduli.

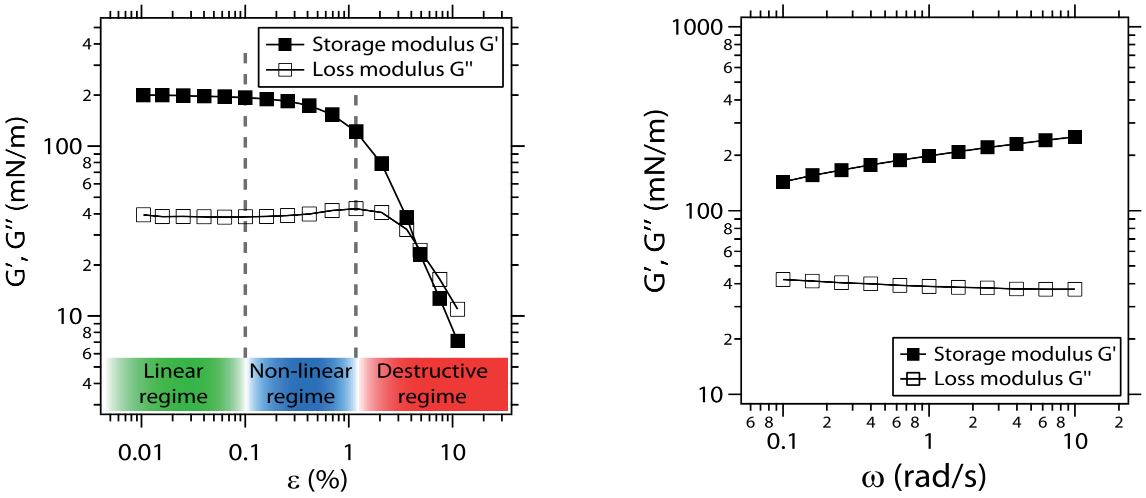

(a) Strain sweep at given frequency $\omega = 1\,\mathrm{rad/s}$. Response is linear until strain $\epsilon = 0.1\,\%$. Then deformation is non-linear (increasing loss modulus G''), and the interface is damaged for strain higher than $\epsilon_\mathrm{y} = 1\,\%$ (high decreases of storage and loss moduli). In the linear regime, storage modulus is significantly higher than loss modulus: $G' = 200\,\mathrm{mN/m} \gg G''$.

(b) Frequency sweep at given amplitude $\epsilon = 0.05\,\%$. Storage modulus increases with frequency, while loss modulus shows small dependency in frequency.

Figure 2.34: Shear deformation of PVP/PMAA bilayer at air/water interface in an interfacial rheometer.

2.6.3 Discussion and comparison with pendant-drop measurement

Comparison between our pendant-drop and the radial-trough experiment. First we compare the values of the interfacial tension upon area compression measured with the pendant-drop method in Section 2.5 (Figure 2.29) with the values obtained with the radial trough (Figure 2.33b).

We find that the initial interfacial tension before compression differs in the two experiments. It is indeed difficult to prepare exactly the same bilayer because the rinsing step between the PVP and the PMAA probably leads to some desorption of the PVP, and this effect depends on the geometry of the set up and the flow used in the experiment.

Then we find that $\gamma(\epsilon)$ curve made with the pendant-drop apparatus superimposes with the second compression made with the radial trough (data not shown). The slope of the $\gamma(\epsilon)$ curve which is equal to the dilational modulus is of the order of $100\,\mathrm{mN/m}$ for both the pendant-drop and the radial-trough experiment.

Comparison between shear and dilational moduli. The compression modulus obtained with the radial trough is $100\,\mathrm{mN/m}$ while the shear modulus obtained with the double wall ring is of the order of $200\,\mathrm{mN/m}$. This means that in the pendant-drop experiment, which involves both a compression of the area and a slight change of shape of the droplets, the effective tension should be influenced by the shear modulus. However we measured a modulus E of the order of $100\,\mathrm{mN/m}$ with the pendant drop in Section 2.5, which is close to the one measured with the radial trough. In fact, in our pendant-drop experiment, using the pressure measurement, we measure the interfacial tension at the apex of the bubbles as well as the local deformation at the apex of the droplets. At the apex, there is probably very little shear deformation and mostly compression. Therefore we suggest that measuring the tension at the apex during compression leads to a measurement of the compression modulus and does not contain a significant contribution of the shear modulus.

Moreover for the PVP/PMAA bilayer, by fitting the whole profile with the classical Young-Laplace Equation, we obtain values of the interfacial tension and compression moduli which are very close to the ones obtained with the pressure measurement. We suggest that the fit is correct all over the profile of the bubble except in a region very close to the needle tip. Provided that this zone is small enough, the value of the tension obtained from the fit seems to be very close to the one obtained from the pressure measurement at the apex.

Even though more systematic measurements should be performed to check these hypothesis, our current understanding is that the pendant-drop experiments involve shear deformation in a small area close to the tip of the needle and that the measurement of the dilational modulus may remain correct for moderate shear moduli and deformations.

To summarize this section:

Independent compression and shear measurements were performed on PVP/PMAA bilayers at the air/water interface.

Compression shows that the dilational modulus of this bilayer is $E = 100\,\mathrm{mN/m}$ **in an intermediate regime between a dilute regime and a plateau were the modulus is smaller.**

Shear measurements exhibit a high elastic shear modulus: $G' = 200\,\mathrm{mN/m}$ **in the linear regime for frequency** $\omega = 1\,\mathrm{rad/s}$**. In the same conditions, viscous modulus is 5 times smaller:** $G'' = 40\,\mathrm{mN/m}$**.**

Compression measurements are in good agreement with previously performed pendant-drop measurements. This means that shear properties do not influence our pendant-drop measurements, since we probe the apex of the droplet, which is highly symmetrical.

2.7 Conclusion

In this chapter, we studied polymer monolayers and multilayers in the model geometry of the pendant-drop apparatus. Using a model system of polymers in which we can tune the anchoring energy with the interface and the strength of the interlayer interactions we studied the adsorption dynamics and the rheology of the first layer, and the rheology of multilayers.

The adsorption of the polymers being spontaneous, a fine understanding of the adsorption dynamics is crucial to control the amount of polymer at the interface. In Section 2.3 we measured the adsorption dynamics of a range of hydrophobically-modified poly(acrylic acid): PAA-α-$\mathrm{C_n}$, where α is the grafting degree and n the length of the grafts. We observed that this dynamics can be described if we take into account the deformation of the incoming chain (as in the Johner and Joanny model) and the deformation of the brush (as in the Ward and Tordai model). Accordingly we suggested a model mixing the two previous ones. By fitting our experiments with this model we observed that the critical area $\mathcal{A}$ that a molecule needs to adsorb increases with the grafting degree. We interpret this as a consequence of a simultaneous adsorption of the grafts for a given molecule.

Because of their high anchoring energy with the interface, these hydrophobically-modified polymers aim at being used as a first layer in multilayers. Accordingly, in Section 2.4 we studied the behaviour of PAA-α-$\mathrm{C_n}$ monolayers under compression and dilatation in pendant drop experiments. We showed that large compression induces polymer desorption. We also showed that this desorption can be limited by increasing the deformation rate or by increasing the length of the grafts. Moreover we showed that increasing the grafting density increases the desorption rate: we interpret this effect as a consequence of the high polymer volume fraction close to the interface due to the high grafting density.

As a logical extension of this work we studied in Section 2.5 the rheology of multilayers and in particular how it depends on the anchoring energy of the first layer and on the interlayer interactions. Using a pendant-drop apparatus we showed that by playing with these two levers we can build multilayers with almost no dilational modulus (such as PVP/PAA), or multilayers with high dilational modulus $E \sim 1000\,\mathrm{mN/m}$ (such as PAA-0.7-$\mathrm{C_{12}}$/PVP/PMAA) which is extremely high compared to the typical modulus of non-desorbing monolayers of Section 2.4 $E \simeq \Pi \sim 30\,\mathrm{mN/m}$ (such as PAA-0.7-$\mathrm{C_{12}}$).

The initial shape of a pendant drop results from a balance between the Laplace pressure and the hydrostatic pressure, and is a complex geometry. Accordingly the deformation of the interface is neither a pure compression/dilatation nor a pure shear, which is an issue when the interface exhibits a shear modulus. To calibrate this experiment and to dissociate shear from compression we performed rheological measurements on a given bilayer in two different model geometries: a radial trough and a shear rheometer. We showed that the PVP/PMAA system exhibits both a high shear modulus which is mostly a storage modulus ($G' = 200\,\mathrm{mN/m} \gg G''$) and a high dilational modulus ($E \simeq 100\,\mathrm{mN/m}$). Despite the high shear modulus, the measured dilational modulus is in good agreement with the one measured in the pendant-drop apparatus because the measurement is performed at the apex of the bubble, which is highly symmetrical and thus involves poor contribution of shear in deformation.

Chapter 3

Microfluidic production and characterization

Contents of this chapter

3.0 Introduction

We have seen in Chapter 1 that microfluidics allows a fine control of the flows and thus a precise handling of the droplets. I have presented the experiments performed by Taylor [53], Martin *et al.* [89, 90] and Brosseau *et al.* [58], which show that microfluidics can be used to deform droplets and capsules.

A goal of my thesis is to produce micro-capsules whose membranes are built by layer-by-layer adsorption through microfluidics and to measure their rheological properties in-situ. The chosen method have to be versatile as it should allow the production or different kinds of multilayers, and the analysis if different kind of rheological properties.

More precisely, I will present in this chapter how we use microfluidics to produce and characterize microcapsules (Figure 3.1). I first present in Section 3.1 how we take advantage of the high level of control allowed by microfluidics to produce droplets and to add polymer layer by layer at the interface to get capsules. Then I will describe in Section 3.2 how we use the high shear rates specific to microfluidics to investigate the mechanical properties of these capsules. To this aim I will simulate numerically the flow in the channel in the presence of a capsule to predict the deformation of this capsule along its trajectory through the chamber. By fitting the experiments with this prediction I will investigate the rheology of the capsule membranes.

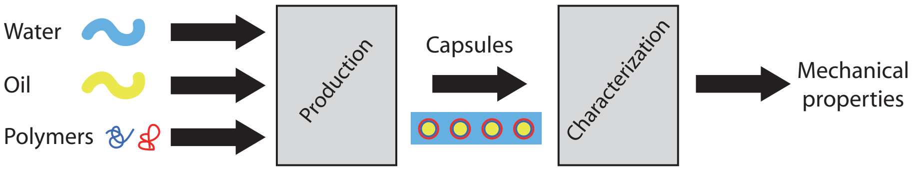

Figure 3.1: Principle of microfluidic production and characterization.

3.1 Microfluidic production of the capsules

Production of microcapsules follows three steps: droplets production with polymer in the external solution, droplet rinsing with water with no polymer, and adsorption of a second layer. The two last steps could eventually be repeated to add more layers, but in this work, we limit the number of layers to two.

Two possibilities have been explored to follow these three steps: the batch and the inline assembly. Our first idea was to produce one batch of capsules with one layer of polymer and to store them in a chamber, rinse them and finally add a second layer by flushing liquid into the chamber: this is is the batch assembly. On the contrary, in the inline assembly, the capsules flow through different areas of the chip where there are in contact with successive polymer solutions.

3.1.1 Material and methods

3.1.1.a Chip fabrication

A microfluidic chip is a network of micrometer sized channels. The overall size of the chip is typically of the order of a few centimeters. Microfluidic chips are disposable, and therefore they must be reproducible. The chips used for the capsule production are based on a crosslinkable polymer: poly(dimethyl siloxane) (PDMS). The PDMS chips are produced following the procedure described by Xia *et al.*[91]. PDMS is a silicon-based polymer which can be poured in a mold and crosslinked to keep the imprint of the mold, as illustrated in Figure 3.2.

The first step consists in designing the chip with a dedicated software: Clewin. The design is then printed on a mask: the channels are transparent, and the other parts are black, as illustrated in Figure 3.2a.

A photo-sensitive resin (*SU-8 photoresist*) is spincoated with the desired thickness on a silicon wafer. Alternatively, a thin sheet of solid photoresist (SUEX) can be laminated on the wafer for the same result. The photoresist is then exposed to UV-light through the mask. The UV-light initializes the crosslinking of the photoresist in the areas corresponding to the transparent zones of the mask. After baking and rinsing with developer (Propylene glycol methyl ether acetate), only the exposed region remains on the wafer, as illustrated in Figure 3.2e. This step can be reproduced with a different mask to add a second layer, in order to obtain areas of different thicknesses. After rinsing with developer and isopropanol, the wafer, as in Figure 3.2b, is ready to use as a mold.

Liquid PDMS with crosslinker (proportion 1:10) is then poured on the wafer, as illustrated in Figure 3.2f. After 2 h at $70°C$ the crosslinking process is over, the solid PDMS layer and the wafer are separated as illustrated in Figure 3.2g. Hence it finally results in a PDMS block with troughs.

The PDMS block is punched to create entrances and exits of 0.5 mm diameter. In the same time, a glass slide is spin coated with a mixture of PDMS and crosslinker (1:10). After a few hours at $70°C$, the glass slide is ready to be sealed to the PDMS block. The sealing is obtained using plasma activation of the PDMS surfaces during 45 s. The troughs of the PDMS block hence create channels, as illustrated in Figure 3.2h.

3.1.1.b Control of the surface properties of the channels

At the channels scale, interfacial effects play a crucial role; therefore the wetting properties of the channels must be carefully controlled: the oil droplets in water stick to any hydrophobic surfaces. As a consequence, we must ensure that the walls are hydrophilic, or that the flow is fast enough to prevent adhesion of capsules on the walls, which would obstruct the channels.

PDMS is naturally hydrophobic. To make PDMS hydrophilic, chips are filled with pure dioxygen and plasma treated during 1 min. Plasma charges PDMS interfaces (the walls), which makes them hydrophilic during a few hours.

3.1.1.c Handling of the microfluidic chips

Pressure control of the flows. The control parameter of the flows in the chips is pressure: every entrance or exit of the chip is connected to a vial in which pressure is imposed. Pressures are set by a pump provided by Fluigent, and monitored through a computer. The applied pressures are of the order of 400 mbar.

Tubing. The vials are connected to the chips through poly(tetrafluoroethylene)(PTFE) tubings (PEEK), of internal diameter 125 μm. Due to PTFE and small diameter imposing high shear rates, as far as we noticed, there is no adhesion of capsules in the tubing.

The production chip and the chip used to characterize the capsules (detailed in Section 3.2) are connected through silicone tubing (Tygon). The inner diameter is 800 μm. Silicon is hydrophobic, and the shear stresses are lower than in the PEEK, due to the large diameter. As a consequence, the inner surface of the Tygon have to be coated to prevent adhesion. Solution at 0.1 %w of bovin serum albumin (BSA) is incubated in the Tygon 12 h before the experiment. The tubing is then rinsed with a large volume of pure water. The BSA molecules adsorb at the interface and make it hydrophilic even after rinsing.

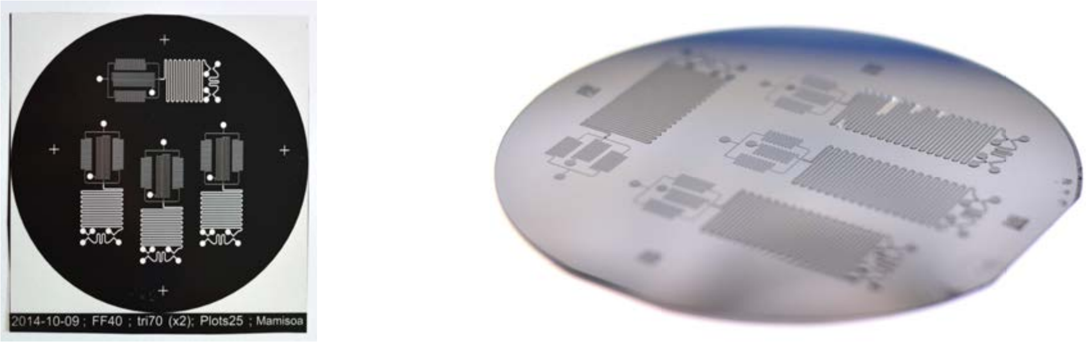

(a) Mask used to flash the photoresist.

(b) Wafer with patterned photoresist.

(c) PDMS molded and punched.

(d) PDMS microfluidic chip: PDMS sealed on PDMS-covered glass.

(e) Mold fabrication.

(f) PDMS pouring and crosslinking.

(g) PDMS block with troughs forming the future channels.

(h) Punched and sealed of PDMS chip.

Figure 3.2: Main steps of fabrication of PDMS-based microfluidic chips: (e) a photo-sensitive resin (yellow) is spincoated on a silicon wafer (black), and illuminated with UV-light through a mask shown in (a). The exposed regions (orange) crosslink during the thermal treatement, duplicating the pattern of the mask on the wafer (b); (f) liquid PDMS (blue) with crosslinker is poured on the silicon mold: after crosslink, the hills of the mold create troughs in the PDMS; (g) solid PDMS (dark blue) is separated from the mold. Transparent lines in the mask have been transfered to PDMS as troughs; (h) solid PDMS block is punched to create entrances and exits (c), and sealed on a glass slide covered by a thin PDMS layer to obtain a microfluidic chip (d).

The external diameter of the PEEK is a bit larger than the holes in PDMS, so that the elasticity of the PDMS maintain the tubings. Tygon tubings are connected to the chips through small metal cylinder which fit exactly in the PDMS holes, and in the Tygon tubings.

The whole setup is represented in Figure 3.3.

Recording. The chip are set in the optical axis of an inverted microscope provided by Leica. The microscope allows the use of Differential Interference Contrast (DIC) to detect the frontier between

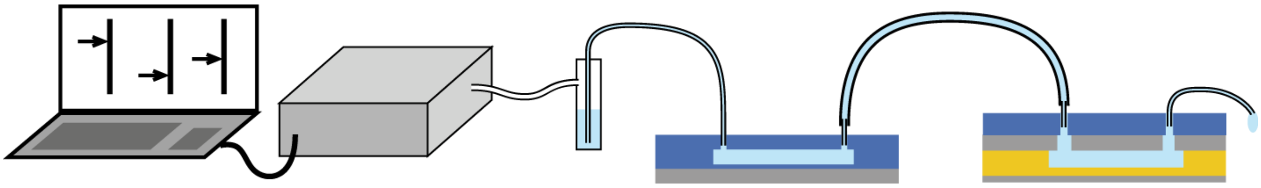

Figure 3.3: Computer sends setpoint values to the pump which imposes the defined pressures in the vials. The vials are connected to the production chip (dark blue) through thin PTFE tubings. The production chip is connected to the characterization chip (yellow) through large silicone tubing. The exit of the characterization chip is connected to a PTFE tubing.

flows of miscible solutions, if the optical indexes are different. The microscope is used with 10x, 20x and 40x objectives.

Moreover, a Photron high-speed camera is mounted on the microscope to record fast events like droplet deformation. The high speed camera is used to record up to 20 000 fps.

3.1.2 Batch production

We first present the batch production. This method requires droplets production, droplet storage, and rinsing steps with pure water and polymer solutions.

3.1.2.a Droplets production

Droplet production has been performed by using a *flow-focusing* device, initially developed by Anna *et al.* [92] and described in Figure 3.4. An oil flow is confined by two lateral flows of polymer solution through a constriction. This configuration is unstable because of the shear and the presence of the interfaces between oil and water. Consequently, this coflow destabilizes into a collection of droplets stabilized by the polymer in the water solution which adsorbs at their interface as surfactants would do.

Two regimes can be observed: a dripping and a jetting regime, as described by Utada *et al.* [93]. In the dripping regime, breakup of the dispersed phase occurs in the constriction: the upstream part recedes, as visible in Figure 3.4b, while the downstream part forms a droplet. For higher flow rates, a jetting regime takes place. In this regime, breakup of the dispersed phase occurs after the constriction: it forms a jet which destabilizes into droplets, as illustrated in Figure 3.4a. The jetting regime usually leads to smaller droplets.

Droplets size depends on the flow rates of the continuous phase (water) and the dispersed one (oil), and on channels geometry. Typical droplets size is ruled by constriction size. Moreover, the higher the flow rate of the continuous phase, the smaller the droplets. For given flow rates in a fixed geometry, droplets size is well defined, leading to monodisperse populations, as shown in Figure 3.5.

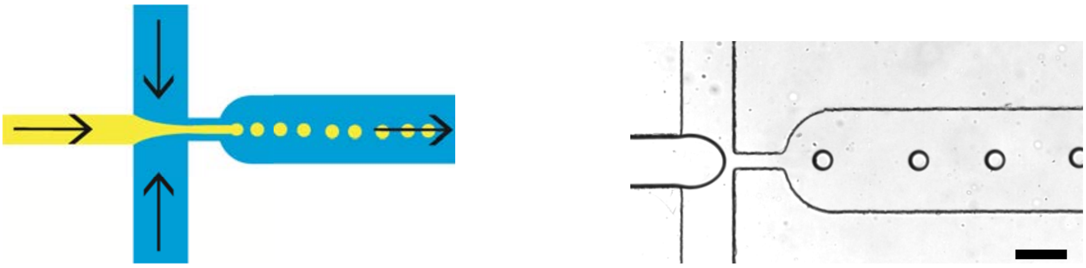

(a) Flow-focusing device: oil (yellow) is pushed with water (blue) through a constriction. The coflow is destabilized into small droplets.

(b) Picture of flow-focusing device when the oil just receded. Scale bar is 250 μm.

Figure 3.4: Flow-focusing device in the dripping regime: oil is pushed through the constriction between two water (containing polymer) streams. This coflow destabilizes in the constriction and breaks, forming a droplet. The oil upstream recedes, and the process starts again. Subfigure (a) illustrates also the jetting regime where a jet passes the constriction and destabilizes after it.

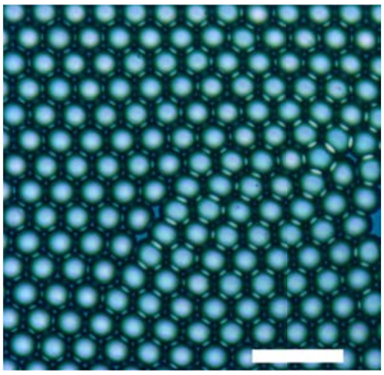

Figure 3.5: Droplets size is well controlled, leading to monodisperse populations and thus to regular ordering of the droplets. Scale bar is 200 μm.

3.1.2.b Droplets storage and rinsing

The droplets must be stored in order to be rinsed with water first and then with polymer solution. To this aim, a large chamber closed by a filter has been designed, as illustrated in Figure 3.6.

In this chamber, the exit is larger than the entrance to minimize the pressure on the droplets close to the filter. Moreover, the height of the chamber is 100 μm while the height of the filter is 50 μm and the width of the holes is 20 μm, to prevent droplets to infiltrate through the filter. Finally, rectangular pillars have been added regularly in the chamber to prevent large deformation of the chamber due to pressure. Two lateral exits enable to purge the chamber.

At the end of the production step, the flow focusing is closed and all the droplets are stored in the chamber. The chamber is rinsed with water at pH 3 during 30 min, and then with a polymer solution during 30 min. The lateral exit is then opened in order to flush the capsules out of the chamber.

3.1.2.c Results

Batch production of capsules allows the rinsing of the droplets with different solutions to add layers of polymers at the interface: droplets are produced in a solution of PMAA (pH 3, 1 %w), and PVP

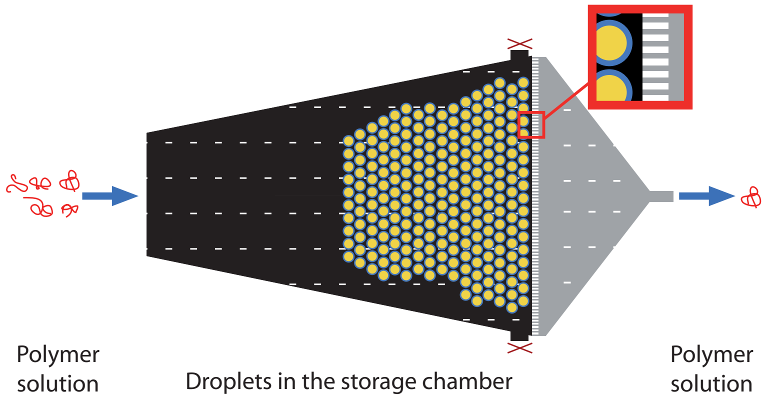

Figure 3.6: Storage chamber of the droplets, of 100 μm height (black region). Capsules arrived from left, and the continuous phase leave on the right because the lateral exits are closed during rinsing steps. The chamber is closed by a filter whose holes are 20 μm wide and 50 μm high (grey region). The rectangular pillars represented by the white dashed lines in the chamber are 200 μm long, and prevent deformation of the chamber due to pressure.

(pH 3, 1 %w) is added by rinsing. It turns out that the capsules couldn't be flushed at the end of the experiment. Indeed, the long stay of the capsules in contact with walls, and the addition of layer create a strong adhesion with the walls. Nevertheless, the flows sheared the capsules, leading to deformation, visualized by the wrinkles of the interface of some capsules as shown in Figure 3.7a, and fracture of the emulsion as illustrated by Figure 3.7b.

The fracture in the emulsion observed in Figure 3.7b is a proof of the cohesion of the emulsion: the assembly of capsules tends to behave like a rigid body. Moreover, the wrinkles that can be observed at the interface of the capsules in Figure 3.7a are an evidence of the elasticity of the membrane.

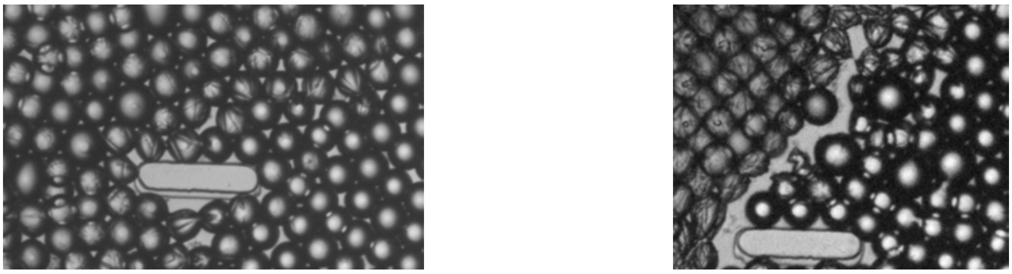

(a) Wrinkles are observed on capsules close to the pillars. Their presence is an evidence of the elasticity of the membrane.

(b) The fracture through the assembly of capsule is an evidence of the adhesion of the capsules with their neighbours.

Figure 3.7: Elastic and adhesive capsules are obtained after adsorption of two layers: PMAA and PVP. Their presence is given by the rectangular pillars of length 200 μm.

3.1.3 Inline continuous production

With the previous method, the adhesion of the capsules in the chamber is an issue difficult to address. Accordingly, we developed a method of capsule production where the capsules always flow through different areas of the chips where they are in contact with different solutions: this is the inline continuous production.

The principle is illustrated in Figure 3.8. After the flow-focusing device (region 1 in Figure 3.8, detailed in Section 3.1.2.a), droplets follow a long channel to let time for polymers to adsorb at the interface: the incubation channel (region 2 in Figure 3.8, detailed in Section 3.1.3.a). At the end of the channel, capsules are extracted from the first polymer solution and put in a second one: this is the rinsing step (region 3 in Figure 3.8, detailed in Section 3.1.3.b). But the two polymers complex together as soon as as they are put into contact. Therefore, to avoid the obstruction of the channels, any contact between the two polymer solutions has to be prohibited. As a consequence, we need to make two phase changes: from first polymer solution to pure water, and then from pure water to second polymer solution.

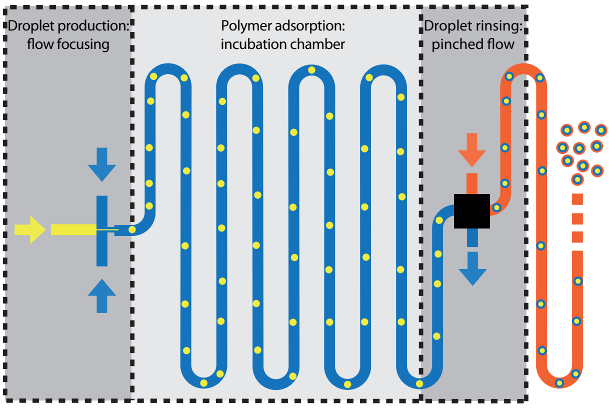

Figure 3.8: Schematic representation of the three steps of inline capsule fabrication. 1: droplet production (detailed in Section 3.1.2.a); 2: incubation channel (detailed in Section 3.1.3.a); 3: Droplets phase transfer (detailed in Section 3.1.3.b). Oil droplets are created in a first polymer solution, and after the incubation channel, they are transferred into a second polymer solution. The transfer actually follows two steps: from first polymer solution to pure water, and then from pure water to second polymer solution, to avoid contact between the two polymer solutions.

3.1.3.a Stabilization of the droplet production

The quantity and the size of the droplets produced in the flow-focusing device depend on flow rates. The control parameter is the pressure differences between the inlets and the outlets in the device. Flow rates depend on the pressures and channels resistance, through the an equation similar to the Ohm's law in electricity (Equation (1.94)). For rectangular channels of length L, width w and height h, the hydrodynamic resistance R_{hydro} of the channel is a function of viscosity of its content η_{eff} [94]:

$$R_{\text{hydro}} = \frac{\eta_{\text{eff}} L}{w h^3} \cdot \frac{12}{1 - \frac{192}{\pi^5} \cdot \frac{h}{w} \cdot \tanh\left(\frac{\pi w}{2h}\right)} \propto \eta_{\text{eff}} \quad . \tag{3.1}$$

The viscosity η_{eff} is the viscosity of the continuous phase containing the capsules. It increases with the size and the quantity of droplets, and so does the hydrodynamic resistance of the incubation channel. Hence the flow rate decreases during the course of the production phase. As a consequence we observe cyclic variations of the droplets size illustrated in Figure 3.9:

- droplets production starts at a given radius r_0,
- the channel resistance increases, the flow rate decreases,
- droplets size decreases,
- channel resistance still increases, flow rate of dispersed phase stops,
- channel resistance is constant,
- first droplets leave the channel,
- resistance decreases
- flow rates increase, droplet production starts again, etc...

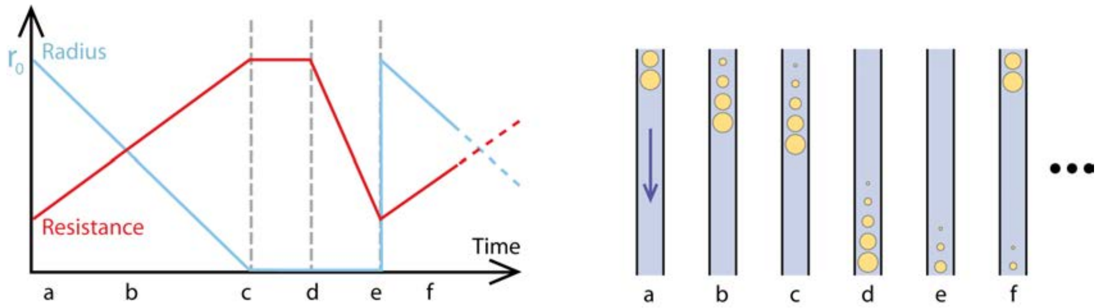

Figure 3.9: Schematic evolution of channel resistance (red) and droplet size (blue) versus time, and representation of the incubation channel containing oil droplets, before stabilization. Droplet production increases the viscosity of the emulsion in the channel and the resistance of the channel. Consequently, flow rates decrease, and thus so does the droplets size, until an arrest of the droplets production. When droplets leave the channel, resistance decreases, and production starts again.

Two possibilities appear to overcome this problem. First, a shorter channel should help to solve this problem. Moreover we realize that flow rates do not depends only upon the incubation channel resistance (red area inFigure 3.10): the resistance of the channels upstream of the flow-focusing device (blue area in Figure 3.10) also plays a role, and these resistances are constant. If the resistance of the incubation channel becomes negligible compared to the resistance of the upstream channels, the flow rates could be constant, and so would the droplets radius.

Accordingly, we decided to make the incubation channel shorter and to modify the upstream channels: the height has been reduced from 100 μm to 50 μm, and the length has been significantly increased, as presented in Figure 3.10.

3.1.3.b Rinsing of the capsules

After the incubation, droplets are transferred from the first polymer solution to pure water, and then to the second polymer solution. The phase change is performed according to the *pinched-flow* protocol developed by Yamada *et al.* [95], and illustrated in Figure 3.11.

Two miscible phases are put into contact through a constriction. The pressures are set in order to confine the phase containing the droplets (the one dyed in blue in Figure 3.11a) close to the wall. The width of this flow must be smaller than the radius of the droplets. Consequently, when the droplets touch the wall, their center of mass switches to the second phase (the one dyed in red in Figure 3.11a). The two phases are separated after the constriction. The trajectories of the droplets are determined by the position of their center of mass, and thus the droplets go into the

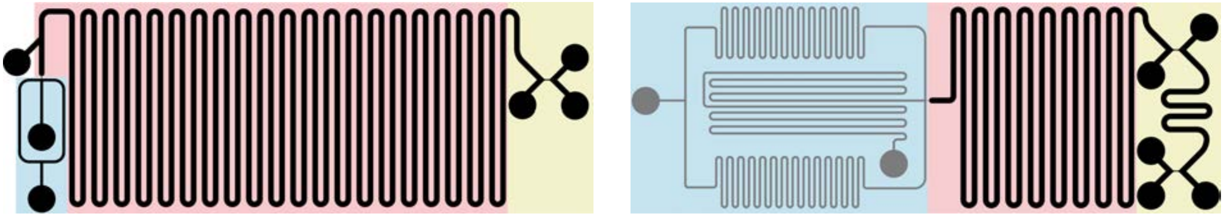

(a) First design: unstable droplet production. There is almost no channel upstream of the flow focusing (blue area), the incubation chamber is long, and there is only one phase change setup (yellow area). The entrance before the incubation channel allows the serial connection of such chips to perform additional rinsing (by bypassing the flow-focusing device).

(b) Final design: stabilized droplet production. Incubation channel has been shortened, channels upstream of the flow focusing have been lengthened, and their height has been divided by two (symbolized by grey color). A second phase change has been added to avoid an additional chip for the second rinsing.

Figure 3.10: Evolution of the design of the production chip. Blue areas correspond to droplet production, red ones to incubation channels, and yellow ones to droplet rinsing. Large circle correspond to entrances and exits.

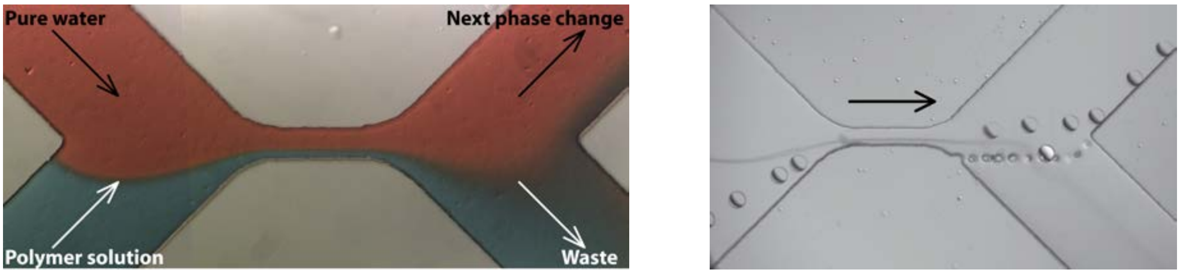

(a) Calibration with dyed solutions.

(b) Droplets rinsing.

Figure 3.11: Droplets rinsing device, adapted from the *pinched-flow fractionation*: the phase containing the droplets is put into contact with a second miscible phase in a constriction. The first phase is confined close to the wall, in a region of thickness smaller than the radius of the droplets. Consequently, the center of mass of the droplets pass in the second phase. When the flows are separated, droplets follow their center of mass, and are transferred into another phase. In the final device, we add a row of small pillars to prevent any anormal sorting.

second phase. In Figure 3.11b, an oil droplet is transferred from polymer solution to pure water. The interface between the two solutions is visible because of the difference of optical index. After flowing in the pure water, the droplets are forced in another pinched-flow cell to move to the second polymer solution.

It is thus possible to adsorb a bilayer at the interface, which should lead to an elastic membrane.

We are now able to produce monodisperse populations of micro-capsules with one or two layers of polymer. The production method is versatile enough to allow the production of various kinds of polymer membranes. We need now to measure the mechanical properties of these capsules, and to relate them to the membrane rheological properties. This measurement will be compared to the macroscopic measurements performed in Chapter 2.

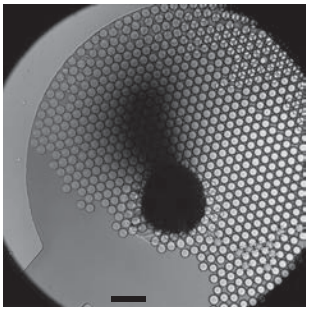

Figure 3.12: Capsule collection at the end of the inline process. This picture is taken at the entrance of the exit tubing (black circle). Monodispersity is revealed by the crystallographic features of the assembly. Scale bar is 200 μm.

To summarize this section:

Two kinds of production devices have been investigated:

- **a batch production, in which droplets are produced in one batch, and covered with polymer layers in a storage chamber,**
- **an inline production, in which every capsule independently follows the same path from droplet production to rinsing and polymer adsorption.**

Layer-by-layer adsorption of polymers at liquid interfaces through microfluidics can be achieved in batch configuration. Droplets are produced in a flow-focusing device, and rinsed in a chamber closed by a filter. Wrinkles have been observed on capsule interfaces, which is an evidence of the elastic behaviour of the interface. Nevertheless, adhesion of the capsules on PDMS hinders the extraction of the capsules, and thus both their use and their characterization.

Inline production does not require capsule storage, and thus solves the adhesion issue. Nevertheless, the length of the incubation chamber leads to instability in the droplets production. We optimized the design to stabilize it. The capsules are then transferred into pure water and then in a second polymer solution to add a second layer of polymer. These transfers are performed using a pinched-flow device.

The inline geometry allows the serial connection of a characterization chip to measure the capsules properties. This geometry will be the device chosen for the rest of the study.

3.2 In-situ mechanical measurement

The next step consists in measuring the mechanical properties of the capsules produced with the inline protocol presented in the previous section. As presented in Figure 3.3, newly produced capsules are injected in a characterization microfluidic chip. The geometry of the channels induces viscous stresses on the capsules, which consequently deform according to their mechanical properties. The analysis of their deformation provides a way to access these properties. Capsules deformation is measured, and in parallel the stresses are calculated using finite-element simulations, as we will describe latter in this section. Experimental deformation will be fitted with the theoretical one according to a model which we will present. We will thus get the interfacial properties of the capsules.

3.2.1 Material and methods

3.2.1.a Fabrication of characterization chips

When the pressure is too high, and when the channels are too large, the PDMS chips tend to deform. As a consequence, the size of the channels slightly depends on the applied pressure. Therefore, the high pressures required for capsule characterization are not compatible with PDMS chips. Accordingly another material, a photosensitive adhesive provided by Norland, is used to build the characterization chips: NOA 81. This method has been developed by Bartolo *et al.*[96] and is known as NOA stickers.

The PDMS block obtained with the previous method (Figure 3.2g) is used as a secondary mold to obtain a stamp with the inverted pattern, as illustrated in Figure 3.13b. The first PDMS piece is treated with gaseous silane to prevent adhesion and help debonding of the two PDMS pieces. The PDMS stamp is used to print the pattern in the adhesive on a glass lamella. The adhesive is crosslinked under UV-light, as shown in Figure 3.13d. Crosslinking is prohibited by oxygen in the PDMS. Consequently, debonding of NOA and PDMS is easy. A drilled glass slide is deposited on the NOA and exposed to UV-light to finish the crosslinking and seal the chip. The channels are thus confined between two non-deformable glass surfaces.

The glass slide is covered by a thick layer of PDMS with holes aligned with those of the glass slide, in order to maintain the connecting tubings. Because of the high speed of the capsules in these chips, there is no adhesion in the NOA chips, and hence the walls don't need to be treated.

3.2.1.b Description of the set-up

Characterization chip consists in a sharp transition between a narrow channel and a wide one, similarly to the chip used by Polenz *et al.* in Baret's group [97] presented in Section 1.2.5.c. Channels design is presented in Figure 3.14a: a large chamber of width $3W$ after a narrow channel of width W imposes a divergent flow at the entrance of the chamber ($(W \in [40, 120]\,\mu\text{m})$). Height of the chamber is $h = 100\,\mu\text{m}$. The flow is illustrated in Figure 3.14b with fluorescent tracers.

Divergent flow at the entrance of the chamber generates viscous stress which should elongates the capsules perpendicularly to the flow direction. The convergent flow of the exit could also be used to deform the capsules. However, the narrow channel makes the capsules more aligned with the

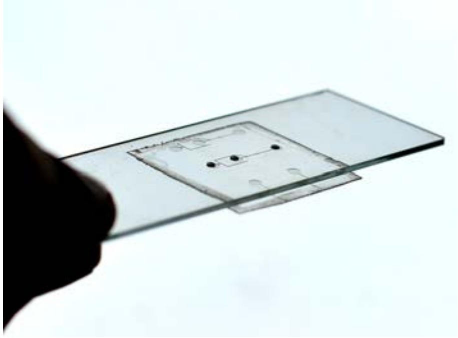

(a) Sealed NOA chip.

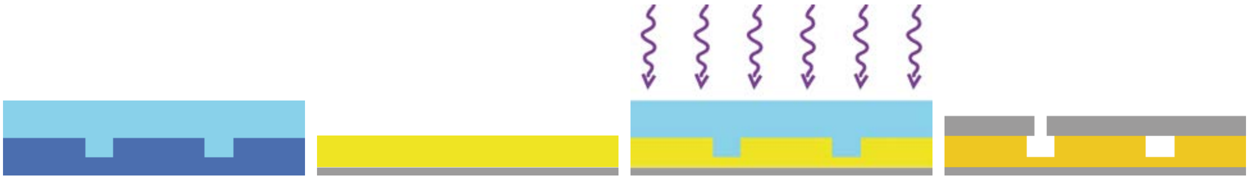

(b) Transfer of the pattern to the PDMS stamp.

(c) Deposition of adhesive on glass lamella.

(d) Stamping and crosslinking of the adhesive.

(e) Sealing of the chip.

Figure 3.13: Steps of fabrication of NOA microfluidic chips (a). (b): the solid PDMS block (dark blue) is used as a mold to shape a second PDMS block (light blue) with a negative pattern; (c): a drop of liquid adhesive (yellow) is poured on a glass lamella; (d): the new PDMS block is used as a stamp to pattern the adhesive during the crosslinking; (e): the crosslinked adhesive (orange) is stuck on a pierced glass slide (grey); A block of PDMS is then stuck on the glass to maintain connections, as seen in Figure 3.3.

(a) Design of the characterization chip. Circles are the entry and the exit of the fluids. A narrow channel of width W is in contact with a large chamber of width $3W$ ($W \in [40, 120]\,\mu$m). The height of the chamber is $h = 100\,\mu$m.

(b) Visualization of the flow inside the chamber with fluorescent tracers without capsule. The flow (from left to right) diverges at the entrance of the chamber, and converges at the exit. Red dashed lines localize the boundaries of the channels.

Figure 3.14: Microfluidic chip used to deform the capsules.

center of the chamber at the entrance than at the exit of the chamber, especially when capsules are laterally confined. As a consequence, observations and measurements are performed at the entrance of the chamber only.

Typical diameter of the capsules is between $50\,\mu$m and $70\,\mu$m. As a consequence, capsules are laterally confined and thus aligned with the center of the chamber of width $W = 40\,\mu$m and $60\,\mu$m. In the z direction, capsules are never confined. Observation is performed along the z direction.

3.2.1.c Image processing for deformation measurements

Pictures as presented in Figure 3.15 are recorded with the same high-speed camera as in Section 3.1 at the entrance of the deformation chamber every 0.1 ms during 2 s. A Matlab program enables us to process this high number of pictures: for every picture, the background is substracted using a picture with no capsule, and then a threshold is automatically set to detect the capsules.

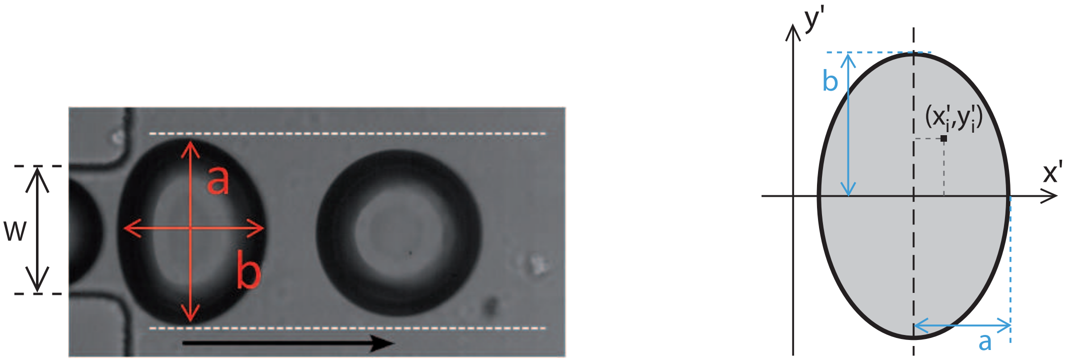

(a) Picture of a capsule entering the chamber showed in Figure 3.14b. Scale: in this case $W = 80\,\mu$m.

(b) Parameters a and b describe the deformation of the capsule. The position of every pixel i is defined by x'_i and y'_i in the frame of reference of the center of the capsule (x_i and y_i in the frame of reference of the chip).

Figure 3.15: Picture (a) and parameters (b) used to measure deformation of the capsule in the chamber.

For every picture containing an entire capsule, the position, the mean radius and the deformation of the capsule are calculated. Position (x, y) is the mean position of all the pixels forming the capsules. Mean radius is calculated with the two semi-axes a and b, in the directions x and y respectively. For small deformations, any deviation from the spherical shape is indeed an ellipsoid in the second order, as noted by R. Cox [98] and J. Rallison [61]. Moreover for symmetry reasons, the axis are along x and y. The mean radius r is the radius of the capsule at rest. By volume conservation, writing c the semi-axis in the z direction:

$$\frac{4}{3}\pi \cdot r^3 = \frac{4}{3}\pi \cdot abc \quad . \tag{3.2}$$

We assume that c is equal to the smallest semi-axis among a and b. Consequently, using Equation (3.2), we write:

$$r = (ab \cdot \min(a, b))^{1/3} \quad . \tag{3.3}$$

Deformation D is defined through the semi-axis a and b as follows:

$$D = \frac{b - a}{b + a} \quad . \tag{3.4}$$

As suggested by Martin *et al.* [89], in the ellipsoidal approximation, it is equivalent but more precise to calculate deformation through the inertia moments along the x-axis and the y-axis, respectively I_x and I_y:

$$D = \frac{\sqrt{I_\mathrm{y}} - \sqrt{I_\mathrm{x}}}{\sqrt{I_\mathrm{y}} + \sqrt{I_\mathrm{x}}} \quad , \tag{3.5}$$

where

$$I_\mathrm{x} = \sum_{\text{pixels i}} (x_\mathrm{i} - x)^2 \quad , \tag{3.6}$$

and

$$I_\mathrm{y} = \sum_{\text{pixels i}} (y_\mathrm{i} - y)^2 \quad . \tag{3.7}$$

Consequently, we know the position and the deformation for every picture containing a capsule. Furthermore, we know that the time lapse between two consecutive pictures is $\Delta t = 0.1\,\mathrm{ms}$, and we have approximately 6 pictures per capsule. For every capsule n, time t_n is counted starting from the first picture where the capsule n is recorded, therefore, t_n is always a multiple of Δt. For every capsule n, time t_n is fitted as a function of position x by a second order polynomial function:

$$t_{\mathrm{n,\,fit}} = a_\mathrm{n} \cdot x^2 + b_\mathrm{n} \cdot x + c_\mathrm{n} \quad . \tag{3.8}$$

In order to synchronize all the capsules with a common time measurement t_sync, we fix $t_\mathrm{sync}(x = 0) = 0$. Accordingly, for every capsule, we define it with the coefficient of Equation (3.8):

$$t_\mathrm{sync} = t_\mathrm{n} - c_\mathrm{n} \quad . \tag{3.9}$$

The capsule are now synchronized: the measurements of the different capsules can be mixed to have one curve $D(t_\mathrm{sync})$.

3.2.2 Experimental observations

We record deformation and position of the capsules for different widths W (from $40\,\mu$m to $120\,\mu$m), and interface coverage (PMAA, PAA-0.7-C_{12}, PMAA/PVP and PAA-0.7-C_{12}/PVP). We start by detailing the effects of each parameter: confinement, nature of the polymers, number of layers.

3.2.2.a Effect of confinement

The width of the incoming channel influences the capsule deformation through two contributions. In the one hand, for a given flow rate and a given capsule radius, the more narrow the channel is, the higher the shear rate is and thus the viscous forces on the capsules. But in the other hand, because the flow is not flow-rate controlled but pressure-controlled, decreasing the width increases the hydrodynamic resistance (Equation (3.1)) and thus decreases the flow rate, and consequently the shear rate. As a result, the evolution of the droplet deformation with the confinement is not monotonic.

In Figure 3.16 we report the deformation of droplets with a layer of PAA-0.7-C_{12} as a function of the capsule position for different channel widths. We observe that there is almost no signal when capsules are not confined, e.g. for $W = 120\,\mu$m, as presented in Figure 3.16a. On the contrary, signal is clear as soon as capsules are confined upstream of the chamber ($W < 2r$) as shown in Figure 3.16b and 3.16c. Moreover, we observe that deformation is more important when $W = 60\,\mu$m than when $W = 40\,\mu$m, and that deformation shows oscillations in the case where $W = 60\,\mu$m. There is yet no theory to explain these observations. Oscillations are often described by a second order differential equation, which often results from inertial effects. These oscillations seems indeed to be observed in experiments with higher flow rates. Moreover, Reynold's number (which represents the ratio of inertial effects over viscous effects) is not very small in these experiments ($\mathcal{R}e \sim 1$), which can be in favour of the inertial effects hypothesis.

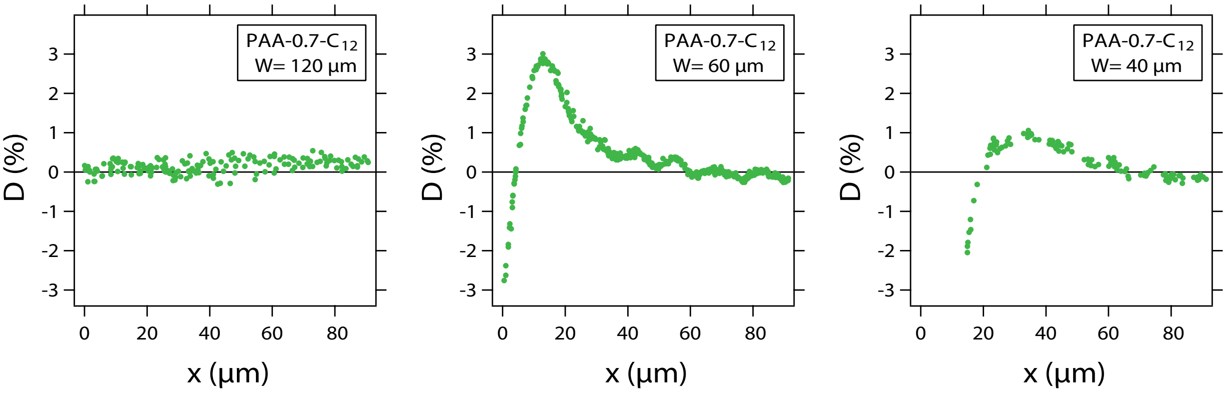

(a) $W = 120\,\mu$m ($r = 28\,\mu$m).
(b) $W = 60\,\mu$m ($r = 34\,\mu$m).
(c) $W = 40\,\mu$m ($r = 26\,\mu$m).

Figure 3.16: Deformation as a function of position depends on initial confinement (W is the constriction width, r is the capsule radius). (a) For unconfined capsules we measure no deformation. (b) For slightly confined capsules, because of the high flow rates, the capsule deforms and we measure oscillations. (c) For strongly confined capsules, the flow rate is a bit lower so we record deformation with no oscillations. (a) In this case, we observe first $D < 0$ for $x = 0$, then due to viscous stress D goes to positive values and relax finally to 0 owing to interfacial tension.

As a consequence, only the experiments with $W = 40\,\mu$m allows us to model precisely the observed phenomena without having to take into account inertial effects. Accordingly, we will study here only the experiments with $W = 40\,\mu$m.

3.2.2.b Effect of anchoring energy for monolayers

Deformation of capsules with a PMAA monolayer follows three steps illustrated in Figure 3.17a:

- an initial negative deformation due to confinement,
- a fast evolution towards positive deformation owing to viscous stress,
- a relaxation towards spherical shape ($D = 0$) because of interfacial tension.

We observe in Figure 3.17b that capsules with PMAA or PAA-0.7-C_{12} monolayers do not deform similarly. With PMAA, final deformation is zero, whereas in the case of PAA-0.7-C_{12}, deformation becomes negative again for $x > 80\,\mu$m.

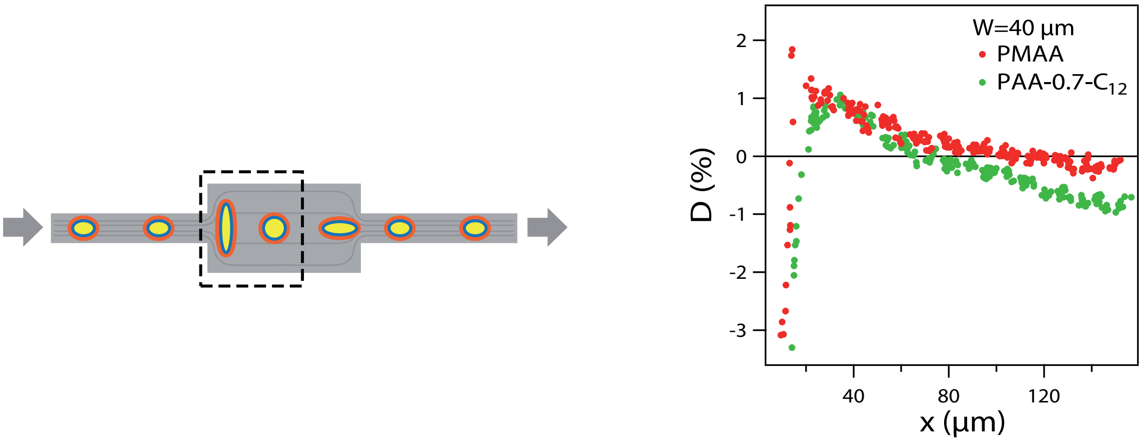

(a) Schematic deformation of capsules with PMAA monolayers in the confined case. The dashed rectangle represents the frame of observation.

(b) Deformation as a function of position for capsules with PMAA and PAA-0.7-C_{12}. The anchoring energy influences the deformation for high values of x.

Figure 3.17: Deformation of capsules covered by monolayers.

3.2.2.c Bilayers

We observe in Figure 3.18 that the addition of a second layer changes drastically the behaviour of the capsules. PMAA/PVP capsules behave differently than what was presented earlier for monolayers: deformation is first negative because of confinement, and then relax directly to almost zero (the final deformation is of the order of -0.5%). As presented in Figure 3.18, PAA-0.7-C_{12}/PVP bilayer also shows only negative deformation, but follows a significantly slower kinetics. Relaxation of PAA-0.7-C_{12}/PVP is so slow that the range of observation had to be extended. The points beyond $x = 160\,\mu$m have been recorded in a second step, after displacement of the chip to observe the downstream area.

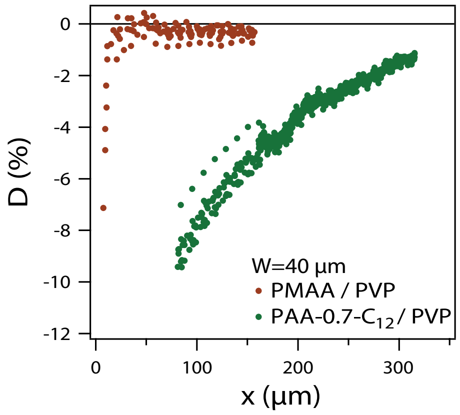

Figure 3.18: Deformation of multilayer capsules versus position in the chamber. Multilayer capsules show various behaviours, but none of them show positive deformation. When observed, final deformation is slightly negative. Relaxation of PMAA/PVP bilayer is very fast, while relaxation of PAA-0.7-C_{12}/PVP is significantly slower.

3.2.3 Analysis

We presented in Section 1.2.5.d the model for the deformation of droplets with a uniform, constant and isotropic interfacial tension. This will be the first step of analysis of our four experimental data sets. In order to compare the experiments with the theoretical predictions given by Equation (1.106), we first need to predict D_{steady} for each experimental conditions. We achieve it by numerical simulations using the software Comsol.

3.2.3.a Calculation of the theoretical steady deformation

In such a complicated geometry with a moving object, it is not straightforward to know the stress undergone by the droplets. Performing numerical simulations is a way to access these data in order to calculate D_{steady} for each particular conditions.

We have thus performed finite-element simulations with the software Comsol to know the stress around the droplets. We should therefore be able to predict theoretical deformation by the flow as a function of time. Velocity field and its gradient are extracted from simulations, and analysed to calculate steady-state deformation of the droplets.

As presented in Figure 3.19, finite-element simulations are performed with the same experimental conditions as in the real experiments (geometry, fluid velocity, fluid viscosity, droplet radius). Viscous stress is extracted from these simulations to calculate the steady deformation for every position of the capsule with Equation (1.105). Knowing the steady deformation function $D_{\text{steady}}(x)$ and the speed of the capsule in the particular case where the membrane has no elasticity but a homogeneous, constant and isotropic interfacial tension, we calculate the theoretical deformation of the capsule as a function of time: $D_{\text{th}}(t)$, with Equation (1.106). The experimental data $D_{\text{exp}}(t)$ is fitted to $D_{\text{th}}(t)$ to get the interfacial properties of the capsule.

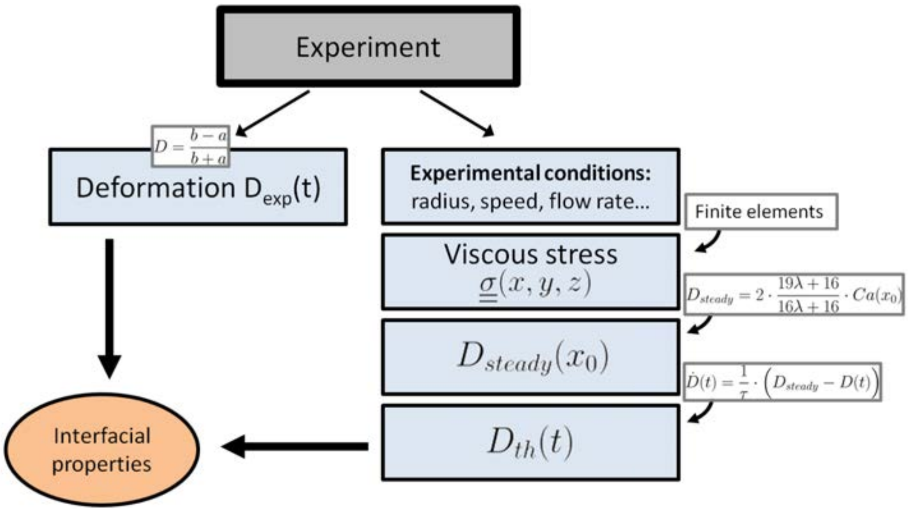

Figure 3.19: Principle of in-situ rheological properties. Capsules are deformed by viscous shear stress, and the experimental deformation is fitted with the theoretical one. Theoretical deformation is calculated with the viscous stress obtained through numerical simulations.

Frame of simulations. The simulated geometry consist in a fix hard sphere at the position $(x_0, 0, 0)$ at the entrance of a chamber three times larger than the incoming channel. The capsule is centred in y and z directions, as presented in Figure 3.20.

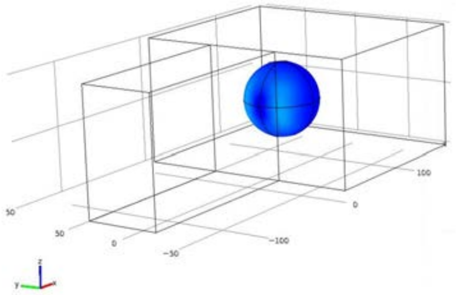

Figure 3.20: Geometry of the simulations: a hard sphere of radius $r = 28\,\mu$m (blue) is placed at a given position in a chamber three times larger than the incoming channel of width $60\,\mu$m. Only the edges of the channels and chamber are represented here.

Experiments have been performed with tracers (diameter $5\,\mu$m) to know precisely the relative speed of water and capsules. It appears that at a distance $x = 150\,\mu$m, capsule velocity is similar to the water speed. Consequently, even without tracers, the final speed of the capsules indicates the flow velocity and thus the flow rate. Therefore, for every simulation, the flow rate and the capsule diameter can be set to mimic a given experiment.

To analyse an experiment, several simulations are made for different positions of the capsule (typically 10 points between $x_0 = 20\,\mu$m and $x_0 = 120\,\mu$m). In the simulation, the capsule do not move, and we simulate steady states.

Boundary conditions. We impose a no-slip condition at the channel walls (no velocity, $u = 0$), which is consistent with the length scale of our experiments (larger than the slip length, which seldom exceeds 100 nm according to Lauga *et al.* [99]), and the newtonian behaviour of water.

The boundary condition at the capsule interface is not straightforward: the capsule of the simulation is fixed, but we want to measure the stress on a moving capsule. We assume that there is no slippage and no interfacial velocity at the capsule interface in our experiments. Consequently, water velocity at the interface (Σ) is equal to experimental capsule velocity:

$$\underline{u(\Sigma)} = \frac{\mathrm{d}\,x_0}{\mathrm{d}\,t} \cdot \underline{e}_{\mathrm{x}} \quad , \tag{3.10}$$

where $\underline{e}_{\mathrm{x}}$ is a unit vector along the x-axis.

Analysis of the simulated data The analysis of the raw data from simulation is computed with Matlab. Simulations provide velocity gradient for every position M:

$$\underline{\underline{\mathrm{grad}}}\,\underline{u} = \begin{bmatrix} u_{\mathrm{xx}} & u_{\mathrm{xy}} & u_{\mathrm{xz}} \\ u_{\mathrm{yx}} & u_{\mathrm{yy}} & u_{\mathrm{yz}} \\ u_{\mathrm{zx}} & u_{\mathrm{zy}} & u_{\mathrm{zz}} \end{bmatrix} \quad , \tag{3.11}$$

where u_{xy} is the derivative of the x-component of velocity $\underline{u}$ with respect to the y-coordinate.

For every position x_0, a boundary layer around the capsule is defined with a thickness equal to 5% of droplet diameter. All the analysis takes place in this boundary layer. Deformation rate $\underline{\underline{d}}$ is defined as the symmetric component of velocity gradient (similarly to Equation (1.45)):

$$\underline{\underline{d}} = \frac{1}{2}\left(\underline{\underline{\mathrm{grad}}}\,\underline{u} + (\underline{\underline{\mathrm{grad}}}\,\underline{u})^{\top}\right) \quad . \tag{3.12}$$

For geometry reasons, we can reasonably assume that the stress is mostly in the (x, y)-plane. Consequently, we consider that there is no stress is the z direction, and we diagonalize the bidimensional deformation rate $\underline{\underline{d}}_{2\mathrm{D}}$ defined as follows:

$$\underline{\underline{d}}_{2\mathrm{D}} = \left[\begin{array}{cc} u_{\mathrm{xx}} & \frac{1}{2}\cdot(u_{\mathrm{xy}} + u_{\mathrm{yx}}) \\ \frac{1}{2}\cdot(u_{\mathrm{yx}} + u_{\mathrm{xy}}) & u_{\mathrm{yy}} \end{array}\right] \quad . \tag{3.13}$$

Diagonalization of $\underline{\underline{d}}_{2\mathrm{D}}$ gives two eigenvalues $e_1(M)$ and $e_2(M)$, and we assume the third eigenvalue $e_3(M)$ (describing the z direction) to be negligible compared to $e_1(M)$ and $e_2(M)$. Each eigenvalue $e_1(M)$, $e_2(M)$, $e_3(M)$ is averaged on the whole boundary layer, and steady deformation $D_{\mathrm{steady}}(x)$ for the position x_0 is calculated with Equation (1.105).

From the simulations we know the stress at the interface. We calculate the steady deformation $D_{\mathrm{steady}}(x)$, and then the theoretical deformation $D_{\mathrm{th}}(t)$, to fit the experimental deformation $D_{\mathrm{exp}}(t)$ and get the fitting parameter γ.

3.2.3.b Validation of the simulations with known geometry

Simulations and their analysis have been checked in a known geometry. We decided to simulate conditions similar to experiments performed by Hudson *et al.* [56, 57, 89] with a viscosity ratio equal to the one taken in our experiment ($\lambda = 30$). In their geometry, the transition between the two widths follows a ramp, and the droplets are small compared to the dimensions of the channels, as illustrated in Figure 3.21.

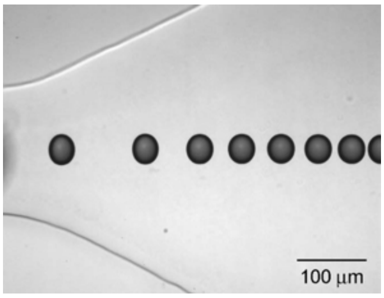

Figure 3.21: Geometry simulated to check the validity of the simulations and analysis: experiments from Hudson *et al.* [56].

Steady deformation predicted by our simulations is compared to the value obtained with the equations used by the authors of the experiments. Their value is calculated with the Taylor Equation (3.14). The authors assume that droplets act like tracers, which means that droplets have the same speed than the surrounding fluid. This simplifying assumption is probably motivated by the small size of the droplets compared to the length scale of the channels and of the section changes. We can point out that this assumption is debatable in their case, and becomes totally wrong in our case. This is why it is necessary to perform numerical simulation. Steady deformation is thus calculated by Hudson *et al.* [56] as follows:

$$D_{\text{steady,Hudson}} = \frac{19\lambda + 16}{16\lambda + 16} \cdot \frac{2\eta_{\text{bulk}}\, r}{\gamma} \cdot \dot{\epsilon} \ , \tag{3.14}$$

where γ is the interfacial tension, r the radius of the droplets, η_{bulk} the viscosity of the fluid, and $\lambda = \frac{\eta_{\text{drop}}}{\eta_{\text{bulk}}}$ the viscosity ratio, and $\dot{\epsilon}$ is the derivative of the capsule velocity v_{capsule} with respect to the position along the x-axis:

$$\dot{\epsilon} = \frac{\mathrm{d}\, v_{\text{capsule}}}{\mathrm{d}\, x} \ . \tag{3.15}$$

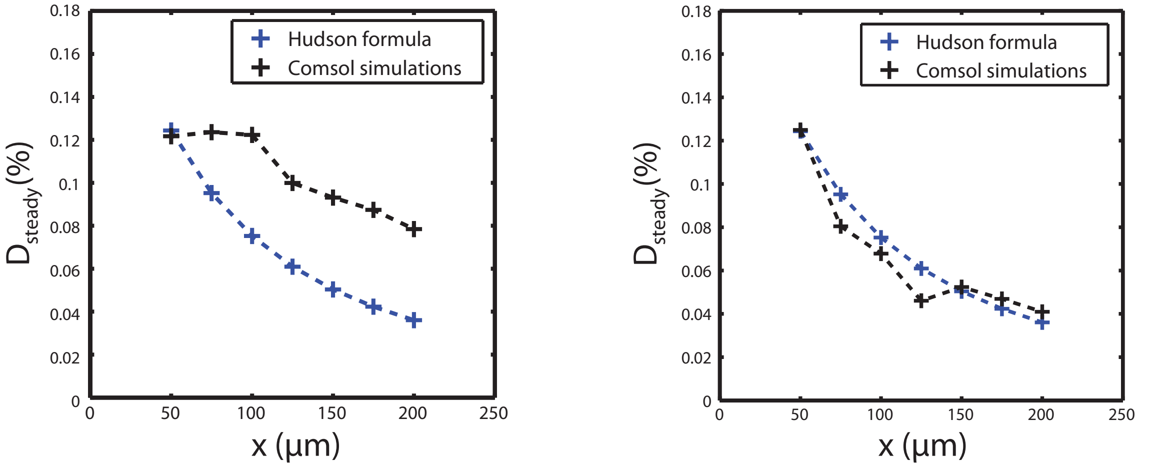

(a) Simulations with a hard droplet at a fixed position.

(b) Simulations without droplet, or (which is equivalent) with a droplet with no boundary conditions.

Figure 3.22: Steady deformation versus droplets position. Comparison between the value calculated with our simulations and Equation (1.105), and the one calculated with the formula used by Hudson *et al.* [56]: Equation (3.14). (a) Simulations considering the presence of the droplet. (b) Simulations without any droplet (or a droplet with no boundary conditions).

Figure 3.22a represents the comparison between our simulations results, and the analytical calculation obtained by the equation used by Hudson *et al.*, Equation (3.14). We can notice that there is a clear discordance between the results given by this equation and our simulations. We then performed simulations without any capsule: the channel is filled with liquid but do not contain any capsule, and we measure the stress in a boundary layer placed where it would be if there was a capsule. The result of this simulation is reported in Figure 3.22b: satisfactorily, our simulations are in good agreement with Equation (3.14).

This agreement comes from the fact that Equation (3.14) is derived from Equation (1.105), which assumes an hyperbolic flow, described by Equation (1.99). This flow is not compatible with the boundary conditions imposed by the droplet, especially if there is no flow at the interface, as prescribed in our simulations. This assumption in our simulations is motivated by the slow dynamics of the polymers at the interfaces: we assume that the experiment is too short (around

1 ms per capsule) to let time for polymers to flow. Interfacial motions are indeed limited by interfacial tension gradients and elastic tensions that they produce.

As a consequence, close to the droplet interface, the flow is not described by Equation (1.99), especially if the droplet is more viscous than the surrounding flow. The presence of the droplet has thus to be taken into account in the calculation of the flow field around it. Taylor [53] observed indeed a discrepancy between the experiments and his theoretical predictions, when viscosity ratio λ becomes significantly higher than 1 ($\lambda = 30$ in our experiments). In Hudson's experiments, $\lambda < 1$. The authors probably chose to describe their flow field by an hyperbolic flow for simplicity reasons. This is not justifiable in our case as we have shown in Figure 3.22a.

Nevertheless, the good accordance of the calculations shown in Figure 3.22b proves that our simulations and calculations are correct, and can be used to measure the stress taking into account the influence of the droplet on the flow.

3.2.3.c Results

The deformation is predicted by Equation (1.106) in which D_{steady} is calculated according to our simulations. In the frame presented in Section 1.2.4, it means that we consider the second model of Table 1.1 and that $\underline{\underline{T}}_{\Gamma}$ is constant.

For a given flow field and capsule radius, we calculated numerically the deformation D_{th} as a function of the capsule position for varying interfacial tension in our geometry. The result is presented in Figure 3.23.

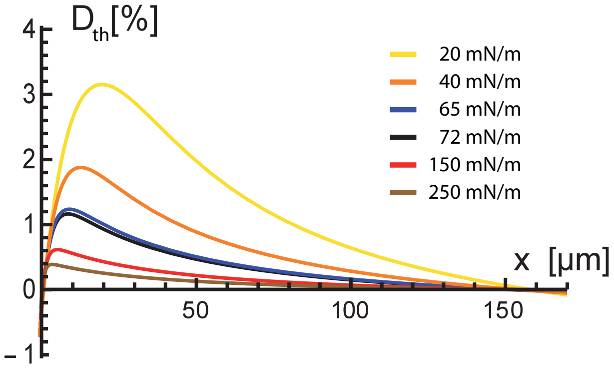

Figure 3.23: Theoretical deformation as a function of capsule position. The calculation consider no liquid or elastic moduli, only an homogeneous, isotropic and constant interfacial tension. The different colors represent the different interfacial tension values.

We observe in Figure 3.23 that the deformation evolves as described in Figure 3.17a. Deformation increases first very fast because of the shear rate. This increase is slightly faster for the higher interfacial tensions. The deformation then reach its maximum value. This maximum value is higher for the lowest interfacial tension values. After this maximum, deformation decreases until zero deformation.

As far as we know, no calculation of the whole deformation profile was made in the literature for such geometry. In Hudson's experiment for example, they do not give the whole evolution of D

with respect to time, but they just extract a characteristic time, from which they get the interfacial tension.

As we can easily predict, tendencies as presented in Figure 3.23 are only compatible with a very restrictive set of experimental data. We will first try to extract parameters from this model before trying to complexify it.

3.2.3.d Analysis of PMAA monolayer

The assumption of constant interfacial tension looks appropriate to describe the deformation of capsules with PMAA monolayer, as presented in Figure 3.24. We find $\gamma = 40\,\mathrm{mN/m}$, which corresponds to a characteristic relaxation time τ_{ca} defined by Equation (1.107) equal to $\tau_{\mathrm{ca}} = 2.33 \cdot 10^{-5}\,\mathrm{s}$. The interfacial tension obtained by the fitting is in fair agreement with the pendant-drop measurement with the same mineral oil which yields $\gamma = 31\,\mathrm{mN/m}$.

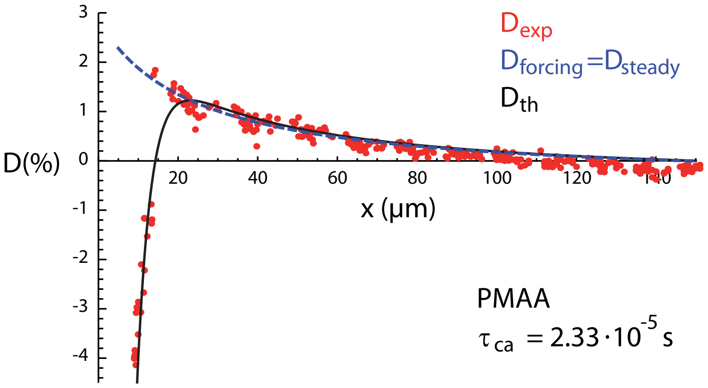

Figure 3.24: Deformation as a function of time for PMAA monolayer. We find $\gamma = 40\,\mathrm{mN/m}$ ($\tau_{\mathrm{ca}} = 2.33 \cdot 10^{-5}\,\mathrm{s}$).

Owing to our simulations it is thus possible to fit the whole profile and to check the validity of the model. However, as shown in Figure 3.25, this simple model is not sufficient to fit with PAA-0.7-C_{12} capsules. Such capsules have a membrane at their interface which can not be described by a simple homogeneous and constant interfacial tension.

3.2.4 A more comprehensive model

In the case of an elastic membrane with no interfacial tension, another model has been suggested by Barthes-Biesel and Rallison [60]. In this case, such capsule initially deformed in a fluid at rest recovers exponentially its spherical shape following the equation:

$$\dot{D} = \frac{1}{\tau_{\mathrm{el}}} D \ , \tag{3.16}$$

where the time scale of this elastic motion is:

$$\tau_{\mathrm{el}} = \frac{3(19\lambda + 16)(2\lambda + 3)}{5(19\lambda + 24) \pm \sqrt{5377\lambda^2 + 14256\lambda + 9792}} \cdot \frac{\eta_{\mathrm{w}} r}{3G'} \ , \tag{3.17}$$

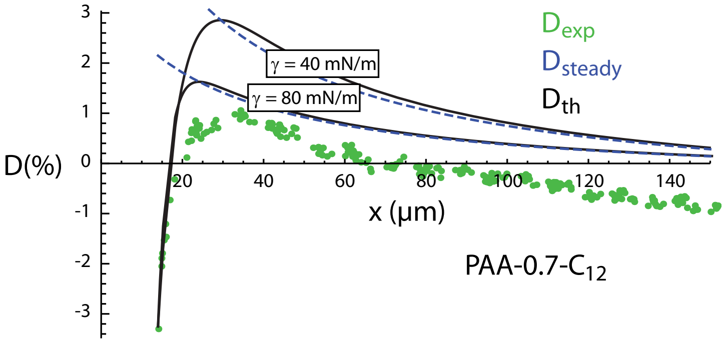

Figure 3.25: Deformation as a function of time for PAA-0.7-C$_{12}$ monolayer. We find that neither $\gamma = 40\,\text{mN/m}$ nor higher interfacial tension can fit our data. The interface of such capsules can not be described by a simple homogeneous, isotropic and constant interfacial tension.

where λ is the viscosity ratio, η_w the viscosity of the surrounding solution, r the radius of the capsule and G' the shear modulus of the elastic membrane.

Moreover, Leclerc *et al.* [100] indicates that the largest relaxation time rules the relaxation of the membrane, and thus

$$\tau_\text{el} = \frac{3(19\lambda + 16)(2\lambda + 3)}{5(19\lambda + 24) - \sqrt{5377\lambda^2 + 14256\lambda + 9792}} \cdot \frac{\eta_\text{w} r}{3G'} \quad . \tag{3.18}$$

Using the same characteristic time (Equation (3.17)), a variant of Equation (3.16) has been recently proposed by Gires *et al.* [101] for viscoelastic membranes, which also does not take into account the extensional flow field. In our geometry, we showed that this extensional flow cannot be neglected and deforms the drop. We decided to focus on the simple exponential relaxation model (i.e. Equation (3.16)) which seems more theoretical and less empirical for us than its variant, and to investigate how we can take into account this exponential relaxation in a case where interfacial tension and extensional flow still play a role.

We therefore have two distinct models for two extreme cases, the purely capillary one (defined by Equation (1.106) for interfaces corresponding to the model 1 in Table 1.1) and the purely elastic one (defined by Equation (3.16) for interfaces exhibiting only $\underline{\underline{T}}_\text{elastic}$ in Table 1.1). Besides, we have some experimental indications from Chapter 2:

- interfacial tension of PAA-0.7-C$_{12}$ is not constant under compression,
- PMAA/PVP exhibits shear and dilational moduli of the order of the interfacial tension.

To take these effects into account we suggest that deformation results from two contributions:

- a contribution due to the competition between the shear rate in the continuous phase which deforms the capsule and the interfacial tension which limits this deformation. This competition is described by Equation (1.106) in Section 1.2.5.d,
- a contribution due to the restoring elastic forces toward a reference shape described by D_ref: the dynamics of these restoring effect is described by Equation (3.16).

We showed in Section 1.2.4.d that the variation of interfacial tension due to surface excess variations can be taken into account in the elastic effects, by defining an effective dilational modulus E. The variation of interfacial tension due to the deformation of the capsules will thus be taken into account in the restoring forces.

Furthermore, the interface is viscoelastic, which means that the polymer chains themselves relax. For instance if the polymers adsorb at the interface when the droplet is confined (and thus deformed), when there is no confinement any more the shape of the capsule should depend on time, even without external flow field. At short time scale the shape of the capsule should be a compromise between the initial shape (minimizing the strain for the elastic membrane and hence the elastic energy) and the spherical shape (minimizing the area and hence the energy due to the homogeneous and isotropic component of interfacial tension). The membrane is viscoelastic and hence at long time scale, the polymer chains and thus the elastic stresses should relax and the droplet should become spherical. To take this viscoelastic relaxation into account in our model, we write that D_{ref} (which is the reference shape for the elastic relaxation) relaxes towards zero over a time τ_{pol}. In the previous example, the initial reference deformation D_{ref} is the shape of the droplet during the adsorption of the polymers.

We would like here to insist on the distinction between this time τ_{pol} and the two other time scales τ_{ca} and τ_{el}, which describe the relaxation of the capsule shape according to a competition between a driving force (interfacial tension or elasticity) and the bulk viscosity. On the contrary, τ_{pol} describes the relaxation of the stress within the membrane, and is thus related to the relaxation of the polymer chains and to the viscoelasticity of the material. The typical length scales of these two processes are thus totally different: τ_{ca} and τ_{el} describe the capsule as an object of a few ten of micrometers, while τ_{pol} describe the dynamics of the polymer chains, whose size is of the order of a few tens of nanometers. Accordingly we expect τ_{pol} to be independent of the capsule radius r, while we know from Equations (1.107) and (3.18) that τ_{ca} and τ_{el} scales linearly with r.

We propose a complete model summarized by the following equations:

$$\begin{cases} \dot{D}(t) = \dfrac{1}{\tau_{\mathrm{ca}}}(D_{\mathrm{steady}}(t) - D(t)) + \dfrac{1}{\tau_{\mathrm{el}}}(D_{\mathrm{ref}}(t) - D(t)) \ , & \text{(3.19a)} \\[2ex] \dot{D}_{\mathrm{ref}}(t) = \dfrac{1}{\tau_{\mathrm{pol}}}(0 - D_{\mathrm{ref}}(t)) \ . & \text{(3.19b)} \end{cases}$$

The second relaxation time τ_{el} can depend on different moduli: E_γ, K', G'. More generally, we note E the effective modulus which is a combination of these three moduli (E is expected to be close to the highest of these three moduli). We can thus write that:

$$\tau_{\mathrm{el}} \propto \frac{\eta_{\mathrm{w}} r}{E} \ . \tag{3.20}$$

We would like to point out that a long relaxation time of the polymers τ_{pol} usually implies a high modulus in simple systems: for instance in the Lucassen model introduced by Equation (1.62) in Section 1.2.4.c, a long relaxation time τ_{pol} is due to a low diffusivity D. This implies a low value of the parameter ζ, which yields a high value of E_γ. Such systems would relax over a short time τ_{el}.

In more complex systems, the link between τ_{pol} and τ_{el} can be more complex. This is in particular what we will see in the following description. For this reason, we need to distinguish these two parameters.

We also note that we can write Equation (3.19a) so as to reduce D_{steady} and D_{ref} into one forcing function D_{forcing}:

$$\dot{D}(t) = \frac{1}{\tau_{\mathrm{forcing}}}\left(D_{\mathrm{forcing}}(t) - D(t)\right) \ , \tag{3.21}$$

where

$$\tau_{\mathrm{forcing}} = \left({\tau_{\mathrm{ca}}}^{-1} + {\tau_{\mathrm{el}}}^{-1}\right)^{-1} \ , \tag{3.22}$$

and

$$D_{\mathrm{forcing}}(t) = \tau_{\mathrm{forcing}} \cdot \left({\tau_{\mathrm{ca}}}^{-1} \cdot D_{\mathrm{steady}}(t) + {\tau_{\mathrm{el}}}^{-1} \cdot D_{\mathrm{ref}}(t)\right) \ . \tag{3.23}$$

We are now able to predict the capsules theoretical deformation D_{th} with an interfacial tension and elastic effects. We will consider how this model can describe all the different behaviours seen in the experimental part, and how we can extract the three fitting parameters τ_{ca}, τ_{el} and τ_{pol}.

3.2.4.a PMAA monolayer

We can easily notice that Equation (1.106) which was used to fit the PMAA monolayer in Figure 3.24 is a specific case of Equation (3.19a). Considering fast reorganisation of the chains at the interface and thus a weak modulus $E \to 0$ yields an infinite elastic time τ_{el}, and consequently the left-hand term of Equation (3.19) can be neglected, leading to an Equation similar to Equation (1.106). Fitting the deformation of the PMAA monolayer would thus yield $\tau_{\mathrm{ca}} = 2.33 \cdot 10^{-5}\,\mathrm{s}$ as seen previously in Figure 3.24, and we fixed in this case $\tau_{\mathrm{el}} \to \infty$ and $\tau_{\mathrm{pol}} \to 0$.

3.2.4.b PAA-0.7-C$_{12}$ monolayer: low dilational modulus

We know from the experiments performed in pendant-drop apparatus and presented in Section 2.4 that in the case of PAA-0.7-C$_{12}$, interfacial tension depends on deformation. As a consequence, we expect that capsule deformation leads to areas with higher interfacial tension (dilated areas) and other ones with lower interfacial tension (compressed areas). These inhomogeneities should be proportional to undergone deformation and to the liquid dilational modulus E_γ of PAA-0.7-C$_{12}$. We have also shown in Section 1.2.4.d that these interfacial-tension variations due to deformation behave like isotropic elastic stresses. We consider the effect of these interfacial-tension variations as an effective restoring stress. This stress will relax over a time scale noted τ_{pol}. This relaxation can be due either to adsorption/desorption processes, as in the model presented in Section 1.2.4.c, or to an in-plane reorganization of the polymers.

We assume here that the upstream channel is long enough to have these restoring stresses totally relaxed before the capsules enter the chamber. As illustrated in Figure 3.26, this assumption leads us to expect that initially the new reference deformation is equal to the actual deformation at the exit of the confining channel: $D_{\mathrm{ref}}^{(initial)} = D^{(initial)}$. The capsule is confined in the upstream channel during a time $\tau_{\mathrm{conf}} \simeq 10^{-2}\,\mathrm{s}$. This assumption is thus justified if we obtain $\tau_{\mathrm{pol}} \ll \tau_{\mathrm{conf}}$.

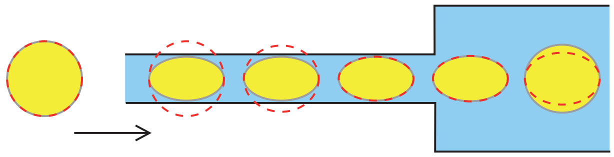

Figure 3.26: Schematic deformation of the capsule along its trajectory before the deformation chamber, with the corresponding reference deformation D_{ref} (red dashed line). In the confining channel, when the elastic stresses relaxes, the reference deformation becomes the present deformation of the capsule.

Consequently, we need to consider the whole model presented in Equation (3.19) to fit the experimental data of PAA-0.7-C$_{12}$ capsules. The result is presented in Figure 3.27. We find an interfacial tension of 35 mN/m (leading to $\tau_{\text{ca}} = 3.03 \cdot 10^{-5}$ s), $\tau_{\text{el}} = 1.7 \cdot 10^{-4}$ s and $\tau_{\text{pol}} = 1.2 \cdot 10^{-3}$ s.

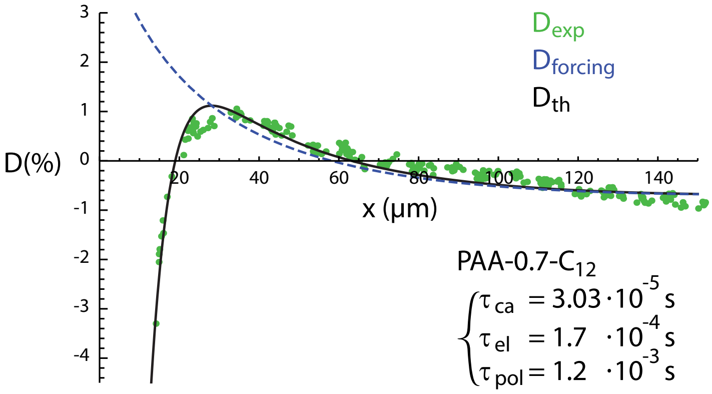

Figure 3.27: Deformation as a function of time for PAA-0.7-C$_{12}$ monolayer. We find $\gamma = 35$ mN/m ($\tau_{\text{ca}} = 3.03 \cdot 10^{-5}$ s), $\tau_{\text{el}} = 1.7 \cdot 10^{-4}$ s and $\tau_{\text{pol}} = 1.2 \cdot 10^{-3}$ s.

Pendant-drop experiments at oil/water interface showed that the interfacial tension with PAA-0.7-C$_{12}$ is about 25 mN/m. As in the case of the PMAA monolayer, we find an interfacial tension higher than in pendant-drop experiments, but we have a fair order of magnitude agreement, and we recover the fact that interfacial tension is higher for PMAA than for PAA-0.7-C$_{12}$. Moreover, we observe that $\tau_{\text{el}} \gtrsim \tau_{\text{ca}}$, which we interpret as follow: the interfacial tension variations are low compared to the interfacial tension. Moreover, we find that $\tau_{\text{pol}} \ll \tau_{\text{conf}}$. Accordingly at the end of the confining channel, when the capsule enters the chamber, all the elastic stresses have relaxed. Hence the reference deformation D_{ref} corresponds to the shape of the capsule when it enters the chamber. This was our initial assumption, which is thus justified.

3.2.4.c PAA-0.7-C$_{12}$/PVP bilayer: high interfacial modulus

We apply the same model to the PAA-0.7-C$_{12}$/PVP capsules, as presented in Figure 3.28. We find the same interfacial tension as for PAA-0.7-C$_{12}$ monolayers ($\gamma = 35$ mN/m), which leads to $\tau_{\text{ca}} = 3.25 \cdot 10^{-5}$ s (we remind here that τ_{ca} also depends on the capsule radius, which slightly varies between the different experiments). Moreover we find the same polymer relaxation time as in the case of PAA-0.7-C$_{12}$ monolayer $\tau_{\text{pol}} = 1.2 \cdot 10^{-3}$ s, but a significantly lower elastic time $\tau_{\text{el}} = 3.0 \cdot 10^{-6}$ s.

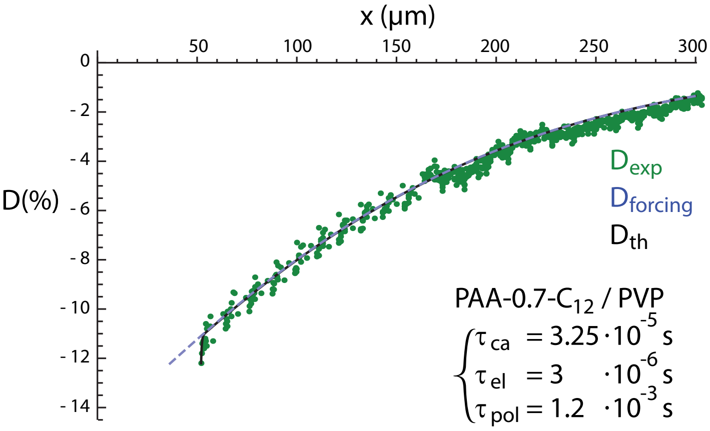

Figure 3.28: Deformation as a function of time for PAA-0.7-C$_{12}$/PVP bilayer. We find $\gamma = 35\,\mathrm{mN/m}$ as for the corresponding monolayer ($\tau_{\mathrm{ca}} = 3.25 \cdot 10^{-5}\,\mathrm{s}$), $\tau_{\mathrm{el}} = 3 \cdot 10^{-6}\,\mathrm{s}$ and $\tau_{\mathrm{pol}} = 1.2 \cdot 10^{-3}\,\mathrm{s}$, as for the corresponding monolayer.

According to Equation (3.20), the significantly shorter elastic relaxation time of the bilayer compared to the monolayer implies that the elastic modulus E is significantly higher for the bilayer than for the monolayer, which is well explained by the interactions between PAA-0.7-C$_{12}$ and PVP.

The value obtained for the polymer relaxation time ($\tau_{\mathrm{pol}} \simeq 1\,\mathrm{ms}$) is coherent with pendant-drop experiments: wrinkles were never observed during compression neither for PAA-0.7-C$_{12}$/PVP bilayers (Figure 2.14b) nor for PAA-0.7-C$_{12}$ monolayers, which indicates that this polymer relaxation time is shorter than the typical time scale of such experiments which is of the order of $\sim 1\,\mathrm{s}$.

We interpret the concordance of the polymer relaxation time τ_{pol} between the monolayer and the bilayer as a consequence of the predominance of the anchoring on the dynamics of the interface, especially when there is no strong interactions between the layers.

A second evidence of the predominance of anchoring is the comparison with an analogous experiment performed with PAA-0.8-C$_8$/PVP, presented in Figure 3.29.

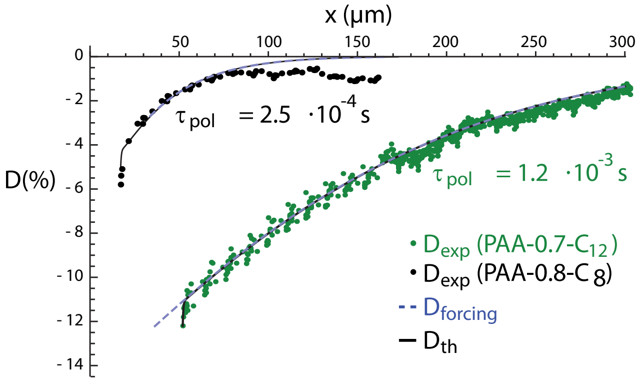

Figure 3.29: Effect of the anchoring energy on the bilayer relaxation. Shorter grafts and thus lower anchoring energy leads to faster relaxation. γ and τ_{el} are the same for the two bilayers.

We observe that the relaxation of such bilayer is much faster than the relaxation of PAA-0.7-C$_{12}$/PVP, which is consistent with what we observed in Figure 2.22b (Section 2.4): desorption of PAA-0.8-C$_8$ is faster than desorption of PAA-0.7-C$_{12}$. Moreover, if the relaxation of the bilayer capsules were set by the moduli only (and thus τ_{el}), because the modulus is higher for PAA-0.7-C_{12} than for PAA-0.8-C_8, we would expect a faster relaxation of PAA-0.7-C_{12}/ PVP than PAA-0.8-C_8/ PVP, which is not what we measured. This comparison between PAA-0.8-C_8/PVP and PAA-0.7-C_{12}/PVP thus indicates that the relaxation time which rules the overall relaxation of the capsule is the polymer relaxation τ_{pol}.

3.2.4.d PMAA/PVP bilayer: high interfacial modulus and slow polymer relaxation

Unlike the PAA-0.7-C_{12}/PVP bilayer, the PMAA/PVP system shows wrinkles when compressed in pendant-drop experiments, as presented in Figure 3.30. Accordingly, we expect to have $\tau_{\mathrm{pol}} > 1\,\mathrm{s}$, which has two consequences.

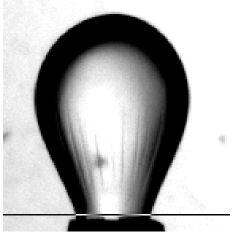

Figure 3.30: Wrinkled membrane of PMAA/PVP at the dodecane/water interface in a pendant-drop apparatus.

First, this time is much longer than the time during which the capsules are confined τ_{conf}. So we assume that the reference deformation D_{ref} is initially close to zero (because of the memory of the non-deformed state before confinement). Indeed polymers do not have time to rearrange in the confining channel. Furthermore τ_{pol} is so long that it is considered as infinite compared to the typical time scale of our microfluidic measurement which is about 1 ms. Therefore we decided to fix the value of the reference deformation D_{ref} to a constant, which corresponds to fix $\tau_{\mathrm{pol}} \gg 10^{-3}\,\mathrm{s}$.

Consequently, to fit our experiment with our model, we consider a reference position which is constant and which is expected to be close to zero. The result of the fit is presented in Figure 3.31. We find the same interfacial tension as for the PMAA monolayer $\gamma = 40\,\mathrm{mN/m}$ (leading to $\tau_{\mathrm{ca}} = 2.8 \cdot 10^{-5}\,\mathrm{s}$), and an elastic time $\tau_{\mathrm{el}} = 3 \cdot 10^{-6}\,\mathrm{s}$ similar to the elastic time of PAA-0.7-C_{12}/PVP, with a polymer relaxation time $\tau_{\mathrm{pol}} \gg 10^{-3}\,\mathrm{s}$.

3.2.5 Discussion

We summarize in Table 3.1 the different results obtained by fitting our experiments with our complex model. The modulus E is calculated from τ_{el} according to Equation (3.18).

The order of magnitude of the obtained moduli are in fair agreement with what we expected from macroscopic measurements. In the case of PAA-0.7-C_{12} where the modulus is liquid dilational modulus E_γ, in the case where there is no desorption, we can show that $E_\gamma = \Pi$, where Π is the surface pressure. The surface pressure of PAA-0.7-C_{12} at the mineral oil/water interface is $\Pi \simeq 10\,\mathrm{mN/m}$. This leads to $E_\gamma \simeq 10\,\mathrm{mN/m}$, which is in fair agreement with what we obtained in our experiments and reported in Table 3.1. For the PAA-0.7-C_{12}/PVP bilayer, no measurement of

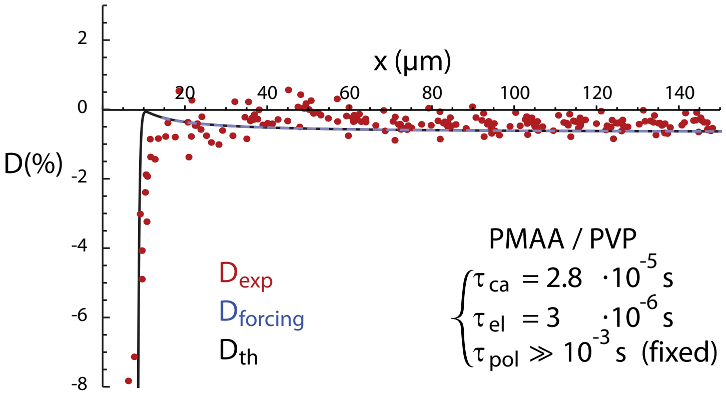

Figure 3.31: Deformation as a function of time for PMAA/PVP bilayer. We find $\gamma = 40\,\mathrm{mN/m}$ as for the corresponding monolayer ($\tau_{\mathrm{ca}} = 2.8 \cdot 10^{-5}\,\mathrm{s}$), $\tau_{\mathrm{el}} = 3 \cdot 10^{-6}\,\mathrm{s}$ as for PAA-0.7-C$_{12}$/PVP and we considered $\tau_{\mathrm{pol}} \gg 10^{-3}\,\mathrm{s}$.

	γ (mN/m)	τ_{ca} (s)	τ_{el} (s)	τ_{pol} (s)	E (mN/m)
PMAA	40	$2.33 \cdot 10^{-5}$	–	–	–
PAA-0.7-C$_{12}$	35	$3.03 \cdot 10^{-5}$	$1.7 \cdot 10^{-4}$	$1.2 \cdot 10^{-3}$	$1.3 \cdot 10^{1}$
PAA-0.7-C$_{12}$/PVP	35	$3.25 \cdot 10^{-5}$	$3 \cdot 10^{-6}$	$1.2 \cdot 10^{-3}$	$6.9 \cdot 10^{2}$
PMAA/PVP	40	$2.8 \cdot 10^{-5}$	$3 \cdot 10^{-6}$	$\gg 10^{-3}$	$6.9 \cdot 10^{2}$

Table 3.1: Parameters extracted from the fit of the data with our complex model.

the elastic modulus has been performed at time scales smaller than $\tau_{\mathrm{pol}} \simeq 1\,\mathrm{ms}$, and consequently we have no reference to compare the obtained value of the modulus. On the contrary, the value extracted from the experiment with PMAA/PVP is close to the value measured in the interfacial rheometer in Section 2.6 at the air/water interface ($G' = 200\,\mathrm{mN/m}$).

The model described in Equation (3.19) offers a good understanding of the phenomena ruling the relaxation of the capsules, and even a satisfactory qualitative agreement with more calibrated experiments.

Nevertheless, this model is at some point a bit naive, especially on the description of the reference-shape relaxation. We think that this model could be improved by replacing Equation (3.19b) by

$$\dot{D}_{\mathrm{ref}} = \frac{1}{\tau_{\mathrm{pol}}} \cdot (D - D_{\mathrm{ref}}) \quad , \tag{3.24}$$

which implies that the reference shape relaxes toward the actual shape, and not especially toward the spherical shape. This would probably better describe the reference deformation, but it significantly complicates the computation of the theoretical deformation. The analysis could also be improved by simulating the flow with deformed capsules, especially when the capsule is close to the entrance of the channel.

Moreover the strong influence of τ_{pol} and the confinement lapse of time τ_{conf} which leads to the differences observed between the PAA-0.7-C$_{12}$/PVP and PMAA/PVP system suggest that the experiment could be performed for varying τ_{conf}. This could possible just by changing the length of the confining channel. This would be a way to measure more precisely the value of τ_{pol}, and thus the other time scales.

To summarize this section:

When entering in a large chamber, capsules deform because of extensional shear stress due to the brutal width change. We performed experiments with different polymer systems at the interface: PMAA, PAA-0.7-C_{12}, PMAA/PVP, and PAA-0.7-C_{12}/PVP. We observe that deformation is larger when capsules are laterally confined before entering the chamber. In this case, deformation is first negative, and relaxes differently depending on the surface coverage and the flow rate. We model the relaxation as the sum of two effects: the viscous forcing due to the external flow field, and the resistance of the membrane to deformation due to its elasticity or its surface excess inhomogeneities. We consider that this resistance also relaxes with a characteristic time which depends on polymers.

Finite-element simulations are performed to know how the flow is disturbed by the presence of the capsule, and what is the shear stress applied on it. For every position of the capsule, simulations give us the steady deformation which would be observed if the capsule experienced this viscous stress for a long time. This simulated steady deformation has been successfully compared to the equations used by Hudson *et al.* [56], in conditions respecting their assumptions.

We showed that the experimental deformation of our four systems could be described by our model. We observed that PMAA monolayers can be described with no interfacial modulus (neither liquid one nor elastic one). On the contrary, PAA-0.7-C_{12} monolayers can not be described without interfacial modulus. This is in agreement with the results of the previous chapter. We also showed that the deformation of bilayers (PMAA/PVP and PAA-0.7-C_{12}/PVP) is ruled by their high modulus and the relaxation time of the polymer chains.

By fitting the experimental data with our model, we are able to recover the mean interfacial tension of the capsule, an effective modulus of the membrane, and the relaxation time of the polymer chains. All the values were in good agreement with what we measured in model geometries in the previous chapter.

3.3 Conclusion

In this chapter, through microfluidics we produced micro-capsules of controlled size with one or two layers of polymers, and we probed their interfacial properties.

A high level of control is required for the capsules production, either to have model capsules to study their properties or to enable the use of the capsules for targeted delivery. To this aim, we developed two production protocols using the advantages of microfluidics (low Reynolds number, easy control of the flow rates). First we designed a microfluidic chip to achieve batch production: a batch of droplets is produced using a flow focusing device and stored in a chamber. In this chamber, the droplets are rinsed with alternatively water and polymer solutions in order to add the different layers of the membrane. Despite the promising results of this method, some limitations were intrinsic to the process, as the adhesion of the capsules with the walls. To overcome these limitations, we developed a second protocol: the inline continuous production. In this microfluidic chip, droplets are produced and then conveyed through different channels and phase exchange cells in order to transfer them from the first polymer solution to successively water and the second polymer solution. Using this protocol we were able to produce monodisperse population of droplets with one or two polymer layers.

Our microfluidic protocol allows us to produce different kinds of capsules by changing the nature of the polymers at the interface. In order to investigate the rheological properties of these capsules, we injected them in a narrow channel which is connected to a chamber three times larger than the channel. We observed that when the width of the inlet channel is smaller than the diameter of the capsules, they deform when they enter the chamber owing to two phenomena: the stress induced by the surrounding fluid tends to elongate the capsule in the direction orthogonal to the trajectory of the capsules, whereas the eventual moduli of the membrane (liquid dilational modulus or elastic moduli) tend to maintain the capsule in its reference shape. Using finite-element simulations, we showed that the viscous flow (and thus the viscous stress) is modified by the presence of the capsule. Taking this effect into account with simulations, we calculated the flow in the chamber and thus the viscous stress exerted on the capsules. Accordingly, we were able to predict the theoretical capsules deformation.

We observed a good agreement of the prediction of the literature for the capsules consisting of one layer of PMAA. We observed that the addition of an anchoring energy or a second layer leads to deviations from the predictions. Consequently we extended our model to add the effect of the moduli to describe the deformation of these capsules through a mean interfacial tension, an interfacial modulus, and a relaxation time of the polymer chains of the membrane. This relaxation time depends on the membrane only, and fix the reference shape of the capsule as a function of time. By fitting our experiments with our model in the case of PAA-0.7-C_{12}, PAA-0.7-C_{12}/PVP and PMAA/PVP, we were able to extract these three parameters. The comparison of these extracted values with the results of more calibrated measurements in Chapter 2 yielded a good agreement.

These preliminary results on capsule deformation with viscoelastic membranes would benefit from more systematic experiments with various kinds of membranes and flow conditions to confirm the relevance of our theoretical description.

General conclusion

This thesis focused on the multilayer assembly of polymers at liquid interfaces. Through experimental observations on model interfaces and modeling, we studied the effect of the molecular interactions of polymer chains at an interface between two immiscible fluids on the rheological behaviour of this interface. This thesis consists of two distinct parts corresponding to two different approaches of the same study. In the first part, we used the model macroscopic geometry of the pendant drop to study independently the different phenomena taking place during the assembly and the deformation of the multilayers. We studied in great detail the influence of the anchoring of the first layer. In the second part, we used microfluidics to create micro-capsules of different kinds and to probe their mechanical properties resulting from all the phenomena studied in the first part.

The pendant-drop experiment constitutes a model system ideal to compare quantitatively different polymers and different multilayer assemblies. This very robust system allowed us to make a complete study of the influence of the anchoring of a polymer layer at an interface. We used polymers grafted with hydrophobic anchors to enhance and speed up their adsorption. The dynamics of these PAA-α-$\mathrm{C_n}$ chains depend on the graft size n and on the grafting density α. We revisited classical adsorption models to adapt them to our system. We showed that the adsorption dynamics can be modeled by an energetic barrier for adsorption which depends on a parameter $\mathcal{A}$: this parameter is the area of the portion of interface that need to be cleared to adsorb a new molecule. We showed that this area implies a stretching energy for the incoming molecules (especially if the area is small), and an interfacial energy to clear the interface (especially if the area is large). This model explains the adsorption dynamics and the influence of the grafting density.

To investigate the robustness of PAA-α-$\mathrm{C_n}$ monolayers, we probed the compression of such interfaces. We found that these layers partially desorb upon compression. The area decrease leads indeed to an increase in surface excess which yields desorption. However, we observed that polymer desorption is limited when the compression is fast, and that the longer the grafts are, the more slowly the polymers desorb. We also observed that increasing the grafting density leads to faster desorption. This non-straightforward effect is assumed to be a consequence of the increase of the polymer volume fraction close to the interface due to the increase of the grafting density.

Bolstered by this study of the monolayers behaviours, we focused on the rheology of multilayers. Compression of polymer multilayers showed that rheological properties strongly depend on the anchoring of the first layer and the interaction between the different layers. Two systems have been studied in detail. In the first one, by comparing the PVP/PAA and the PVP/PMAA systems, we highlighted the influence of the hydrophobic interactions. In the case of PVP/PAA the layers interact through hydrogen bonds only, whereas PVP/PMAA also exhibits hydrophobic interactions.

We observed that while PVP/PAA shows a very low dilational modulus $K \simeq 3\,\text{mN/m}$, PVP/PMAA exhibits a high dilational modulus of the order of $100\,\text{mN/m}$. The PVP/PMAA system also exhibits a high storage shear modulus $G' = 200\,\text{mN/m}$ and a significantly lower loss shear modulus $G'' = 40\,\text{mN/m}$. This high shear storage modulus is an evidence of the bilayer elasticity and of the strong interactions between the polymers. The second kind of system we studied implied polymer anchoring at the interface. We observed that combining a high anchoring energy and a strong interaction between the layers leads the PAA-0.7-C_{12}/PVP/PMAA system to yield a very high dilational modulus: $K = 1200\,\text{mN/m}$. We also showed that the use of a pressure probe in the pendant-drop apparatus allows the quantitative measurement of the dilational modulus despite the complex shape of the pendant drop. This method enables indeed a local measurement of the interfacial tension at the apex, where the high symmetry yields a local isotropic compression.

In the second part of my thesis, I investigated the behaviours of micro-capsules made of droplets covered by polymer multilayers. To obtain large populations of micro-capsules, we designed a microfluidic chip in which oil droplets are produced and conveyed through the different polymer solutions necessary for the layer-by-layer assembly. The chip was optimized to get homogeneous populations of droplets.

The production of micro-capsules being ensured, we designed a second chip which enables the stretching of the capsules by transferring them from a confined environment to an extensional flow. We observed a wide range of behaviours, from capsules that elongate ($D > 0$) and then relax ($D \to 0$), to capsules that are too stiff to elongate and that relax more or less rapidly from negative to zero deformation. By performing finite-element simulations, I have accessed the stress applied by the flow on the capsules. I was able to predict the deformation with a model from the literature only in the case of homogeneous and constant interfacial tension, which is the case for PMAA monolayer. Despite the knowledge of this model in the literature, such theoretical prediction of the whole deformation profile of the capsule along its trajectory through the chamber had not been described before. However we observed that PAA-0.7-C_{12} monolayers and PMAA/PVP and PAA-0.7-C_{12}/PVP bilayers shows completely different behaviours. By taking into account an elastic modulus (a liquid dilational modulus or a proper elastic modulus) and a typical polymer-chains relaxation time, we suggest a model to predict the deformation of these stiffer capsules, which shows very fast (PMAA/PVP) or on the contrary very slow relaxation (PAA-0.7-C_{12}/PVP). PAA-0.7-C_{12} monolayer behaviour is intermediate between the soft PMAA monolayer and the stiff bilayers.

To go further into the understanding of these multilayers, it would be interesting and certainly fruitful to study the ageing of these capsules in various environments. This study should indeed help to identify new possible stimuli to trigger the compounds release. In the case of the polymers studied in this thesis, which interact through hydrogen bonds, a natural stimulus would be the pH. Moreover, the permeability of the membrane to various kinds of molecules should be investigated to block or to tune the diffusion of the compound through it. Finally, the process of the assembly could be improved even further by using a polymer exhibiting both a high anchoring energy with the interface and strong interactions with the other layers. Such a combination could allow high elastic moduli even with only two layers. Furthermore, in order to produce such capsules at a larger scale for industrial applications, we should investigate new processes allowing the production of higher quantities with a good control of the adsorption and rinsing steps. The fluidized-bed process seems to fill these requirements, and would thus be a logical extension of this work.

Bibliography

[1] A. M. Raichur, J. Voros, M. Textor, and A. Fery, “Adhesion of polyelectrolyte microcapsules through biotin-streptavidin specific interaction,” *Biomacromolecules*, vol. 7, no. 8, pp. 2331–2336, 2006. 5, 6

[2] S. Mun and D. J. McClements, “Influence of interfacial characteristics on ostwald ripening in hydrocarbon oil-in-water emulsions,” *Langmuir*, vol. 22, pp. 1551–1554, feb 2006. 5

[3] B. Zeeb, M. Gibis, L. Fischer, and J. Weiss, “Influence of interfacial properties on Ostwald ripening in crosslinked multilayered oil-in-water emulsions,” *Journal of Colloid and Interface Science*, vol. 387, no. 1, pp. 65–73, 2012. 5

[4] B. Wang, Q. Zhao, F. Wang, and C. Gao, “Biologically driven assembly of polyelectrolyte microcapsule patterns to fabricate microreactor arrays,” *Angewandte Chemie - International Edition*, vol. 45, no. 10, pp. 1560–1563, 2006. 6

[5] M. Delcea, H. Mohwald, and A. G. Skirtach, “Stimuli-responsive LbL capsules and nanoshells for drug delivery,” *Advanced Drug Delivery Reviews*, vol. 63, no. 9, pp. 730–747, 2011. 6

[6] R. Palankar, A. G. Skirtach, O. Kreft, M. Bedard, M. Garstka, K. Gould, H. Mohwald, G. B. Sukhorukov, M. Winterhalter, and S. Springer, “Controlled intracellular release of peptides from microcapsules enhances antigen presentation on MHC class I molecules,” *Small*, vol. 5, no. 19, pp. 2168–2176, 2009. 6

[7] D. G. Shchukin, D. A. Gorin, and H. Mohwald, “Ultrasonically induced opening of polyelectrolyte microcontainers,” *Langmuir*, vol. 22, no. 17, pp. 7400–7404, 2006. 6

[8] A. G. Skirtach, B. G. D. Geest, A. Mamedov, A. A. Antipov, A. Kotov, and G. B. Sukhorukov, “Ultrasound stimulated release and catalysis using polyelectrolyte multilayer capsules,” *J. Mater. Chem.*, vol. 17, pp. 1050–1054, 2007. 6

[9] W. Wang, L. Liu, X. J. Ju, D. Zerrouki, R. Xie, L. Yang, and L. Y. Chu, “A novel thermo-induced self-bursting microcapsule with magnetictargeting property,” *ChemPhysChem*, vol. 10, no. 14, pp. 2405–2409, 2009. 6

[10] S. H. Hu, C. H. Tsai, C. F. Liao, D. M. Liu, and S. Y. Chen, “Controlled rupture of magnetic polyelectrolyte microcapsules for drug delivery,” *Langmuir*, vol. 24, no. 20, pp. 11811–11818, 2008. 6

[11] H. N. Yow and A. F. Routh, “Formation of liquid core-polymer shell microcapsules,” *Soft Matter*, vol. 2, no. 11, p. 940, 2006. 6

[12] A. M. Rosenthal and T. M. S. Chang, "The incorporation of lipid and Na+-K+-ATPase into the membranes of semipermeable microcapsules," *Journal of Membrane Science*, vol. 6, no. C, pp. 329–338, 1980. 6

[13] A. Burger, H. Leonhard, H. Rehage, R. Wagner, and M. Schwoerer, "Ultrathin crosslinked membranes at the interface between oil and water," *Macromolecular Chemistry and Physics*, vol. 196, no. 1, pp. 1–46, 1995. 6

[14] H. Rehage, M. Husmann, and A. Walter, "From two-dimensional model networks to microcapsules," *Rheologica Acta*, vol. 41, pp. 292–306, may 2002. 6

[15] E. Donath, G. B. Sukhorukov, F. Caruso, S. a. Davis, and H. Mohwald, "Novel Hollow Polymer Shells by Colloid-Templated Assembly of Polyelectrolytes," *Angew Chem Int Ed Engl*, vol. 37, no. 16, pp. 2201–2205, 1998. 6, 7

[16] F. Caruso and H. Mohwald, "Preparation and characterization of ordered nanoparticle and polymer composite multilayers on colloids," *Langmuir*, vol. 15, no. 23, pp. 8276–8281, 1999. 6

[17] G. Decher, J. D. Hong, and J. Schmitt, "Buildup of Ultrathin Multilayer Films By a Self-Assembly Process .3. Consecutively Alternating Adsorption of Anionic and Cationic Polyelectrolytes on Charged Surfaces," *Thin Solid Films*, vol. 210, no. 1-2, pp. 831–835, 1992. 6

[18] G. Decher, "Fuzzy Nanoassemblies: Toward Layered Polymeric Multicomposites," *Science*, vol. 277, no. 5330, pp. 1232–1237, 1997. 6, 7

[19] U. Klinkesorn, P. Sophanodora, P. Chinachoti, E. A. Decker, and D. J. McClements, "Encapsulation of emulsified tuna oil in two-layered interfacial membranes prepared using electrostatic layer-by-layer deposition," *Food Hydrocolloids*, vol. 19, no. 6, pp. 1044–1053, 2005. 7

[20] M. O. Lisunova, I. Drachuk, O. A. Shchepelina, K. D. Anderson, and V. V. Tsukruk, "Direct probing of micromechanical properties of hydrogen-bonded layer-by-layer microcapsule shells with different chemical compositions," *Langmuir*, vol. 27, no. 17, pp. 11157–11165, 2011. 7

[21] S. Le Tirilly, C. Tregouet, S. Bone, C. Geffroy, G. Fuller, N. Pantoustier, P. Perrin, and C. Monteux, "Interplay of Hydrogen Bonding and Hydrophobic Interactions to Control the Mechanical Properties of Polymer Multilayers at the Oil/Water Interface," *ACS Macro Letters*, vol. 4, no. 1, pp. 25–29, 2014. 7, 64, 65

[22] R. Seemann, M. Brinkmann, T. Pfohl, and S. Herminghaus, "Droplet based microfluidics," *Rep. Prog. Phys.*, vol. 75, no. 75, pp. 16601–41, 2012. 8

[23] L. Y. Chu, A. S. Utada, R. K. Shah, J. W. Kim, and D. A. Weitz, "Controllable monodisperse multiple emulsions," *Angewandte Chemie - International Edition*, vol. 46, no. 47, pp. 8970–8974, 2007. 8

[24] A. R. Abate and D. A. Weitz, "High-Order Multiple Emulsions Formed in Poly(dimethylsiloxane) Microfluidics," *Small*, vol. 5, pp. 2030–2032, sep 2009. 8

[25] C. Kantak, S. Beyer, L. Yobas, T. Bansal, and D. Trau, “A ’microfluidic pinball’ for on-chip generation of Layer-by-Layer polyelectrolyte microcapsules.,” *Lab on a chip*, vol. 11, pp. 1030–5, mar 2011. 8

[26] C. Priest, A. Quinn, A. Postma, A. N. Zelikin, J. Ralston, and F. Caruso, “Microfluidic polymer multilayer adsorption on liquid crystal droplets for microcapsule synthesis.,” *Lab on a chip*, vol. 8, pp. 2182–2187, dec 2008. 8

[27] P.-G. de Gennes, F. Brochard-Wyart, and D. Quere, *Gouttes, bulles, perles et ondes.* Belin, 2005. 10

[28] E. A. Guggenheim, “The thermodynamics of interfaces in systems of several components,” *Transactions of the Faraday Society*, vol. 35, p. 397, 1940. 10

[29] H.-J. Butt, K. Graf, and M. Kappl, *Physics and Chemistry of Interfaces.* Weinheim: Wiley-VCH, second, re ed., 2006. 10, 16

[30] A. Marchand, J. H. Weijs, J. H. Snoeijer, and B. Andreotti, “Why is surface tension a force parallel to the interface?,” *American Journal of Physics*, vol. 79, no. October, p. 999, 2011. 11

[31] C. Pozrikidis, *Modeling and Simulation of Capsules and Biological Cells.* Boca Raton, FL: Chapman & Hall/CRC, 2003. 11, 26

[32] D. Vollhardt, V. B. Fainerman, and G. Emrich, “Dynamic and equilibrium surface pressure of adsorbed dodecanol monolayers at the air/water interface,” *Journal of Physical Chemistry B*, vol. 104, no. 35, pp. 8536–8543, 2000. 15

[33] B. Loppinet and C. Monteux, “Dynamics of surfactants and polymers at liquid interfaces,” in *Soft Matter at Aqueous Interfaces* (P. R. Lang and Y. Liu, eds.), vol. 917 of *Lecture Notes in Physics*, ch. 5, pp. 137–157, Cham: Springer International Publishing, 2016. 18

[34] a. F. H. Ward and L. Tordai, “Time-Dependence of Boundary Tensions of Solutions I. The Role of Diffusion in Time Effects,” *The Journal of Chemical Physics*, vol. 14, no. 1946, pp. 453–461, 1946. 18

[35] I. Langmuir, “The Adsorption of Gases on Plane Surfaces of Glass, Mica and Platinum,” *Journal of the American Chemical Society*, vol. 40, no. 9, pp. 1361–1403, 1918. 19

[36] A. F. H. Ward and L. Tordai, “Time-dependence of boundary tensions of solutions: IV. Kinetics of adsorption at liquid-liquid interfaces,” *Recueil des Travaux Chimiques des Pays-Bas*, vol. 71, no. 6, pp. 572–584, 1952. 20, 46, 69

[37] B. Andreotti and J. H. Snoeijer, “Soft wetting and the Shuttleworth effect, at the crossroads between thermodynamics and mechanics,” *EPL (Europhysics Letters)*, vol. 113, no. 6, p. 66001, 2016. 20

[38] J. Lucassen and M. Van Den Tempel, “Dynamic measurements of dilational properties of a liquid interface,” *Chemical Engineering Science*, vol. 27, no. 6, pp. 1283–1291, 1972. 25

[39] S. Knoche and J. Kierfeld, “Buckling of spherical capsules,” *Physical Review E - Statistical, Nonlinear, and Soft Matter Physics*, vol. 84, no. 4, pp. 1–13, 2011. 25

[40] S. Knoche, D. Vella, E. Aumaitre, P. Degen, H. Rehage, P. Cicuta, and J. Kierfeld, “Elastometry of deflated capsules: Elastic moduli from shape and wrinkle analysis,” *Langmuir*, vol. 29, no. 40, pp. 12463–12471, 2013. 25

[41] D. Barthès-Biesel, A. Diaz, and E. Dhenin, “Effect of constitutive laws for two-dimensional membranes on flow-induced capsule deformation,” *Journal of Fluid Mechanics*, vol. 460, pp. 211–222, 2002. 26

[42] J. K. Ferri, P. Carl, N. Gorevski, T. P. Russell, Q. Wang, A. Boker, and A. Fery, “Separating membrane and surface tension contributions in Pickering droplet deformation,” *Soft Matter*, vol. 4, no. 11, p. 2259, 2008. 27

[43] J. K. Ferri, P. a. L. Fernandes, J. T. McRuiz, and F. Gambinossi, “Elastic nanomembrane metrology at fluid–fluid interfaces using axisymmetric drop shape analysis with anisotropic surface tensions: deviations from Young–Laplace equation,” *Soft Matter*, vol. 8, no. 40, p. 10352, 2012. 27, 49

[44] P. Marmottant, S. van der Meer, M. Emmer, M. Versluis, N. de Jong, S. Hilgenfeldt, and D. Lohse, “A model for large amplitude oscillations of coated bubbles accounting for buckling and rupture,” *The Journal of the Acoustical Society of America*, vol. 118, no. 6, p. 3499, 2005. 27

[45] J. T. Petkov, T. D. Gurkov, B. E. Campbell, and R. P. Borwankar, “Dilatational and shear elasticity of gel-like protein layers on air/water interface,” *Langmuir*, vol. 16, no. 8, pp. 3703–3711, 2000. 28

[46] L. D. Landau and E. M. Lifschitz, *Theory of elasticity.* London: Pergamon Press, 1953. 28

[47] S. Vandebril, A. Franck, G. G. Fuller, P. Moldenaers, and J. Vermant, “A double wall-ring geometry for interfacial shear rheometry,” *Rheologica Acta*, vol. 49, pp. 131–144, dec 2009. 28

[48] P. Cicuta and E. M. Terentjev, “Viscoelasticity of a protein monolayer from anisotropic surface pressure measurements,” *European Physical Journal E*, vol. 16, no. 2, pp. 147–158, 2005. 29

[49] C. Quilliet, A. Farutin, and P. Marmottant, “Effect of Gaussian curvature modulus on the shape of deformed hollow spherical objects,” *The European Physical Journal E*, vol. 39, no. 6, p. 58, 2016. 30

[50] M. van Dyke and F. M. White, “An Album of Fluid Motion,” 1982. 32

[51] B. M. Paegel, R. G. Blazej, and R. A. Mathies, “Microfluidic devices for DNA sequencing: Sample preparation and electrophoretic analysis,” *Current Opinion in Biotechnology*, vol. 14, no. 1, pp. 42–50, 2003. 33

[52] B. Lincoln, H. M. Erickson, S. Schinkinger, F. Wottawah, D. Mitchell, S. Ulvick, C. Bilby, and J. Guck, “Deformability-based flow cytometry,” *Cytometry*, vol. 59A, no. 2, pp. 203–209, 2004. 33

[53] G. I. Taylor, "The Formation of Emulsions in Definable Fields of Flow," *Proceedings of the Royal Society A: Mathematical, Physical and Engineering Sciences*, vol. 146, pp. 501–523, oct 1934. 34, 35, 91, 112

[54] J. S. Lee, R. Dylla-Spears, N. P. Teclemariam, and S. J. Muller, "Microfluidic four-roll mill for all flow types," *Applied Physics Letters*, vol. 90, no. 7, pp. 2005–2008, 2007. 34

[55] J. Deschamps, V. Kantsler, E. Segre, and V. Steinberg, "Dynamics of a vesicle in general flow.," *Proceedings of the National Academy of Sciences of the United States of America*, vol. 106, no. 28, pp. 11444–7, 2009. 34

[56] S. D. Hudson, J. T. Cabral, W. J. Goodrum, K. L. Beers, and E. J. Amis, "Microfluidic interfacial tensiometry," *Applied Physics Letters*, vol. 87, no. 8, p. 081905, 2005. 34, 35, 110, 111, 121

[57] J. T. Cabral and S. D. Hudson, "Microfluidic approach for rapid multicomponent interfacial tensiometry.," *Lab on a chip*, vol. 6, pp. 427–436, mar 2006. 34, 35, 110

[58] Q. Brosseau, J. Vrignon, and J.-C. Baret, "Microfluidic Dynamic Interfacial Tensiometry (μDIT).," *Soft matter*, vol. 10, pp. 3066–76, may 2014. 34, 35, 91

[59] D. Barthes-Biesel and A. Acrivos, "Deformation and burst of a liquid droplet freely suspended in a linear shear field," *Journal of Fluid Mechanics*, vol. 61, pp. 1–22, 1973. 34, 35, 36

[60] D. Barthes-Biesel and J. M. Rallison, "The time-dependent deformation of a capsule freely suspended in a linear shear flow," *Journal of Fluid Mechanics*, vol. 113, no. -1, p. 251, 1981. 34, 113

[61] J. M. Rallison, "The Deformation of Small Viscous Drops and Bubbles in Shear Flows," *Annual Review of Fluid Mechanics*, vol. 16, no. 1, pp. 45–66, 1984. 34, 104

[62] M. Rubinstein and R. H. Colby, *Polymer Physics*. New York: Oxford Uni, 2003. 37, 39, 41, 71

[63] P. Mansky, "Controlling Polymer-Surface Interactions with Random Copolymer Brushes," *Science*, vol. 275, no. 5305, pp. 1458–1460, 1997. 39

[64] S. Hu, X. Ren, M. Bachman, C. E. Sims, G. P. Li, and N. Allbritton, "Surface modification of poly(dimethylsiloxane) microfluidic devices by ultraviolet polymer grafting," *Analytical Chemistry*, vol. 74, no. 16, pp. 4117–4123, 2002. 39

[65] S. G. Ash, D. H. Everett, and C. Radke, "Thermodynamics of the effects of adsorption on interparticle forces," *Journal of the Chemical Society, Faraday Transactions 2*, vol. 69, p. 1256, 1973. 39

[66] J. Feder and I. Giaever, "Adsorption of ferritin," *Journal Of Colloid And Interface Science*, vol. 78, no. 1, pp. 144–154, 1980. 39

[67] S. Alexander, "Adsorption of chain molecules with a polar head a scaling description," *Journal de Physique*, vol. 38, no. 8, pp. 983–987, 1977. 40

[68] P.-G. de Gennes, “Conformations of Polymers Attached to an Interface,” *Macromolecules*, vol. 13, no. 19, pp. 1069–1075, 1980. 40

[69] P. G. de Gennes, “Polymer solutions near an interface. Adsorption and depletion layers,” *Macromolecules*, vol. 14, no. 6, pp. 1637–1644, 1981. 41

[70] B. A. Noskov, “Dynamic surface elasticity of polymer solutions,” *Colloid & Polymer Science*, vol. 273, no. 3, pp. 263–270, 1995. 41, 42

[71] F. Millet, J. J. Benattar, and P. Perrin, “Vertical free-standing films of amphiphilic associating polyelectrolytes.,” *Physical review. E, Statistical physics, plasmas, fluids, and related interdisciplinary topics*, vol. 60, pp. 2045–2050, aug 1999. 42, 44

[72] F. Millet, M. Nedyalkov, B. Renard, P. Perrin, F. Lafuma, and J.-J. Benattar, “Adsorption of Hydrophobically Modified Poly(acrylic acid) Sodium Salt at the Air/Water Interface by Combined Surface Tension and X-ray Reflectivity Measurements,” *Langmuir*, vol. 15, pp. 2112–2119, mar 1999. 42, 44

[73] E. Leclerc, R. Douillard, M. Daoud, and V. Aguie-Beghin, “Asymmetric Multiblock Copolymers at the Gas – Liquid Interface : Phase Diagram and Surface Pressure,” *Journal of Colloid and Interface Science*, vol. 155, pp. 143–155, jun 1999. 43, 68

[74] D. E. Graham and M. C. Phillips, “Proteins at liquid interfaces. I. Kinetics of adsorption and surface denaturation,” *Journal of Colloid And Interface Science*, vol. 70, no. 3, pp. 403–414, 1979. 44

[75] J. Benjamins, A. Cagna, and E. H. Lucassen-Reynders, “Viscoelastic properties of triacylglycerol/water interfaces covered by proteins,” *Colloids and Surfaces A: Physicochemical and Engineering Aspects*, vol. 114, pp. 245–254, aug 1996. 44

[76] F. Millet, P. Perrin, M. Merlange, and J. J. Benattar, “Logarithmic adsorption of charged polymeric surfactants at the air-water interface,” *Langmuir*, vol. 18, no. 23, pp. 8824–8828, 2002. 44, 73

[77] L. Aricov, H. Petkova, D. Arabadzhieva, A. Iovescu, E. Mileva, K. Khristov, G. Stinga, C.-f. Mihailescu, D. Florin, and R. Todorov, “Aqueous solutions of associative poly (acrylates): Bulk and interfacial properties,” *Colloids and Surfaces A: Physicochemical and Engineering Aspects*, vol. 505, pp. 138–149, 2016. 44

[78] A. Johner and J. F. Joanny, “Block copolymer adsorption in a selective solvent: a kinetic study,” *Macromolecules*, vol. 23, no. 26, pp. 5299–5311, 1990. 45, 46, 69

[79] C. Ligoure and L. Leibler, “Thermodynamics and kinetics of grafting end-functionalized polymers to an interface,” *Journal de Physique*, vol. 51, no. 12, pp. 1313–1328, 1990. 46, 47, 69

[80] C. Barentin, P. Muller, and J. Joanny, “Polymer brushes formed by end-capped poly (ethylene oxide)(PEO) at the air-water interface,” *Macromolecules*, vol. 9297, no. 97, pp. 2198–2211, 1998. 47, 48

[81] B. A. Noskov, S. Lin, G. Loglio, R. G. Rubio, R. Miller, V. Lastruccia, and S. Fiorentino, “Dilational Viscoelasticity of PEO - PPO - PEO Triblock Copolymer Films at the Air - Water Interface in the Range of High Surface Pressures,” *Langmuir*, no. 12, pp. 2647–2652, 2006. 47, 48

[82] J. Ferri, W. Dong, R. Miller, and H. Mohwald, “Elastic moduli of asymmetric ultrathin free-standing polyelectrolyte nanocomposites,” *Macromolecules*, pp. 1532–1537, 2006. 49

[83] K. T. Wang, I. Iliopoulos, and R. Audebert, “Viscometric behaviour of hydrophobically modified poly(sodium acrylate),” *Polymer Bulletin*, vol. 20, pp. 577–582, 1988. 56

[84] T. Chen, M. S. Chiu, and C. N. Weng, “Derivation of the generalized Young-Laplace equation of curved interfaces in nanoscaled solids,” *Journal of Applied Physics*, vol. 100, no. 7, 2006. 60

[85] S. le Tirilly, C. Tregouet, M. Reyssat, S. Bone, C. Geffroy, G. G. Fuller, N. Pantoustier, P. Perrin, and C. Monteux, “Interfacial rheology of hydrogen-bonded polymer multilayers assembled at liquid interfaces. Influence of anchoring energy and hydrophobic interactions,” *Langmuir*, p. acs.langmuir.6b01054, 2016. 66

[86] A. Einstein, “The motion of elements suspended in static liquids as claimed in the molecular kinetic theory of heat,” *Annelen der Physik*, vol. 17, no. 8, pp. 549–565, 1905. 72

[87] Z. Mao and S. B. Sinnott, “Separation of organic molecular mixtures in carbon nanotubes and bundles: Molecular dynamics simulations,” *Journal of Physical Chemistry B*, vol. 105, no. 29, pp. 6916–6924, 2001. 72

[88] A. Theodoratou, U. Jonas, B. Loppinet, T. Geue, R. Stangenberg, R. Keller, D. Li, R. Berger, J. Vermant, and D. Vlassopoulos, “Semifluorinated Alkanes at the Air-Water Interface: Tailoring Structure and Rheology at the Molecular Scale,” *Langmuir*, vol. 32, no. 13, pp. 3139–3151, 2016. 87

[89] J. D. Martin and S. D. Hudson, “Mass transfer and interfacial properties in two-phase microchannel flows,” *New Journal of Physics*, vol. 11, p. 115005, nov 2009. 91, 104, 110

[90] J. D. Martin, J. N. Marhefka, K. B. Migler, and S. D. Hudson, “Interfacial rheology through microfluidics,” *Advanced Materials*, vol. 23, pp. 426–432, jan 2011. 91

[91] Y. Xia and G. M. Whitesides, “Soft Lithography,” *Annual Review in Material Science*, vol. 28, no. 12, pp. 153–184, 1998. 92

[92] S. L. Anna, N. Bontoux, and H. A. Stone, “Formation of dispersions using "flow focusing" in microchannels,” *Applied Physics Letters*, vol. 82, no. 3, pp. 364–366, 2003. 95

[93] A. S. Utada, A. Fernandez-Nieves, H. A. Stone, and D. A. Weitz, “Dripping to jetting transitions in coflowing liquid streams,” *Physical Review Letters*, vol. 99, no. 9, pp. 1–4, 2007. 95

[94] M. J. Fuerstman, A. Lai, M. E. Thurlow, S. S. Shevkoplyas, H. a. Stone, and G. M. Whitesides, “The pressure drop along rectangular microchannels containing bubbles.,” *Lab on a chip*, vol. 7, no. 11, pp. 1479–1489, 2007. 98

[95] M. Yamada, M. Nakashima, and M. Seki, “Pinched flow fractionation: Continuous size separation of particles utilizing a laminar flow profile in a pinched microchannel,” *Analytical Chemistry*, vol. 76, no. 18, pp. 5465–5471, 2004. 99

[96] D. Bartolo, G. Degre, P. Nghe, and V. Studer, “Microfluidic stickers,” *Lab on a Chip-Miniaturisation for Chemistry and Biology*, vol. 8, no. 2, pp. 274–279, 2008. 102

[97] I. Polenz, Q. Brosseau, and J. C. Baret, “In situ encapsulation kinetics monitored by microfluidics,” *Procedia IUTAM*, vol. 16, pp. 115–122, 2015. 102

[98] R. G. Cox, “The deformation of a drop in a general time-dependent fluid flow,” *Journal of Fluid Mechanics*, vol. 37, no. 03, pp. 601–623, 1969. 104

[99] E. Lauga, M. P. Brenner, and H. a. Stone, “Microfluidics: The no-slip boundary condition,” in *Springer Handbook of Experimental Fluid Mechanics*, ch. 19, pp. 1219–1240, Springer, 2005. 109

[100] E. Leclerc, H. Kinoshita, T. Fujii, and D. Barthès-Biesel, “Transient flow of microcapsules through convergent–divergent microchannels,” *Microfluidics and Nanofluidics*, vol. 12, pp. 761–770, dec 2011. 114

[101] P. Y. Gires, D. Barthes-Biesel, E. Leclerc, and A. V. Salsac, “Transient behavior and relaxation of microcapsules with a cross-linked human serum albumin membrane,” *Journal of the Mechanical Behavior of Biomedical Materials*, vol. 58, pp. 2–10, 2016. 114

Multicouches de polymères aux interfaces liquides :
assemblage, rhéologie interfaciale et analyse microfluidique.

Résumé Le relargage contrôlé est un enjeu industriel auquel l'encapsulation peut répondre. Une méthode prometteuse pour fabriquer des micro-capsules consiste à déposer couche après couche des polymères à la surface de goutte d'huiles ou de bulles d'air. Cette thèse a pour objet ces assemblages en multicouches de polymères aux interfaces liquides. A partir d'expériences menées sur des interfaces modèles entre deux fluides non miscibles et leur modélisation, nous avons étudié l'effet des interactions à l'échelle des chaînes de polymère sur les propriétés rhéologiques de l'interface. Dans un premier temps nous avons utilisé la géométrie modèle qu'est la goutte pendante pour étudier indépendamment les différents phénomènes impliqués dans l'assemblage des multicouches et dans leur déformation. Nous avons revisité différents modèles classique pour décrire l'adsorption de nos polymères à l'interface, puis nous avons mesuré les modules interfaciaux de différents systèmes de polymères. Pour cela, à l'aide de mesures complémentaires, nous avons établi un cadre pour les mesures de modules élastiques en goutte pendante. Dans un second temps, nous avons utilisé la microfluidique pour fabriquer différents types de micro-capsules et pour mesurer leurs propriétés mécaniques. Celles-ci résultent des différents phénomènes étudiés dans la première partie de cette thèse. Nous avons établi un modèle et effectué des simulations numériques qui nous permettent d'extraire les principales propriétés interfaciales de nos capsules à partir de la mesure de leur déformation dans les canaux microfluidiques.

Mots-clés : encapsulation, polymères, layer-by-layer, rhéologie interfaciale, microfluidique, hydrodynamique.

Polymer multilayers at liquid interfaces:
assembly, interfacial rheology and microfluidic probing.

Abstract In order to improve control over the delivery of chemicals, industries seek a way to encapsulate them. A promising method to produce artificial micro-capsules consists in assembling several layers of polymer at the interface of an oil droplet or an air bubble. This thesis focuses on these multilayer assemblies of polymers at liquid interfaces. Through experimental observations on model interfaces and modeling, we studied the effect of the molecular interactions of polymer chains at an interface between two immiscible fluids on the rheological behaviour of this interface. In a first part, we used the model macroscopic geometry of the pendant drop to study independently the different phenomena taking place during the assembly and the deformation of the multilayers. We revisited classical models to describe the adsorption dynamics of our polymers, and we measured the interfacial dilational modulus of various systems. To this aim, by performing independent measurements, we delimited the range of validity of the pendant-drop apparatus. In the second part, we used microfluidics to create micro-capsules of different kinds and to probe their mechanical properties resulting from all the phenomena studied in the first part. We developed a model and we performed numerical simulations to extract the main interfacial properties of our capsules from the measurement of their deformation in the channels.

Keywords: encapsulation, polymers, layer-by-layer, interfacial rheology, microfluidics, hydrodynamics.